The topology and electrical properties of nanoparticle networks

Emmanuel Ohieku Jonah

A thesis presented for the degree of

DOCTOR OF PHILOSOPHY

in the Department of Physics

Faculty of Science

University of CapeTown

December 2013

Abstract

The bulk and surface network topologies of milled silicon nanoparticle aggregates in layers deposited on porous and non-porous substrates have been quantitatively characterised using laboratory and synchrotron based small angle X-ray scattering and ultra-small angle X-ray scattering, as well as with a new surface scattering technique developed for this research, which can be described as wide angle low q scattering. A new scaling model applied to the small angle and ultra-small angle X-ray scattering data which was originally developed to describe branched polymers was shown to be applicable to the description of the networks of silicon particles. The milled particles which have a highly polydisperse size distribution, form agglomerates, which in turn cluster to form larger structures with a very high degree of aggregation. Results from the new scattering technique showed the rough surface of the printed layers to have a fractal structure with step heights of 10% to 20% between adjacent particles. This value is consistent with the topology of the particle aggregates in the layer inferred from ultra-small angle X-ray scattering. Flow properties of the inks on different substrates lead to quantitative differences in the mean aggregate separation, with slowly curing systems on materials which allow good capillary flow resulting in denser networks with smaller aggregates and better contact between particles. The electrical conductance of the layers was shown to be linearly related to parallel connections of the minimum paths of particles through the aggregates as determined from the analysis of ultra-small angle X-ray scattering data. The capacitance of the layers was shown to have a linear dependence on both the separation between primary particles and series connection of the minimum paths.

Acknowledgement

My thanks to my Lord and Saviour Jesus Christ who enabled me all these years to be able to go through this research.

My supervisors, Prof David T. Britton and Prof Margit Härting, I am grateful for the privilege you accorded me to work and learn with your guidance and support.

My wife Veronica for her overwhelming support. Also to my son Peter, you are indeed a blessing to us and thanks for your patience and support.

To my parents Mr M.A. Jonah and Mrs Fatima, my siblings Mrs Elizabeth and her family, Joseph and his family, David and his family, Jacob, Martha and Samuel, thank you all for the support and encouragement.

To my in-laws, Mr and Mrs J Amlabu, Mrs Mercy and her family, Lucy, Blessing and David, thanks for the support.

The Awodeles and Gonasillans, I will always be grateful for your support here in Cape Town.

My thanks to Prof. G. Beaucage, Dr. J. Ilavsky, Dr. G. Smith, and Dr. D.K. Rai for your comments and support in the course of this research.

Special thanks to the NanoScience Innovation Centre group members; past and present. I will always be grateful for the countless hours of discussions and support in the lab.

A special thanks to my sponsors during the course of this thesis, the *NanoPower Africa* Project funded by *United States Agency for International Development* (USAID) through *the Higher Education for Development* (HED) office. Also my thanks to other sponsors through the UCT NanoSciences Innovation Centre. These are the US Airforce Office of Scientific Research, University of Cape Town Vice Chancellor's Strategic Fund, and the South African Department of Science and Technology through its business unit. My thanks to the staff members of the ChemMatCARS Sector 15 of Argon National lab USA. ChemMatCARS Sector 15 is principally supported by the National Science Foundation/Department of Energy under grant number NSF/CHE-0822838. Use of the Advanced Photon Source was supported by the U. S. Department of Energy, Office of Science, Office of Basic Energy Sciences, under Contract No.DEAC02-06CH11357.

Contents

1. Introduction

The study of nanoparticles in printed electronics is necessary and of great interest, as they make up the major components of many electronic inks [1, 2, 3]. These type of particles are known to exhibit properties which differ from their bulk materials due to the influence of their large size to volume ratio [4, 5]. The properties of nanoparticles could have advantages or disadvantages depending on the application. For instance, the aggregation of nanoparticles which arises as a result of their surface properties is a disadvantage in many inks used for printed electronics. Surfactants are now being used to alter the surface properties of these nanoparticles in order to reduce aggregation [1, 6]. Similar to the surface, nanoparticles sizes and shapes could affect the electrical, thermal conductivity and stability of printed electronic inks [7].

A major challenge when nanoparticles are introduced in printed electronic inks, is the interfacial interaction between the particles and the surrounding binder matrix which are mostly polymers. Depending on the nature of the polymer binder, a core shell structure could be formed by the binders around the nanoparticles as a result of their high surface areas [8]. The size and effects of the core shell increases as the particle sizes decreases, which implies that the interfacial layer formed could affect the macroscopic properties of aggregates of these particles [9, 10]. Since different materials will behave differently relative to their interfacial properties, it is therefore necessary to understand how interfaces will behave electrically when used for printed electronic devices. The interfacial polymer layer is also dependent on the topographic features of the nanoparticle aggregates [11, 12], it is also important to understand the topology of the surface for different types of nanoparticle aggregates and how they affect the macroscopic properties of printed layers.

Semiconducting materials are some of the most used in printed electronics, and they could be in the form of solution processable organic semiconductors [13, 14], or inorganic nanoparticles [15]. Recently, the use of elemental silicon nanoparticles in printed electronics has been demonstrated for the production of low cost devices with flexible form factor [16]. For an assembly of silicon nanoparticles to function as a semiconductor in a printed layer, where the layer consists of a binder and individual nanoparticles and aggregates [17], transport of charge has to take place through the network of particles. Hence, an intimate contact between the particles, and the aggregates of particles, is necessary, to form a dense network providing percolation paths for the charges. Because the electrical properties, as well as other physical

properties, depend on the arrangement and connectivity of the particles in such aggregate systems, it is necessary to understand the structural topology of the particle networks as well as their detailed microstructure. However, there are few experimental techniques and analytical tools available for a quantitative description of aggregate structures.

The use of scaling theories to describe the topology of random features of aggregates has been popularised in the past few decades. One such approach, is the use of percolation scaling theory [18, 19, 20] which relates connected paths with transport in disordered structures. Previous works using this approach, have employed simulations to show that the electrical resistance of such structures can be scaled with the fractal properties of the structure [21, 22, 23]. However, no experimentally found evidence of such a scaling has been reported for nanoparticulate aggregates. Another use of the scaling theory to describe structures is in its application to the results of small angle scattering (SAS) experiments [24, 25]. In this case, such an application has traditionally been limited to relating the fractal dimension of an aggregate with the size of the aggregate. Only recently the application of scaling theory to SAS data has been extended to quantify disordered features [26, 27]. An extended scaling model was developed for the description of the folding states of highly branched polymers [26, 28], but it has so far not been applied to nanoparticulate aggregate systems.

In this research, laboratory small angle X-ray scattering (SAXS) and synchrotron ultra-small-angle X-ray scattering (USAXS) are applied to the study of the network structure formed by silicon nanoparticles using a scaling model recently developed for the description of highly branched polymers [26]. Silicon nanoparticle systems were produced by using printing and coating techniques, to deposit inks containing these nanoparticles onto a substrate. In this work it will be shown, that the topological features determined with USAXS measurements can be combined with the results of the electrical measurements to relate to charge transport of an aggregated system of silicon particles. This was achieved by relating the structural parameters determined from USAXS with the electrical resistance and capacitance determined from the analysis of current - voltsge (IV) characteristic of the printed layers. Since the surface feature of a printed layer contributes to the overall electrical properties especially charge transport in multilayer devices, similar to what was described in [17], a new scattering technique was developed in the framework of this research to determine the topology of the network of particles at the surface. Results from the new surface probing technique were compared with results from the traditional bulk probing USAXS to determine if there are differences between the networks of particles on the surface and the bulk of printed layers.

Chapter 2 briefly describes the morphology of silicon nanoparticles with respect to production processes. A review of small angle X-ray scattering (SAXS) theory as well as the application of a new scaling approach to the scattering data of particulate systems is presented in chapter 3. The experimental details are described in chapter 4, and the results obtained presented in chapter 5. Further clarification on the result are given in chapter 6, and the conclusions reached in this research are stated in chapter 7.

2. Silicon and the morphology of silicon nanoparticles

Silicon is the dominant material in the electronic industry, making it the most important of all semiconductors [29]. The silicon atom is covalently bonded to four nearest neighbour atoms forming a tetrahedron. When a long range order of the tetrahedral structure is present, the silicon is described as crystalline, such as in silicon wafers which are mostly used as substrates for microelectronic device fabrication [30, 31]. Silicon with short range order is described as amorphous, and it is used mainly as the active layer in thin-film field effect transistors for display panels [32] and in solar cells [33, 34]. An intermediate material is polycrystalline silicon, with a disordered arrangement of grains with the ordered structure of crystalline silicon, which is also used in solar cells [35]. Recently, attention has focused on the use of silicon nanomaterials (nanoparticles, nanorods, quantum dots, etc.) in electronic devices [36, 37], because of the prospect of developing devices with enhanced properties. In this work, the definition of nanoparticles that will be used, is the more widely acceptable definition given by the International Organisation for Standardisation (ISO) in 2008. Nanoparticle is defined as a "Nano-object with all three of its external dimension in the nanoscale" (ISO/TS 27687:2008), and the nanoscale is defined as the "size range from approximately 1 nm to 100 nm" (ISO/TS 27687:2008).

In this chapter, the morphology and aggregation of silicon nanoparticles associated with their production processes are described.

2.1 Morphology of silicon nanoparticles

The unique properties exhibited by nanoparticles, which are different from the corresponding bulk materials, are mostly due to the large surface to volume ratio associated with nanoparticles [38]. This feature is both size and morphology dependent, since the shape of a material also determines the amount of available surface [39]. The size and shape of nanoparticles are features which are dependent on the way the particles are produced. Generally, two main approaches are used for nanoparticle production: "bottom-up" and "top-down" [4]. The morphology of silicon nanoparticles produced using processes categorised according to these approaches are described below.

2.1.1 Bottom-up production of silicon nanoparticles

The synthesis of nanoparticles using the "bottom-up" approach, is brought about by the agglomeration of atoms or molecules. Different methods that have been developed using this approach include aerosol methods [40], chemical vapour deposition [41] and liquid phase methods [42]. Figure 2.1 shows typical TEM micrographs [40, 41] of Si nanoparticles produced using bottom-up approach.

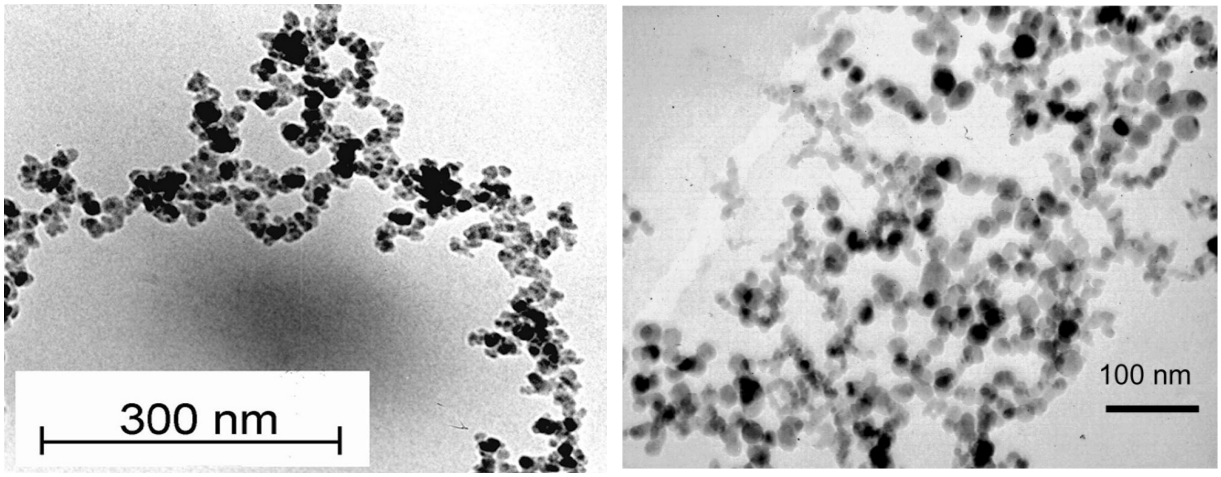

(a) (b)

Figure 2.1: Silicon nanoparticles produced using bottom-up approach, with (a) TEM observation Si nanoparticles produced using aerosol method [40], and (b) TEM observation of Si nanoparticles prepared by laser pyrolysis of silane - a vapour phase method [41].

In both the aerosol method (figure 2.1a) and the vapour phase deposition (figure 2.1b), branched chains of nanoparticles are formed. The particles also tend to coalesce (sinter) with adjacent particles, and overlap between particles is also observed. From both figures, it can be seen that mainly spherical nanoparticles with a weakly polydisperse size distribution can be produced using these approaches. In general, it should be noted that with respect to the morphology of nanoparticles and their aggregation, bottom-up approaches have the advantage that size, shape, and even agglomeration can be controlled [43, 44]. In this work, nanoparticles produced using the bottom-up approach of hot wire thermal catalytic pyrolysis [45, 46] were used to compare with particles produced using top-down milling approach as explained in section 4.3.

2.1.2 Top-down production of silicon nanoparticles

Top-down production of nanomaterials involves size reduction processes whereby bulk solid materials are reduced to nanoscale dimensions. The process of size reduction is defined as the mechanical breakdown of solids into smaller particles without changing their state of aggregation [47]. Large scale production of silicon nanoparticles has been achieved using "top-down" approaches such as mechanical milling [48] and laser ablation [49]. Figures 2.2a and 2.2b are examples of Si nanoparticles produced using the top-down approaches, ball milling and laser ablation respectively.

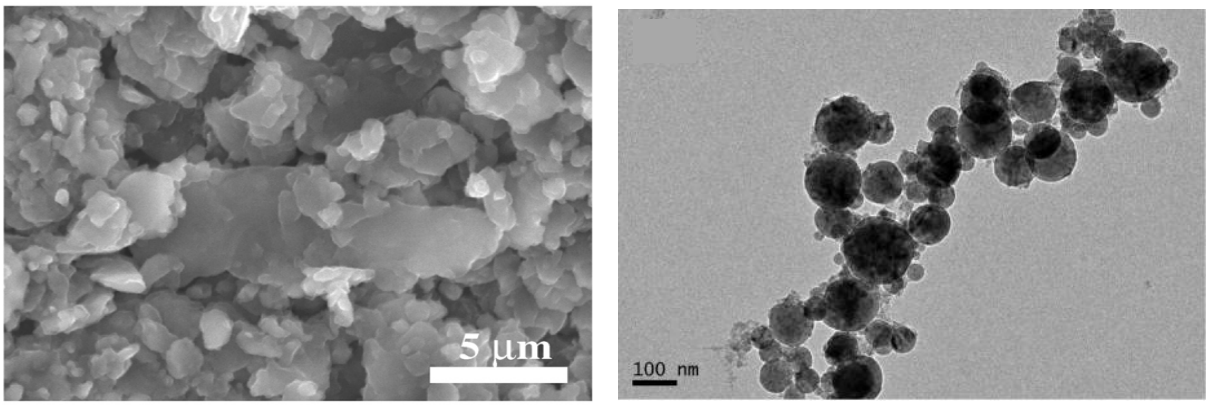

(a) (b)

Figure 2.2: Silicon nanoparticles produced using top-down approach, with (a) SEM observation of 20 hours milled Si nanoparticles produced using ball milling [48], and (b) TEM observation of Si nanoparticles prepared by laser ablation [49].

The two examples of particles shown in figure 2.2 definitely show different morphologies. In the ball milling process (figure 2.2a), particles with a broad size distribution and irregular shapes were obtained. Besides obviously very large particles, there are a multitude of smaller particle aggregates composed of even smaller particles in the nanoscale as shown in [48] after further treatment of the sample. The laser ablation process (figure 2.2b) on the other hand, produces particles which appear to be spherical in shape, but also with a broad size distribution. Without a further process to separate the varying particle sizes in the above micrographs, it is difficult to resolve the size of individual particles because of the nature of the aggregates formed by the particles [48, 50]. In general, it can be noted that using the top-down approach, size and shape of particles cannot be easily controlled, so non uniform nanoparticles with polydisperse size distributions are usually produced. The majority of

particles investigated in this work were produced using high energy milling as described in section 4.1.1.

2.2 Aggregation of nanoparticles

Irrespective of how nanoparticles are produced, the particles tend to combine to form complex structures which are referred to as aggregates [51]. These complex structures have been described using the concept of fractals [52], with an important parameter known as the fractal dimension d_f used to characterise their morphology. This concept will be described further in section 3.1.1. From simulations, two principal mechanisms can be identified which govern aggregation of nanoparticles: diffusion limited cluster aggregation (DLCA) [53]; and reaction limited cluster aggregation (RLCA) [54]. Figure 2.3 shows the type of structures expected for each aggregation mechanism by simulation involving 256 nanoparticles [55].

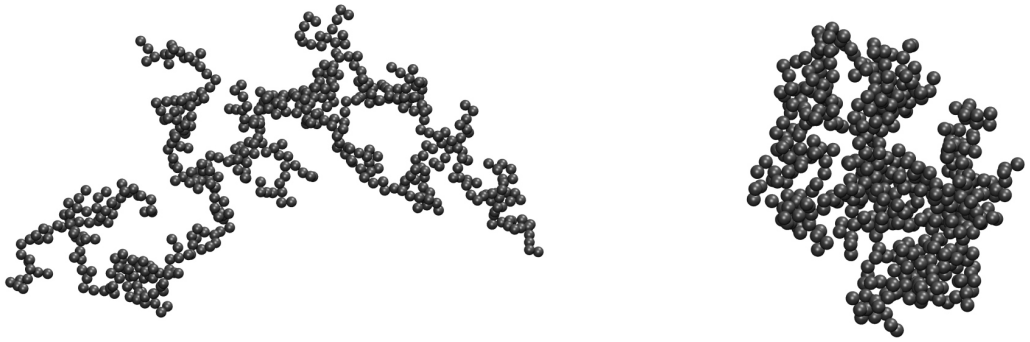

(a) (b)

Figure 2.3: Two dimensional projection of fractal aggregates of 256 nanoparticles using (a) the DLCA mechanism with $d_f = 1.8$, and (b) the RLCA mechanism with $d_f = 2.5$ [55].

In aggregates formed by DLCA (figure 2.3a), very little rearrangement of the particles occurs by diffusion and hence the nanoparticles form an open structure due to a strong attraction between particles with strong bonds between them. From the literature, aggregates of this nature are reported to have a low fractal dimension, d_f of about 1.8 and a coordination number of about 2.2 [56, 57]. On the other hand, a more compact aggregate structure is obtained by RLCA mechanism as shown in figure 2.3b. In this case, strong bonds do not exist between the particles in the aggregate, and the slower rate of the formation of the aggregates allows a rearrangement of the particles. A fractal dimension of about 2.1 have been reported

in the literature for the RLCA, but higher dimensions could be achieved by restructuring the aggregates [58] as indicated by the more dense configuration of the clusters seen in figure 2.3b. Experimentally, similar aggregate features have been reported for nanoparticles using scattering of X-rays [59] or light [60], but only the fractal dimension and size of the aggregates are usually reported. No reports have been found in the experimental scattering work on the quantification of the nanoparticles that make up an aggregate structure, or fully describe the topology of nanoparticulate aggregate. The use of scaling parameters to quantify aggregate structures from USAXS data as described in section 3.2 is one of the main concerns of this work, which allows on the example of silicon nanoparticle networks in an aggregate to extend the applicability of this scattering technique.

3. Small Angle X-ray Scattering and the Scaling Laws

Small angle scattering (SAS) was first developed by Guinier [61], with subsequent contributions from Porod [62, 63], Debye [64, 65], and Kratky [66, 67] helping to develop the theoretical background and the experimental procedures. The strength of this technique is its potential to resolve inner structures of inhomogeneous disordered systems including particle shapes, which was demonstrated in the early works of Guinier *et al.* for dilute and concentrated polymer solutions [68]. In SAS experiments, X-rays [69, 70, 71], neutrons [72], and visible light [73, 74] are used as probing radiation. Though all three types of radiation probe materials differently, the same methods are used in analysing the experimental data.

This chapter sets the framework for small angle X-ray scattering (SAXS) which is exclusively used in this work, and also sets the background for understanding the new scattering techniques discussed in section 4.3.3. In the second section, a new approach to analyse aggregates of nanoparticles is presented, and how the approach can be applied to SAXS data will be described.

3.1 Theory of SAXS

When radiation of wavelength, λ is incident on features much larger than the magnitude of λ, the intensity of the scattered radiation for very small angles is determined by irregular large scale variations in the electron density of the material given by its microstructure. This is the basic principle that governs SAXS experiments, and the small angles of incidence in SAXS correspond to the zeroth order of diffraction.

In X-ray scattering, when an incident photon interacts with electrons in a system, its momentum is changed from its initial momentum $\mathbf{k}_i$ to a final momentum $\mathbf{k}_f$ as illustrated in Fig. 3.1. The scattered wave vector $\mathbf{q}$ can then be defined as

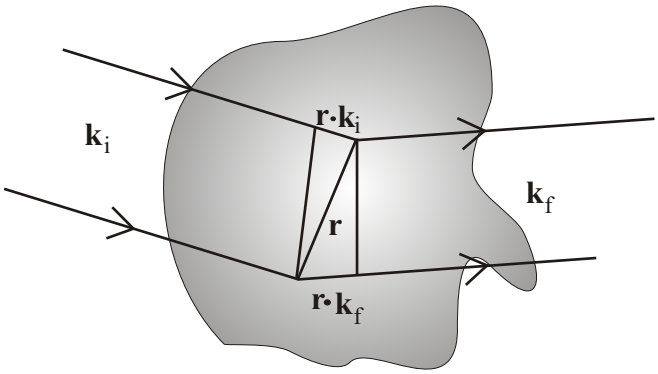

Figure 3.1: Scattering of photon by electrons in an object. Modified after Guinier and Fournet [68].

$$\mathbf{q} = \mathbf{k}_f - \mathbf{k}_i, \tag{3.1}$$

and the magnitude of the scattering vector is given as

$$q = \frac{4\pi}{\lambda}\sin(\theta) \tag{3.2}$$

where λ is the wavelength of the incident beam and the scattering angle is 2θ. The magnitude of the scattering vector q is related to a Bragg spacing d by the relation

$$d = \frac{2\pi}{q}. \tag{3.3}$$

Thus q is expressed in inverse length units which are usually Å^{-1} or nm^{-1}. In the scattering process illustrated in Fig. 3.1, the scattering amplitude $F(\mathbf{q})$ of the irradiated volume at the position $\mathbf{r}$ occupied by an atom is given by [64, 75]

$$F(\mathbf{q}) = \int_V \rho(\mathbf{r}) e^{i\mathbf{q}.\mathbf{r}}. \tag{3.4}$$

The scattering intensity measured from a single scatterer is given by the product of the scattering amplitude and its complex conjugate. This can then be written in the form

$$I(q) = \int_V \rho(r)^2 e^{iqr}. \tag{3.5}$$

For symmetric objects, the distribution of $\rho(r)^2$ in equation 3.5 depends only on the magnitude of $\mathbf{r}$. Considering the symmetry over all directions and using the Debye formula given as [68, 75]

$$\left\langle e^{iqr} \right\rangle = \frac{\sin(qr)}{qr}, \tag{3.6}$$

equation 3.5 can be simplified to the form

$$I(q) = \int 4\pi r^2 dr \rho(r)^2 \frac{\sin(qr)}{qr}. \tag{3.7}$$

The analytical solution to equation 3.7 for a symmetrical sphere of radius R has been solved [68, 75]

$$I(q) = (\Delta\rho)^2 V^2 \left\{ 3\frac{\sin(qR) - qR\cos(qR)}{(qR)^3} \right\}^2. \tag{3.8}$$

A more general approximation of equation 3.8 can be written as

$$I(q) = (\Delta\rho)^2 V^2 P(q), \tag{3.9}$$

where $P(q)$ is the form factor of a single scatterer, V is the volume of the particle and $\Delta\rho$ is the electron density of the scatterer in a vacuum, or if the scatterer is in a medium with non-zero electron density, it is the difference between the two densities [75, 76]. Basic scattering laws such as the Porod and Guinier laws can be derived using equation 3.9 as discussed below.

3.1.1 Porod and power scaling laws

Porod's law was derived for particulate systems with sharp interfaces [77, 78]. This is observed at very high q-values of SAS data where the length scale is sufficiently small so that the surface of the scatterer can be regarded as smooth or locally flat. For very high q-values, the form factor in equation 3.8 is proportional to q^{-4}, leading to the derivation of the scattering law for sharp interfaces which is given as [75]

$$I(q) = \frac{(\Delta\rho)^2 2\pi S}{q^4} : q \to \infty, \tag{3.10}$$

where S is the surface area. Equation 3.10 is known as Porod's law when the intensity drops with a power of -4 in plot of $\log I(q)$ versus $\log q$.

A deviation from the Porod power of -4 is often observed in SAXS experiments. This can be attributed to the nature of the scattering object. Since the intensity of the scattering is still proportional to a negative power of the scattering vector q, a more general equation derived from equation 3.10 to describe power laws is given as [78, 79]

$$I(q) = I_o q^{-\alpha}, \tag{3.11}$$

where I_o is a constant and α is the power law exponent which is obtained from a plot of $\log I(q)$ against $\log q$. In SAXS, the value of α is used to deduce if the scattering object has a mass or surface fractal property as described below. The concept of fractals was introduced to describe structures that do not scale as regularly as the structures which follow the scaling laws of normal Euclidean geometry [24, 52]. Such structures are described as having fragmented shapes with irregular patterns that display self-similarity with change in scale. This concept of fractals has been used to describe properties of disordered objects in SAS [80, 81], though not all fractal structures can be said to have the self similar property with change in scale.

Mass fractals are substances or structures whose mass and surface are characterised by fractal properties [79], and they often are aggregates of subunits [78]. For a mass fractal object of size R, the mass or the volume is said to scale as [24, 78]

$$M \propto R^{d_f}, \tag{3.12}$$

where d_f is the mass fractal dimension which has values in the range $1 < d_f < 3$ [24, 78, 82]. This important parameter depends on the dimensions of the scattering object, because the dimension of an object cannot be higher than the space it is embedded in [24]. For example, the structural dimensions for a rod, a disc and a sphere are 1, 2 and 3 respectively. The mass fractal dimension d_f is related to the power law exponent as $\alpha = d_f$ [83, 84].

Surface fractals are structures whose surfaces are characterised by fractal properties, but the mass or volume does not [79]. In this case, the surface S varies in relation to the size R as

$$S \propto R^{d_s}, \tag{3.13}$$

where d_s is the surface fractal dimension. The relationship between the power law exponent α and d_s is given as [82, 83, 85]

$$\alpha = 2d_f - d_s. \tag{3.14}$$

For surface fractals, $2 < d_s < 3$ and $d_f = 3$ so that $3 < \alpha < 4$. When $d_s = 2$, then equation 3.11 becomes Porod's law for a sharp interface.

3.1.2 Guinier's law

Guinier's law describes scattering from an isolated particle assuming that coherent scattering of X-rays occurs between different regions of the particle [61, 75, 86]. At very small angles,

Guinier showed that the scattered intensity can be described by the equation

$$I(q) = I_o \exp(-q^2 R_g^2/3). \tag{3.15}$$

In this equation, R_g is the radius of gyration which is defined as the mean square distance of electrons from their centre of distribution [75]. In this case, R_g corresponds in some form to a distribution in space, which can be associated with the geometry of the scattering objects. For example, the radius R of an isolated spherical object is related to the radius of gyration by the equation [87, 88, 89]

$$R_g^2 = \frac{3}{5} R^2. \tag{3.16}$$

Similar equations can be obtained for the cross section of a thin rod or the thickness of a disc. From equation 3.15, R_g can be obtained from a plot of $\ln I$ versus q^2, and in a plot of $\log I$ versus $\log q$ it can be observed as an exponential decay which terminates a power law decay at the low q region where $qR_g \ll 1$ [77]. This region of exponential decay also known as a "knee", is often observed in scattering spectrum of particulate systems that approximate spherical structures [84]. It should be noted that the Guinier approximations were obtained assuming isolated scattering particles, so that R_g is related to the particle size. In a dense particulate system, R_g is the correlation length [75, 87, 89], which is the probability of finding a similar scatterer from a reference scattering particle. The correlation length can therefore be attributed to the distance between the scattering particles and this is equivalent to the diameter of the particles in a close-packed system [75].

3.1.3 Unified Guinier-exponential/power-law Equation

The power and exponential laws described in sections 3.1.1 and 3.1.2 can be used to describe structural and dimensional features of particles in the high q ($qR_g \gg 1$) range as well as the low q ($qR_g \ll 1$) range [82, 90]. Independently, these laws are not sufficient to distinguish scattering from different topological features due to a loss of phase information which is inherent to static scattering [26]. However, combining the different fractal features described by these laws can generate new information that can be used to extract the topology of fractal aggregates from a scattering curve with multiple regimes [26]. A unified equation that combines both the power and exponential laws without the addition of any new parameter has been given as [77, 84]

$$I(q) = G \exp\left(\frac{-q^2 R_g^2}{3}\right) + B(q^*)^{-\alpha}. \tag{3.17}$$

In equation 3.17, $G = N_p n_e^2$ is the exponential prefactor, and $B = 2\pi G S_p / V_p^2$ is a constant prefactor specific to the type of power law observed in a scattering curve determined by the regime in which α falls. S_p and V_p are the surface area and volume of the primary particles respectively. The variable q^*, in equation 3.17, arises from a modification of the power law to ensure it accounts for finite structures [77]. The modified q^* is given as

$$q^* = \frac{q}{\left[\text{erf}\left(qR_g/\sqrt{6}\right)\right]^3}, \tag{3.18}$$

where erf() denotes the error function.

Equation 3.17 can also be extended to describe, not just the first structural level which are mostly from primary particles in an aggregate, but structures with inter related multiple-size-scale features [77, 84]. The extended equation is expressed as

$$I(q) \approx \sum_{i=1}^{n} G_i \exp\left(\frac{-q^2 R_{g,i}^2}{3}\right) + B_i \exp\left(\frac{-q^2 R_{g,(i+1)}}{3}\right) \left(\frac{\left[\text{erf}\left(qR_{g,i}/\sqrt{6}\right)\right]^3}{q}\right)^{\alpha_i}, \tag{3.19}$$

in which, $i = 1$ refers to the smallest-size structure observed in an experiment. Each level of structure is described by the radius of gyration, R_g, a power law slope, α, a Guinier prefactor, G and a power-law prefactor, B. Identifying these values gives a description of the morphology and dimensions of the structure under investigation at different length scales.

All equations discussed so far correspond to scattering from non-correlated particle domains. For correlated systems in which scattering contributions from different particles cannot be ignored due to increased concentration, a modification to the scattering intensity is given by [84, 91]

$$I(q) = AF(q)^2 S(q), \tag{3.20}$$

where $AF(q)^2$ corresponds to the intensity in equation 3.5, and $S(q)$ is a structure factor accounting for the weakly correlated particle domains. The structure factor is described for the correlation of spherical colloidal particles or domains in terms of the inter-particle distance ζ and the packing factor, κ by [68, 91]

$$S(q) = \frac{1}{1 + \kappa\theta(q)}, \tag{3.21}$$

where $\theta(q)$ is the structural correlation "form factor" given as

$$\theta(q) = 3\frac{\sin(q\zeta) - q\zeta\cos(q\zeta)}{(q\zeta)^3}. \tag{3.22}$$

For weakly correlated systems, both the radius of gyration R_g of the particles and the radius of correlation ζ are expected to be observed with the property that $R_g \leq \zeta$. For multiple structural fitting using the unified function in equation 3.19, any level with a correlated relationship can be modified according to equation 3.20. Both the non-correlated intensity and the correlated intensity functions will be applied to describe particulate systems in this work.

3.2 Aggregate scattering and scaling laws in SAXS

In this section, a new scaling model to extract the topology of fractal aggregates of nanoparticles will be described. The model was originally developed to quantify branching features of polymers from scattering data [26, 27]. The scaling model has been used successfully to describe the branch content of polyethylene chains [28], and the folding states in proteins and ribonucleic acid [27]. For the first time, this model will be used in this work to quantify aggregates of nanoparticulate systems [70, 71] using X-ray scattering data. This approach is a step towards understanding how particles aggregates in printed layers, and how the structural features could affect the layer properties such as electrical performance. Information from this scaling model will be used to support the results from the new surface scattering technique described in section 4.3.3.

3.2.1 The Scaling model

In the scaling model, a fractal aggregate of particles is represented by the two dimensional branched aggregate structure shown in figure 3.2. The branched aggregate of size R and fractal dimension $\alpha_2 = d_f$ is composed of a number z of primary particles which corresponds to all the circles in the figure. z is known as the degree of aggregation or mass of the aggregate. Also considered is an average minimum path (*open circles*) with a number p of primary particles that span through the size of the aggregate. The minimum path, which has a minimum dimension d_{min}, describes how tortuous or convoluted the aggregate structure is [27, 71]. The aggregate structure can also be described in terms of a connectivity path, s represented by the straight lines joining branch points and free ends in the figure. The connectivity path s with its associative dimension c describes the branching characteristics of the aggregate. A relationship connecting z, p and s is given as [27, 71]

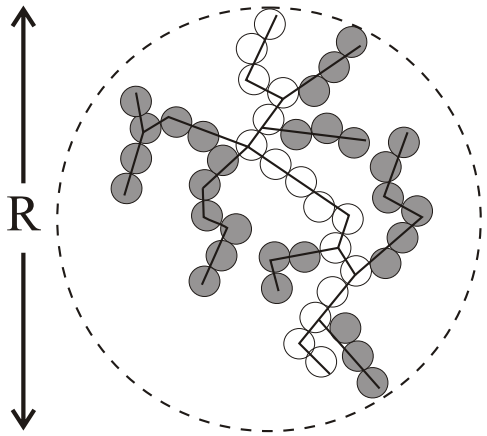

Figure 3.2: Illustration of aggregate structures in two dimensions composed of similar primary particles. The aggregate is composed of z number of primary particles (*circles*) known as the degree of aggregation or mass of the aggregate. An average minimum path (*open circles*) with p number of primary particles and fractal dimension d_{min} that spans the size of the aggregate is shown. The *straight lines* represent the connectivity path of the aggregate with a fractal dimension c [71].

$$z = p^c = s^{d_{min}}, \tag{3.23}$$

where z is seen to be related to the minimum path through the connectivity dimension and also related to the connectivity path through the dimension of the minimum path. The aggregate overall size R can be obtained from the scaling relationship by

$$R = z^{1/d_f} = p^{1/d_{min}} = s^{1/c}. \tag{3.24}$$

By combining equations 3.23 and 3.24, c, d_f and d_{min} can be shown to be related by

$$d_f = cd_{min}, \tag{3.25}$$

where $c \leq d_f$ and $d_{min} \leq d_f$. Equation 3.25 implies that the knowledge of the aggregate in just two dimensions can be used to describe its three dimensional structure. Values of c, d_f and d_{min} for some known shapes have been given in [27]. Following from the above scaling relationships, the branch fraction of the aggregates ϕ_{br}, which is the fraction of the structure that is not included in the minimum path, is given by [26, 27, 71]

$$\phi_{br} = \frac{z - p}{z} = 1 - z^{\frac{1}{c}-1}. \tag{3.26}$$

The end-to-end distance of the minimum path which should span through the aggregate size, R is given in terms of the average number of segments per minimum path, $n_{s,p}$ and the

minimum path, p by [71]

$$R = n_{s,p}\left(\frac{p}{n_{s,p}}\right)^{\frac{5}{9}}. \tag{3.27}$$

Each segment is considered to possess an intrinsic fractal dimension of ≈ 1.8, as has been obtained for diffusion limited cluster aggregates DLCA in the literature by simulations [92, 93]. From equations 3.24 and 3.27, a relationship for $n_{s,p}$ is obtained as

$$n_{s,p} = \left[p^{\frac{1}{d_{min}}-\frac{5}{9}}\right]^{\frac{9}{4}}. \tag{3.28}$$

The average number of branch sites per minimum path is given as [28]

$$n_{br,p} = n_{s,p} - 1. \tag{3.29}$$

Defining n_{br} as the total number of branch sites in the whole aggregate, and the average number of branches emanating from each branch point f known as the average functionality of branching, the total number of effective end groups n'_e can be determined in terms of n_{br} and f as

$$n'_e = n_e + 2n_c = (f-2)n_{br} + 2. \tag{3.30}$$

The equation above was derived using the concept of free arms for polymers [94]. In equation 3.30, n_e is the number of the end groups in the aggregate and n_c is the number of cyclics which means the number of closed loops, whereby in the formation of an individual cyclic two end groups are needed. The total number of segments in the aggregate $n_{s,z}$, is one less than the number of branch points, therefore the effective end points in the aggregate can be given as

$$n_{s,z} = n_{br} + n'_e - 1 = (f-1)n_{br} + 1. \tag{3.31}$$

The average number of primary particles in each segment z_s, may be obtained by dividing the mass of the aggregate by the total number of segments in the aggregate,

$$z_s = \frac{z}{n_{s,z}}. \tag{3.32}$$

An equation for the total number of branches can be obtained from equations 3.23, 3.27, 3.28, 3.31 and 3.32 as

$$n_{br} = \frac{z^{\frac{9}{4d_f}-\frac{5}{4c}+(1-\frac{1}{c})} - 1}{f-1}. \tag{3.33}$$

The number of inner segments, n_i, which are segments not included in the minimum path, can be approximated by [28]

$$n_i = n_{br} - n_{br,p}. \tag{3.34}$$

The average coordination number, C_N, which is a measure of average number of primary particles attached to a primary particle in the aggregate (neglecting free ends) [95], is given by

$$C_N = \frac{2z + (f-2)n_{br}}{z}. \tag{3.35}$$

Considering branches emanating from the minimum path at a branch point, the average number of primary particles per branch z_{br} is the mass of branches ($z\phi_{br}$) divided by ($f-2$), which accounts for the number of branches emanating from each branch point multiplied by the number of branch points on the minimum path $n_{br,p}$

$$z_{br} = \frac{z\phi_{br}}{(f-2)n_{br,p}}. \tag{3.36}$$

The functionality, f could be determined from microscopy, if the branches of the aggregates can be resolved accurately. It is therefore, reasonable to assume that the branch points are mutually exclusive, i.e., $f = 3$, in which case [28]

$$n_{br} = \frac{z^{\frac{9}{4d_f} - \frac{5}{4c} + (1-\frac{1}{c})} - 1}{2}. \tag{3.37}$$

The parameters C_N, n_i, n_{br}, p and z_{br} may be obtained from the scaling relationships once n_{br} is calculated using equation 3.37. These scaling parameters can be obtained from SAXS data as described below.

3.3 Application of the scaling model to SAXS data

Using the unified function in equation 3.19, the scattering from both primary particles and their aggregates can be determined when the equation is used to fit the scattering data. Denoting the primary particle parameters with subscript 1 and the aggregate parameters with subscript 2, the scaling parameters can be obtained from the unified function parameters. The degree of aggregation z can be obtained from the Guinier prefactors G_2 and G_1 of the aggregate and primary particles respectively as [26, 96]

$$z = \frac{G_2}{G_1}. \tag{3.38}$$

Equation 3.38 was obtained assuming that the primary particles constitutes the aggregate structure. The minimum dimension, d_{min} is given by [27, 71]

$$d_{min} = \frac{B_2 R_{g,2}^{d_f}}{\Gamma(d_f/2)G_2}, \tag{3.39}$$

where $d_f = \alpha_2$ is the fractal dimension of the aggregates and $\Gamma()$ is the gamma function. Equations 3.38 and 3.39 can be used along with the parameters from the unified function to determine the values of the scaling model parameters.

The Sauter mean diameter d_p which is the average size of the primary particles is given by [96, 97, 98]

$$d_p = \frac{6Q}{\pi B_1}, \tag{3.40}$$

where B_1 is the Porod prefactor of the primary particles and Q is the Porod invariant determined from the scattering curve associated with primary particles (unified fit parameters with subscript 1). It is given as [75, 96]

$$Q = \int_0^\infty q^2 I(q) dq = 2\pi^2 r_e^2 N (\Delta\rho)^2 V. \tag{3.41}$$

d_p in equation 3.40 has been shown to reflect same moment of volume to surface ratio as the particle size obtained using Brunauer, Emmett and Teller (BET) [99] analysis of gas adsorption [96, 97]. From the Guinier and Porod prefactors in the unified function corresponding to the primary particles, a unitless ratio known as the polydispersity index (PDI) is given by [69, 96]

$$PDI = \frac{B_1 R_{g,1}^4}{1.62 G_1}. \tag{3.42}$$

The PDI is obtained directly from the scattering experiment without any assumption of particle shape. For a monodispersed distribution of spherical particles it has a value of 1 and this number increases when there is a distribution of sizes. When the PDI suggest a broad size distribution, an assumption of a log-normal distribution can be used since it can estimate all moments of the distribution [96]. The log-normal distribution function is given as [69, 96]

$$f(R) = \frac{1}{R\sigma\sqrt{2\pi}} \exp\left(\frac{-[\ln(R/m)]^2}{2\sigma^2}\right), \tag{3.43}$$

where m is the median and σ is the standard deviation of the logarithm of the size. For a distribution of spheres, the PDI and σ are related by the expression

$$\text{PDI} = \exp(12\sigma^2). \tag{3.44}$$

The geometric standard deviation σ_g is related to the index of polydispersity by [96]

$$\sigma_g = \exp(\sigma) = \exp\left(\sqrt{\frac{\ln(\text{PDI})}{12}}\right). \tag{3.45}$$

All the equations obtained in sections 3.2 and 3.3 will be used to characterise silicon nanoparticles printed on various substrates to understand the structural properties of the aggregates formed by the nanoparticles.

4. Experiment

In this chapter, the production of silicon nanoparticles, ink formulation and the printing processes used to deposit layers containing these particles will first be described. Secondly, the scattering methods used to study the morphology of the nanoparticles and their assembly in the layers will be discussed. Special emphasis will be given to describe the new scattering technique developed in the framework of this research to study the surface features of the assembly of nanoparticles. As a complementary technique, the electron microscopy methods which were used to study the as produced silicon nanoparticles as well as the printed layers will also be described.

4.1 Sample preparation

4.1.1 Production of nanoparticles

Silicon nanoparticles were produced by the top down process of high energy milling (HEM) [16], performed with a 800W Siebtechnik laboratory disc mill which is equipped with cylpeb dry milling media. By vibration, the mill applies a complex combination of impact fracturing forces and shear attrition forces [100] to reduce the size of bulk solids which are usually hard and abrasive [47]. For this work, 2503 grade metallurgical silicon (M-Si) supplied by Silicon Smelters, Polokwane, South Africa, and Czochralski grown P-type silicon wafers supplied by Siltronix, St Louis, USA, were used as feedstock materials in the milling process. Before milling, the pestles and pots were cleaned by milling quartz for few minutes and then wiped with ethanol and acetone. Milling times of 60, 90, 120, 150, 180 and 300 minutes were used to produce different powders. After milling, the pots were left to cool to room temperature before the nanoparticles were harvested and stored in plastic bottles under ambient conditions.

4.1.2 Ink formulation and layer deposition

The silicon nanoparticles investigated were used in two different ink systems: a solvent-based ink in which cellulose acetate butyrate (CAB) (Goodfellow, Ltd, UK) was dissolved in industrial grade lacquer thinners, and a water-based ink using a commercial acrylic emulsion

screen printing base (Marchem (Pty) Ltd, South Africa). In the water-based ink, in which the acrylic monomer polymerizes by hydrolysis at ambient temperature [101, 102], propan-1, 2-diol (propylene glycol) was used as a solvent as well as a retarder. The composition of the inks were determined by weight ratios of the silicon nanoparticles and the required binder. Inks were produced with 20%, 50%, 60%, 70% and 80% particles by weight mixed with the complementary weight of binder. Two different methods were used to mix the inks:

(a) **sonication**: In this method, the powder, binder and thinner were mixed in a bottle and then sonicated for periods of as long as 1.5 hours at 30 minutes interval. This long sonication time was chosen to ensure a proper mixture of the binder, thinning liquid and the particles.

(b) **hand**: This method required the addition of the powder and thinner sequentially to the full amount of binder with mixing performed by hand.

In both cases, the thinners were used to obtain inks with viscosity suitable for printing [16, 70].

To deposit the inks onto different substrates, two methods were used: blade coating and screen printing. In the blade coating method, a glass rod was used to spread the ink onto the substrate to obtain a uniform layer [69, 70]. For screen printing, an ATMA AT-60PD semi-automatic flatbed screen printer was used to form defined pattern of the silicon nanoparticle inks, as seen in figure 4.1 as an example. The sizes of the samples were adapted to the requirements of the measurment techniques employed in this work, and are described below. For this study, three types of substrates differentiated by porosity were used. They include porous 80 gsm plain paper, aramid paper which is semi-porous, and non-porous 100 μm polyethylene terephthalate (PET) film. After depositions, the printed layers were left to cure under ambient conditions before any measurement or further processing was carried out. The type of particles investigated, the milling times for the top-down produced particles, ink systems, type of deposition and substrates used are mentioned in the relevant section describing each of the different experiments.

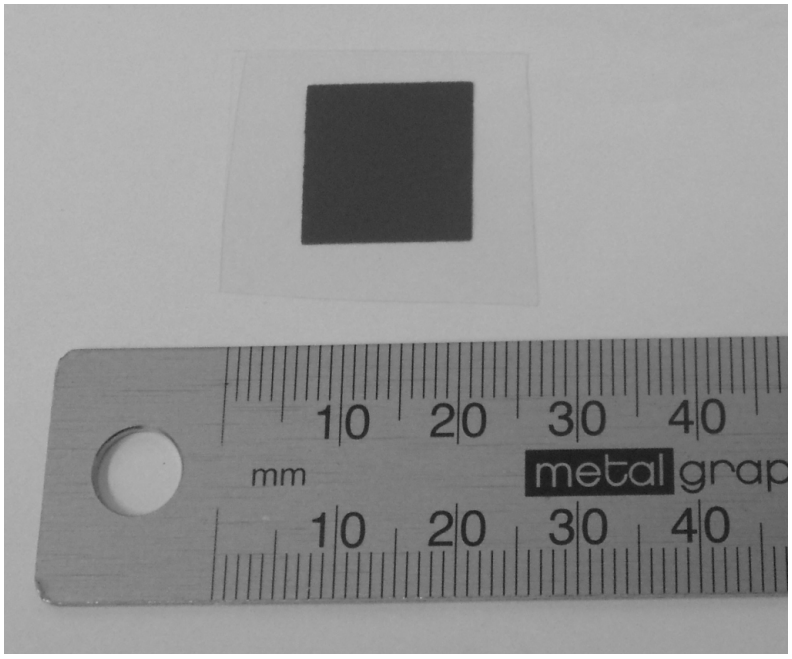

Figure 4.1: Example of a defined pattern of metallurgical grade silicon particle layer produced by screen printing on a PET substrate.

4.2 Electron microscopy

4.2.1 Transmission Electron Microscopy

A FEI F20 field emission gun transmission electron microscopy (FEGTEM) operated at 200 kV, was used to acquire images of the nanoparticles at low magnification. The microscope is equipped with a Gatan imaging camera which was set to acquire images of size 4096 $\times$ 4096 pixels at a pixel resolution of 1 Å. To enhance the contrast of the particles, all images were taken at a constant defocus of -2 μm. To determine the size distribution of the particles, a series of images were taken at different positions on the TEM grids.

The TEM sample was prepared by placing a small amount of metallurgical silicon nanoparticle powder milled for 5 hours into methanol [103], and sonicating the mixture for few seconds to break up agglomeration of the nanoparticles. A pipette was used to place a drop of the mixture on to plain carbon coated TEM grids, and the sample was left to dry under ambient conditions. A manual method using ImageJ v.1.42q [104, 105] software as described

in [106] was applied to determine the particle size by measuring the long and short axes of more than 3400 silicon nanoparticles of the particular sample.

4.2.2 Scanning Electron Microscopy

A Nova Nano SEM 230 with beam energy settings from 10 keV to 15 keV and a current of 200 pA was used in secondary electron imaging mode to study the morphology of printed layers containing aggregates of the silicon particles milled for 5 hours. The aggregation of the particles on the sample surface gives an impression of the expected features within the bulk of the printed layers. To mount the samples in the microscope, the printed layers were cut to size, and mounted on aluminum stubs. The printed layers were carbon coated using an evaporation coater to enhance the image quality at higher magnification by reducing charging at high points on the surface [107].

4.3 Scattering techniques

4.3.1 Laboratory SAXS/USAXS

The laboratory based small angle X-ray scattering experiment set-up manufactured by Molecular Metrology (Northampton, MA) for which the principle features are shown in figure 4.2, uses CuK_α radiation with a wavelength of $\lambda = 1.54$ Å from a point source X-ray tube. The three pinhole collimation system consists of the two collimating pinholes which provide a small circular spot on the sample structure. The guard pinhole blocks parasitic scattering which could result from edge scattering from the second pinhole [108]. A two dimensional camera positioned 1.30 m from the sample, detects the circular scattering pattern. In this transmission configuration, the instrument measures a q range of approximately 0.01 to 0.2 $Å^{-1}$ [71].

To increase the q range, a laboratory based Bonse-Hart camera manufactured by Advanced Metals Research Corporation (Burlington, Massachusetts) was used for USAXS measurements. Both instruments are located at the Department of Chemical and Materials Engineering, University of Cincinnati, Cincinnati, Ohio. The USAXS instrument also uses CuK_α radiation, but with a line source. An illustration of the principles of the USAXS instrumentation is shown in figure 4.3, with the collimating channel cut silicon single crystal between

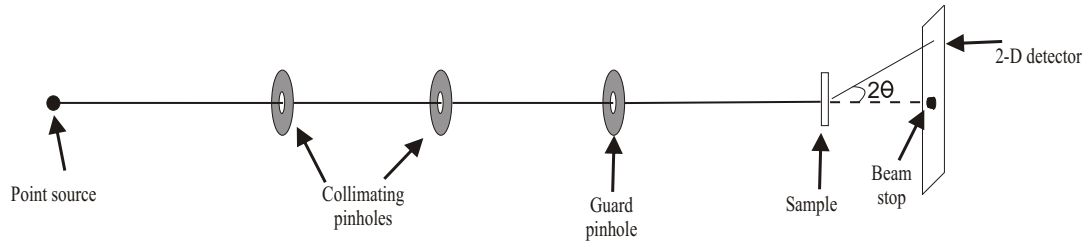

Figure 4.2: Schematic of the pinhole SAXS setup

the X-ray source and the sample acting as a monochromator and to provide a nearly parallel beam. The analysing channel cut silicon crystal between the sample and detector uses the same 220 Bragg reflection as the collimator. By rotating the analyser together with the detector, the scattered intensity is measured as a function of q for each angular orientation. A q range of approximately 0.0001 to 0.1 $Å^{-1}$ was achieved using this set-up [71].

The samples investigated using both laboratory systems, were blade coated layers of silicon on PET (see section 4.1.2) produced from a water based ink containing 5 hour HEM M-Si particle with a 80% to 20% particle to binder weight ratio. 3×2 cm strips with a uniform thickness of silicon particle layer, as well as a strip from the PET substrate coated with only the binder as a reference sample, were cut for easy mounting in the equipments. The measured data were corrected for the substrate and binder signal using small-angle scattering profiles of the reference sample. Irena and Indra software packages [109] (available at usaxs.xor.aps.anl.gov) were employed to correct and desmear the SAXS/USAXS data using the Lake method [110].

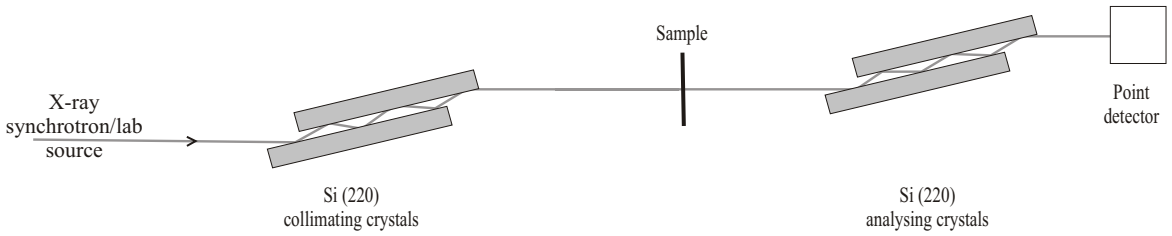

Figure 4.3: Principle of a USAXS experiment shown in one-dimensional collimation configuration. The set-up uses Si (220) channel cuts as the collimating and analysing crystals. After [109]

4.3.2 Synchrotron USAXS

For advanced studies to facilitate higher radiation intensities [109, 111], synchrotron USAXS measurements were conducted at sector 15ID of the Advanced Photon Source, Argonne National Laboratories [109]. The instrument is a one dimensional Bonse-Hart set-up, with the same principle as the laboratory set-up shown in figure 4.3, but which operates on a variable X-ray range of 8 to 19 keV [109]. A wavelength of 0.733 Å (16.899 keV) was used for all the measurement performed in this work, resulting in a q range of approximately 0.00015 to 0.1 $Å^{-1}$ [70]. A series of samples were prepared by cutting small strips of the printed layers to a size that fitted in the circular openings of the 1 cm diameter sample holder. Different types of samples as described below together with the appropriate reference samples, were measured to investigate the properties of the printed layers with respect to the different production methods and material systems used. The same methods to those mentioned in section 4.3.1 above were used for the data correction.

(a) **Influence of particle production, ink formulation and substrate used on the aggregation of silicon nanoparticles**

Layers of silicon nanoparticles blade coated on two different substrates, paper and PET, with differently produced nanoparticles and ink formulations, were investigated to study how these variations affect the structural features of the nanoparticle aggregates. For the top-down produced particles listed in table 4.1, metallurgical grade silicon were high energy milled for 5 hours. For comparison, silicon nanoparticles produced by the bottom-up process of thermal catalytic pyrolysis (TCP) [45, 46] of silane were also investigated. The samples were produced from water and solvent based inks prepared by hand mixing and sonication (see section 4.1.2) respectively, with a 80% to 20% particle to binder ratio. Reference samples were also prepared by blade coating the binders on the respective substrates used.

(b) **Influence of particle concentration and substrates used on the aggregation of silicon nanoparticles in screen printed layers**

The effect of the concentration of nanoparticles in printed layers on the structural features was studied using the 5 hour HEM M-Si particles. Water-based inks were prepared with particle concentrations of 80%, 70%, 60% and 50% by weight. Hand mixing were performed to obtain screen printable inks. These inks were screen printed on to paper,

Table 4.1: Specifications of the blade coated silicon nanoparticle samples with respect to the ink systems and substrates used for synchrotron USAXS measurements following investigations in 4.3.2(a).

Sample ID	Si nanoparticles	Binder	Substrate
HEM1	high energy milled	Acrylic	Paper
HEM2	high energy milled	Acrylic	PET
HEM3	high energy milled	CAB	Paper
HEM4	high energy milled	CAB	PET
TCP1	synthesized by TCP	Acrylic	Paper
TCP2	synthesized by TCP	Acrylic	PET
TCP3	synthesized by TCP	CAB	Paper
TCP4	synthesized by TCP	CAB	PET

aramid paper and PET to produce twelve different samples. The reference samples were the different substrates on which only a layer of the acrylic binder was printed.

(c) **Influence of the milling time on the aggregation of silicon nanoparticles in printed layers**

Size reduction of bulk solid materials to nanoparticles using milling is expected to decrease exponentially with time [100]. The influence of M-Si particles milled for 1 hour, 1.5 hours, 2 hours, 2.5 hours, and 3 hours on the aggregation was investigated with screen printed layers produced from water-based inks containing 70% particle weight ratio on PET. Nine samples of each composition were measured.

(d) **Influence of particle concentration on the aggregation of silicon nanoparticles in printed layers**

The influence of particle concentration was also investigated for M-Si nanoparticles milled for 1.5 hours, with similar concentrations and ink formulation as described in 4.3.2(b). Some of these samples were also investigated for electrical properties as discussed in section 4.4 below.

4.3.3 Wide Angle Low q scattering

All the scattering experiments described so far probe the internal structures of the printed layers, with no information regarding the surface features. A new scattering technique described here was designed to investigate the surface features of the printed layers with the aim to obtain information of the topology of the particle networks on a presumably rough surface. The surface of a printed layer is of particular importance in printed electronics especially since compatibility between active layers and electrodes [17, 112] affects the properties of devices.

The principle of the set-up for the experiment is shown in figure 4.4, which has the classic reflection geometry used in X-ray powder diffraction [113]. It uses the same geometry as in a θ-2θ scan but to measure scattering of the incident beam due to the surface alone, so as to maintain the direction of the scattering vector $\mathbf{q}$ perpendicular to the plane of the sample. One basic difference to the above described techniques is in the choice of the X-ray wavelength and the minimum angle of incidence. An incident beam with long wavelength is used to probe the sample material at angles greater than its critical angle and generally below the diffraction angle for the first diffraction peak. At the minimum incident angle used with soft X-rays on surfaces with micron scale roughness, the reflectivity is effectively zero. Hence, this avoids total external reflection from the surfaces, but the low penetration depth for the soft X-rays restricts the observable scattering to the near surface region. The magnitude of the scattering vector $\mathbf{q}$, which is in the direction perpendicular to the substrate, can be described with equation 3.2.

In other SAXS experiments, low q-values, corresponding to very large Bragg spacing, are obtained with short wavelength high energy radiation (8 - 17 keV) scattered at small angles [114]. In contrast, in this experiment, similar values are obtained using low energy long wavelength radiation scattered at wide angles; hence the description wide-angle low q (WALq). The primary aim is to observe the diffuse scattering features as measured by SAS for bulk material, below the diffraction peaks of a diffraction experiment for the surface of the material under investigation.

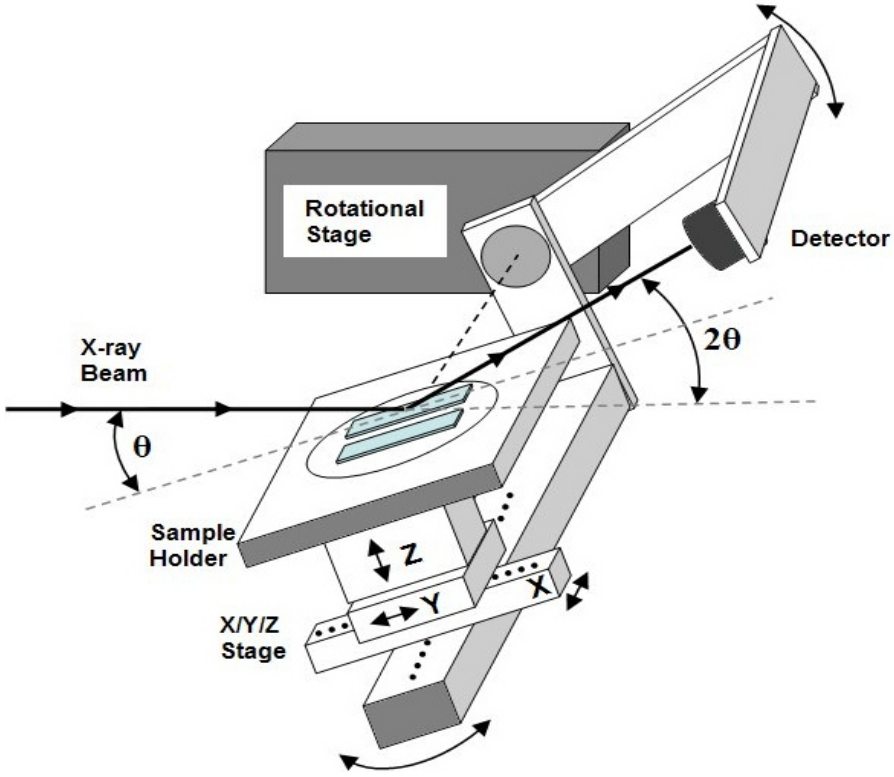

Figure 4.4: Schematic of the sample stage and detector position used for the new experiment.

The differences between WALq and other SAS methods are illustrated in figure 4.5. For transmission SAS experiments (figure 4.5a), the scattering vector is in a direction perpendicular to the incident beam. There is no momentum transfer, or scattering, in the direction perpendicular to the sample surface (i.e. $q_z = 0$), thus surface features are not investigated [115]. In X-ray reflectometry (XR) shown in figure 4.5b, the momentum transfer is in a direction perpendicular to the surface of the sample (i.e. $q_z \neq 0$, $q_y = 0$). To obtain significant external reflection, the X-rays have to be incident at grazing angles similar to the critical angle of the material under investigation. This implies, not only, that only the features that lie on the surface can be investigated, but that XR can only be performed on samples with near atomically smooth flat surfaces, i.e surfaces with nanometre scale roughness [116]. For example, using the software available at http://henke.lbl.gov/optical_constants/layer2.html, for a silicon surface with roughness of 1 μm, the reflectivity falls by over 9 orders of magnitude within 0.1° from grazing incidence for soft X-rays.

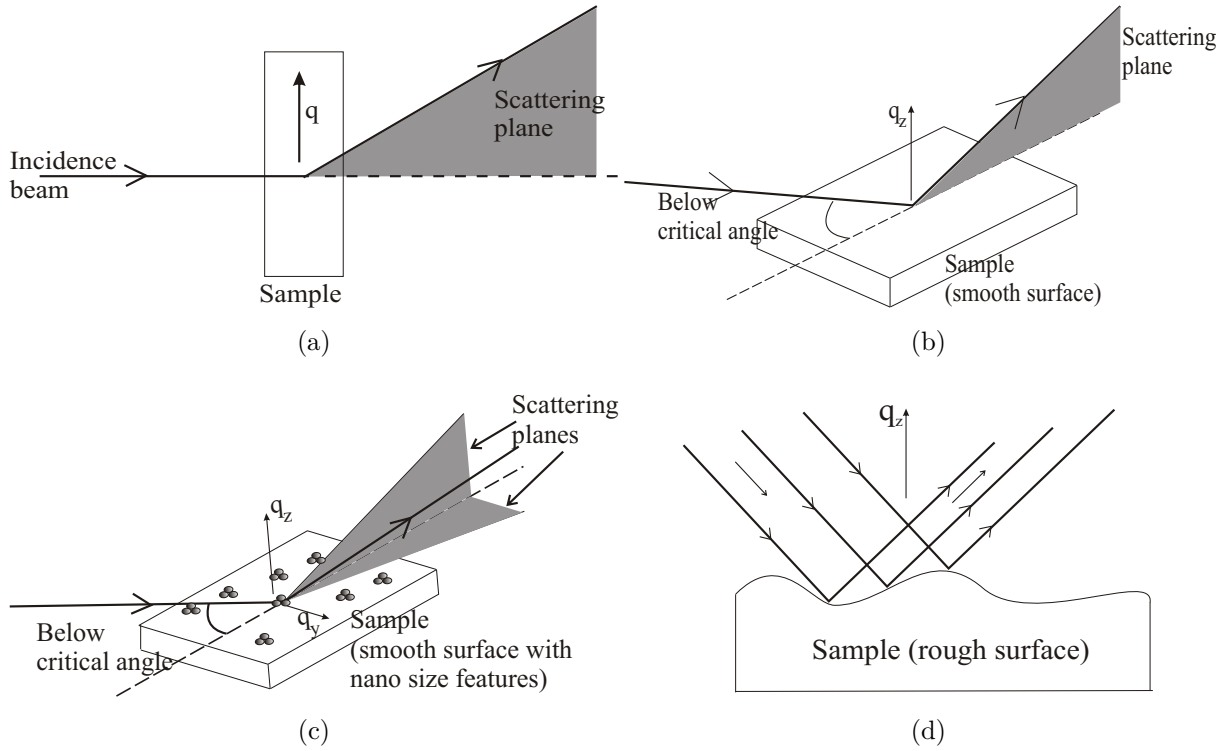

Figure 4.5: Experimental set-ups for (a) transmission SAS, (b) X-ray reflectometry and (c) Grazing incidence small angle X-ray scattering, showing the scattering planes and how they are different from (d) WALq set-up.

Grazing incidence small angle X-ray scattering (GISAXS) [117], where the principle is shown in figure 4.5c, is slightly different from XR because there is a net momentum transfer both parallel and perpendicular to the surface. Though the GISAXS method can be used to study nanoscale structures on surfaces, it also requires the sample to be similarly smooth to reflectometry, since the beam is also incident at grazing angles similar to the critical angle. For the new method of wide angle low q scattering, low energy X-rays are incident on rough surfaces (figure 4.5d) which have height differences of the order of several microns, for which external reflection does not occur. The direction of the momentum transfer is the same as in XR due to the detector position, but the X-rays are incident at angles greater than the critical angle for total external reflection. Thus, the X-rays penetrate the sample, albeit with a relatively short penetration depth. This is because the low energy X-rays required for WALq are easily absorbed by most materials; unlike the high energy short wavelength X-rays used in other SAS methods. At grazing incidence, shadowing of both the incident and reflected beam may occur depending on the surface feature shown in figure 4.5d. These effects can be prevented in this new method by choosing wider angles for both the incident

and the scattered beam.

(a) **Experimental set-up**

Beamline 6.3.2 of the Advanced Light Source (ALS) at the Center for X-ray Optics, Lawrence Berkeley Laboratory, University of California, Berkeley, CA, USA was used in this experiment. The beamline which operates in the energy range of 50 eV to 1300 eV was originally developed for the characterisation of optical elements such as mirrors, gratings, multilayers, detectors, etc. [118, 119, 120]. The beamline as shown schematically in figure 4.6 has a horizontal and a vertical focussing mirror with high focussing ability. It has a wavelength precision of 0.007%, wavelength uncertainty of 0.0123%, spectral purity of 99.98%, and dynamic range of 10^{10} [121]. The beamline is equipped with a two-axis vacuum goniometer to carry the sample and detector as shown in figure 4.4. The energy range provided by this set-up and the configuration of the sample stage, makes this an ideal instrument for the surface scattering experiment explained above. A full description of the beamline and its component is given in the published work of Underwood and Gullikson [119, 120].

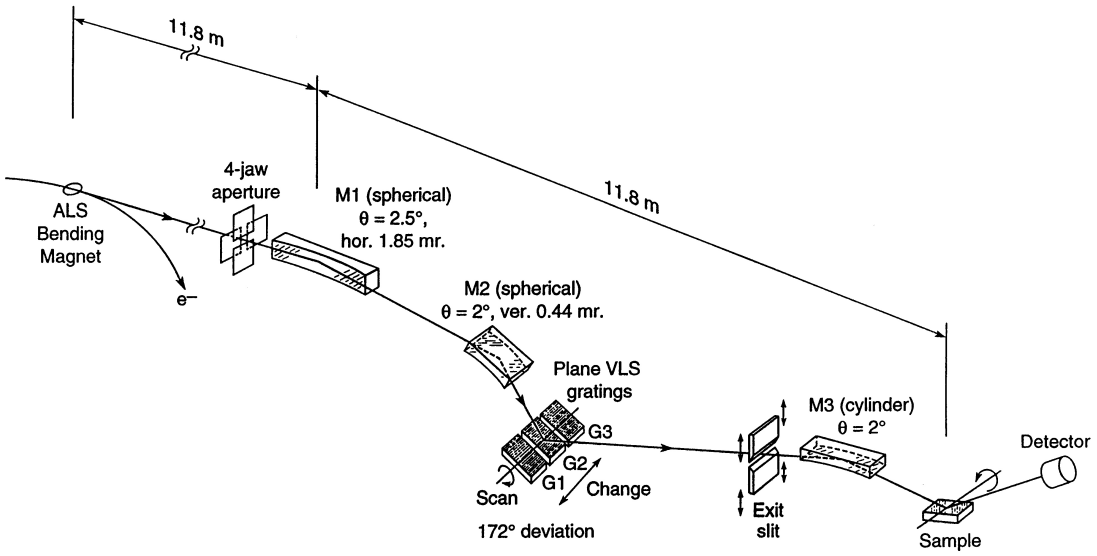

Figure 4.6: Schematic of the Advanced Light Source Calibration and standards beamline 6.3.2 [119].

A beam of 1 mm diameter was focussed on the samples at normal incidence. The spot size increases laterally with increase in the angle of incidence resulting in an increase in the scattering volume. Figure 4.4 shows the experimental set-up which is a symmetric

θ-2θ configuration. In the frame of reference of the sample, the detector and the incident beam are rotated in a circle about a point on the sample surface with a radius equal to the distance between the sample and the detector. The sample stage, along with the detector, is located in a vacuum chamber to avoid scattering and absorption of the soft X-rays in the ambient atmosphere [122, 123].

In the selection of the wavelength a balance needs to be achieved between the available scattering angles for the required range of the scatting vector and the penetration of the X-rays into the sample material. The wide tunable range of X-ray energies available at the 6.3.2 beamline gives the opportunity to select X-rays with the required properties. The penetration depth calculation for silicon at 90° was obtained using the penetration depth calculator software (available at henke.lbl.gov/optical_constants/atten2.html) for X-rays varying wavelength, as shown as a plot in figure 4.7. At 2 nm ($\approx$ 620 eV) the penetration depth of the X-rays is about 0.7 μm and the order of magnitude is similar for X-rays with 13 nm ($\approx$ 95 eV) wavelength. Thus for each sample, 2 nm and 13 nm X-rays were used at angular ranges of $5° \leq \theta \leq 51°$and $5° \leq \theta \leq 45°$ respectively, to investigate the surface properties. Using both wavelengths together yielded a combine scattering range of 0.00842 Å$^{-1} \leq q \leq$ 0.4883 Å^{-1}, which covers a Bragg-like size range of 1 nm $< d <$75 nm. The extension in the size that can be probed is achieved by selecting wavelengths of different energies but similar penetration depth, so as to probe similar areas in the sample. To ensure the equivalence of the measurement when using different wavelengths to obtain overlapping q values, the penetration depth should not be significantly different. Choice of wavelengths that vary significantly in penetration depth could result in loss of information due to discontinuity in the data, or may not even extend the q range, but this could be investigated in future works.

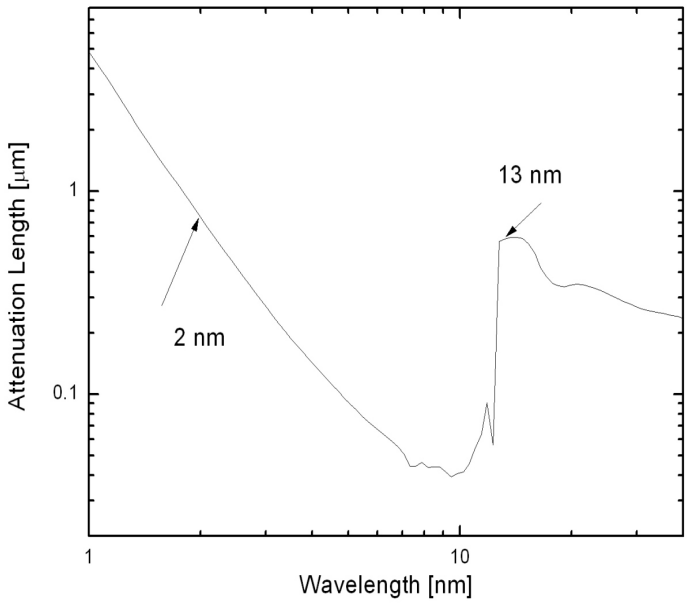

Figure 4.7: X-ray attenuation length for silicon calculated for an incident X-ray beam at 90° to the surface for wavelengths from 1 nm to 40 nm,

(b) **Sample preparation**

Printed silicon nanoparticle samples used in this experiment were produced from inks containing particles from 5 hour HEM of P-type Si wafers and 3 hour HEM M-Si [16]. These will be referred to as HEM-P for the wafer and HEM-M for the 2503 grade feedstock respectively. Printed samples made from nominally intrinsic silicon nanopowder (denoted as I-Si) produced by laser synthesis obtained from MTI Corporation, Richmond, CA, USA was also investigated for comparison. For each type of powder, water-based and solvent-based inks were produced with 80%, 50%, and 20% particle to binder weight ratio, and blade coated onto a paper substrate. For the scattering experiment, the printed layers were cut into strips of 5×0.5 cm and glued onto $4''$ silicon wafers to avoid any additional bending of the samples, before mounting onto the goniometer in the vacuum chamber of the beamline. One strip of the paper was also measured as a reference.

4.4 Electrical Characterisation

A Keithley 4200 semiconductor characterisation system (SCS) was used to determine the I-V characteristics of printed layers composed of 1.5 hour HEM M-Si nanoparticles which were previously studied with synchrotron USAXS as described in section 4.3.2(d). The Keithley 4200-SCS shown in figure 4.8 is an industrial standard equipment which is used for electrical characterisation of electronic devices such as transistors. It is equipped with an embedded computer with windows operating system. The instrument has two Source Measurement Units (SMUs) which can source current and voltage with a supply-measurement range of 0.1 fA to 1 A for the current and 1 μV to 210 V for the voltage. The software of the Keithley 4200-SCS provides the ability to perform real time current-voltage sweeps.

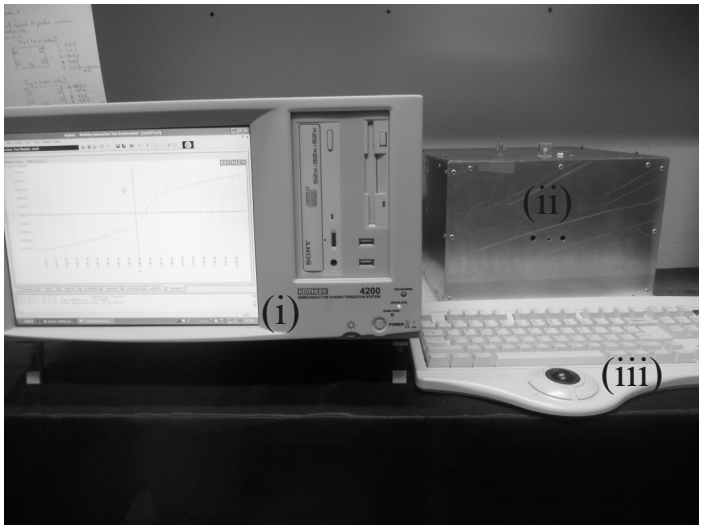

Figure 4.8: Electrical characterisation equipment consisting of (i) the Keithley 4200 semiconductor system, (ii) a Faraday cage, and (iii) the keyboard.

The SMUs are connected to a double Faraday cage shown in figure 4.9, so as to screen out external signals when characterising the samples. The interior of the box is shown in figure 4.9 with the remote sense ground unit (GND), SMU 1 and SMU 2 probes which were extended from the Keithley 4200-SCS. Each probe is shielded with the ends attached to pogo pins to provide the contacts to the sample.

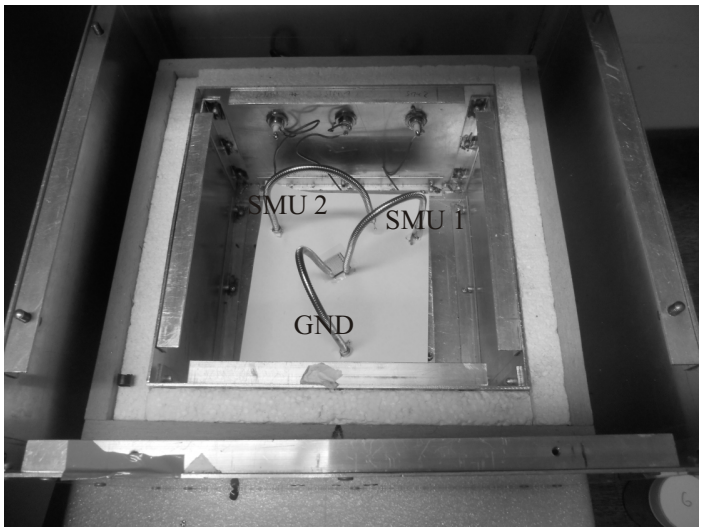

Figure 4.9: Faraday cage with probes that are connected to the GND, SMU 1 and SMU 2 of the Keithley 4200-SCS.

To ensure good contacts with the SMU probes, interdigitated metallic electrodes as shown in figure 4.10 were screen printed onto five silicon layers printed from each of the 80%, 70%, 60% and 50% particle concentration ink, using a pattern similar to that used in the production of printed temperature sensors [124].

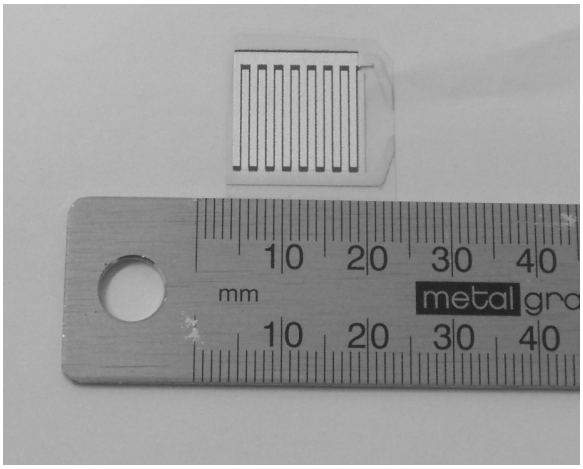

Figure 4.10: Example of a sample prepared for electrical characterisation with a screen printed metallic electrode on top of the printed silicon layer.

For the contacts, Dupont Luxprint 5000 conductor supplied by Dupont Microcircuit Ma-

terials was used. Before the electrical measurement could be performed, the samples were heat-treated at 100° for 5 minutes, so that the solvent could evaporate. Afterwards, the samples were left to cool to room temperature at ambient conditions. To perform the electrical measurements, the samples were placed in the Faraday cage with the metallic contacts connected to SMU 1 and GND as shown in figure 4.9. The Keithley 4200-SCS was set to measure the I-V characteristics in current sweep mode so as to be able to measure the capacitive properties of the layers. A hold time of 2 second was set to allow the device to stabilise before measurement, and a delay time of also 2 seconds was set to reduce undesirable transient responses during the measurement.

5. Results and Analysis

In this chapter, results from microscopy are presented for the nanoparticles and networks investigated. These results are then correlated with results from scattering experiments. Also, the results of electrical measurement on printed layers of the nanoparticles investigated were presented and are compared with results from scattering with the view of establishing a correlation between them.

5.1 Electron microscopy

Figure 5.1a is a TEM micrograph of metallurgical Si nanoparticles milled for 5 hours. From the different grey scale images of the of the individual structures, it can be concluded that the nanoparticles form aggregates of different sizes, even in the dry powder or during the TEM preparation process. Thus, even when the silicon particles are used in an ink to print devices, it is expected that the layers will be characterised by these varying size aggregates as will be confirmed by SEM investigation below. A close up image (figure 5.1b) of the highlighted region seen in the micrograph of figure 5.1a, reveals that the individual nanoparticles really form aggregates and that the larger features may not be single large particles. It is difficult to clearly distinguish individual particles within the larger aggregates due to the compact nature of the aggregates, but this may be improved by using an instrument with higher magnification. Nevertheless, from these images it is obvious that the nanoparticles are not spherical but their shape can generally be described as prolate ellipsoidal. The smaller particles tend to have a lower aspect ratio compared to the larger particles which could probably be aggregates of smaller particles.

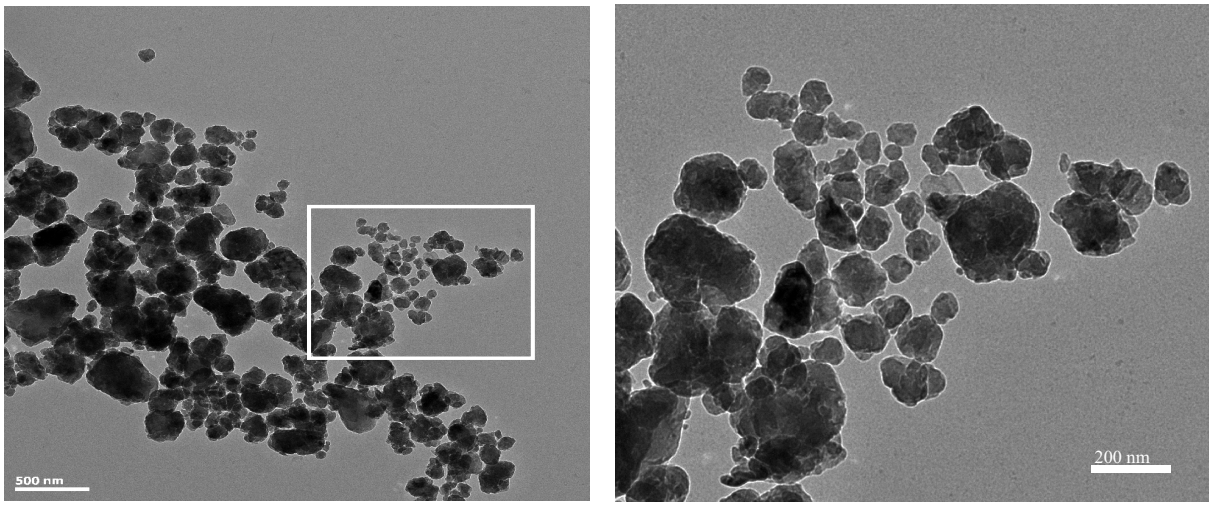

(a) (b)

Figure 5.1: TEM micrographs of (a) 5 hours milled metallurgical grade silicon, (b) a close up image of nanoparticles found in the region indicated by the rectangle in 5.1a.

Figure 5.2 shows the long (figure 5.2a) and short (figure 5.2b) axis size distributions of the HEM M-Si nanoparticles, which confirm that the nanoparticles in the above image were slightly prolate. The histograms of the size distributions were fitted with a log-normal distribution, yielding mean sizes of 130 ± 3 nm and 80 ± 2 nm for the long and short axes respectively. Figure 5.2c shows a histogram of the aspect ratio determined from the ratio of the long to short axes values. A log-normal fit to the histogram yielded a value of 1.30 ± 0.02 for the aspect ratio of the prolate HEM nanoparticles.

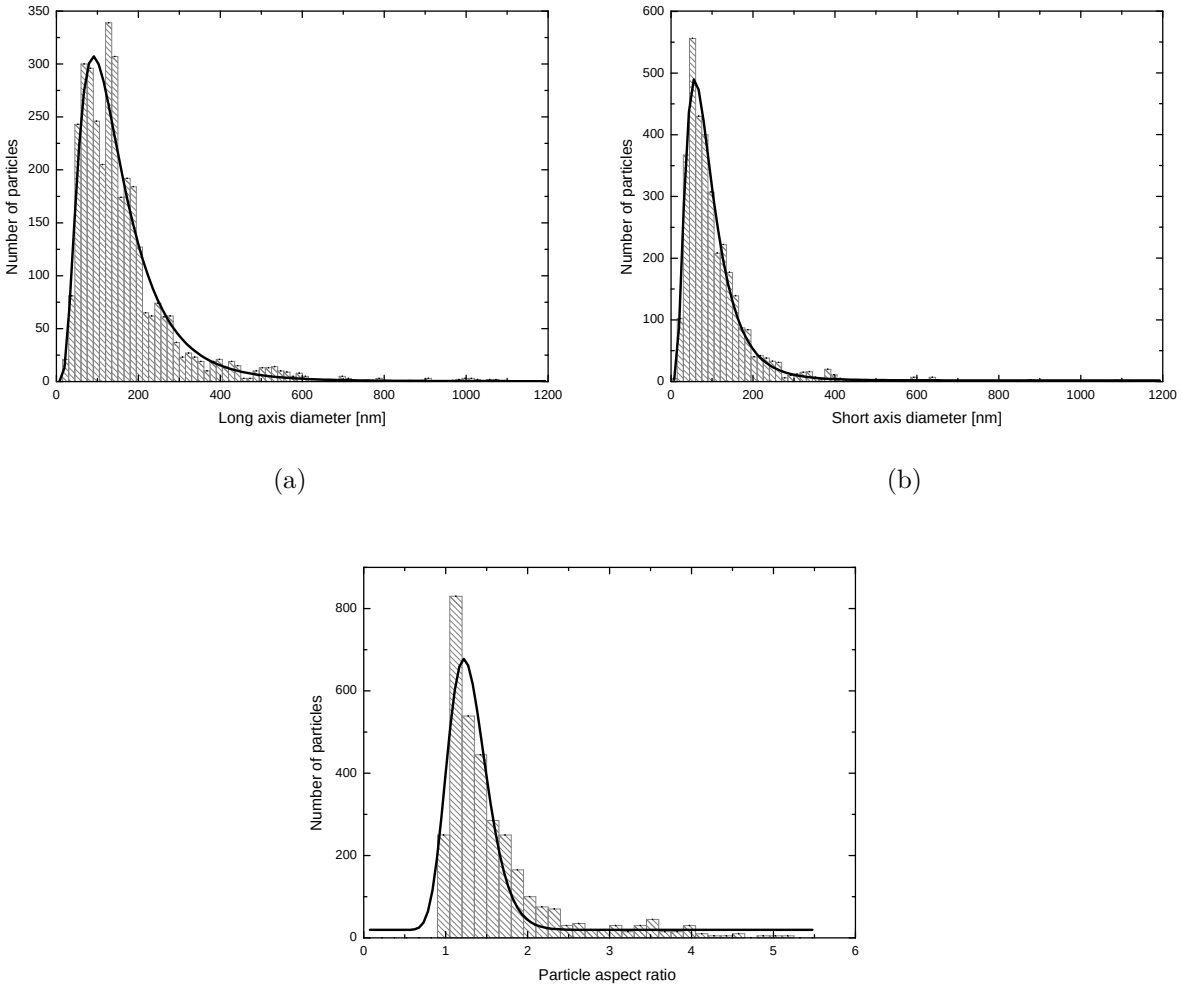

Figure 5.2: Particle size distribution of (a) long and (b) short axes of 5 hour milled silicon, and(c) the aspect ratio of the long to short axes. The *solid line* is a log-normal fit to the data.

Typical examples of SEM micrographs of printed layers prepared from 5 hours milled M-Si and Si nanoparticles produced by TCP using different binders as described in section 4.3.2(a), are shown in figure 5.3 for samples with 80% to 20% particle binder weight ratio. The micrographs in figures 5.3a and 5.3b are of the HEM M-Si nanoparticle based inks deposited on non-porous PET and on paper (porous) substrates respectively. The layer of HEM nanoparticles on the non-porous substrate (figure 5.3a) which was produced using the water-based ink, has a relatively open structure of particle aggregates, where the aggregates have similar features to the powder discussed above. In this open network, continuous paths of contacting particles can be identified which connect particles from one end to the other

end in the field of view. On the other hand, the layer of HEM particles produced using the solvent-based ink, which was blade coated on the porous paper appears to be more dense with no large gaps between the nanoparticle aggregates (figure 5.3b), resulting in more connecting paths through the network. However, the CAB binder can be clearly observed in the left of figure 5.3b, which is not the case for the acrylic binder in figure 5.3a. In some regions, the CAB can be seen to to cover some of the particles. Nevertheless, in both cases, the particles form compact aggregates, which indicates that the ink making and deposition processes do not principally affect the physical arrangement that the nanoparticles had in the dry powder.

Figures 5.3c and 5.3d are the micrographs of layers of Si nanoparticles synthesised by TCP in water-based acrylic and solvent-based CAB inks respectively. Both inks were blade coated on non-porous PET substrates. With a mean size of 22 nm previously reported for the TCP synthesised nanoparticles [45], the nanoparticles are smaller and appear to be more regular in shape than the milled nanoparticles. The layer of TCP synthesised particles with the acrylic binder (figure 5.3c) appear to form a compact network of particle aggregates with many continuous paths of interconnecting clusters easily identifiable throughout the image. On the other hand, the layer of TCP particles printed using CAB as a binder shown in figure 5.3d, forms a more open network of interconnecting particles than seen in figure 5.3c. Regions of unincorporated CAB binder similar to what was observed in figure 5.3b, which partially covers particles in some regions can be seen on most part of the surface.

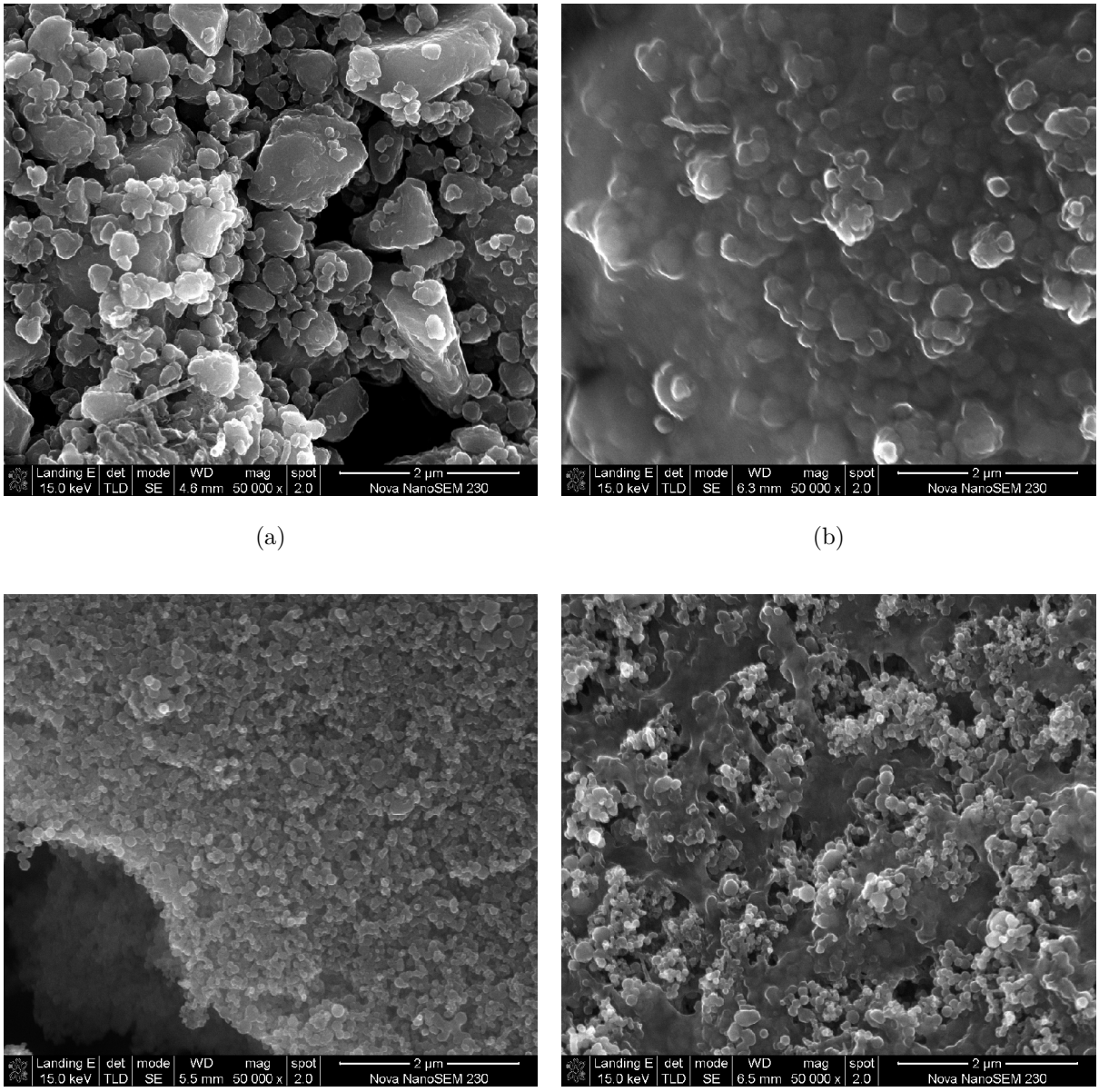

Figure 5.3: Secondary electron scanning electron micrographs of printed silicon nanoparticle layers: (a) milled silicon nanoparticles in acrylic binder printed on PET; (b) milled silicon nanoparticles in CAB printed on paper; (c) silicon nanoparticles produced by TCP in acrylic binder printed on PET; and (d) silicon nanoparticles produced by TCP in CAB printed on PET.

Figure 5.4a shows a cross-sectional scanning electron micrograph of 5 hours milled P-Si nanoparticles blade coated on paper as described in section 4.3.3(b) for the WALq experiment from a water-based acrylic ink mixed in a powder to binder weight ratio of 80% to 20%. The

paper substrate and the printed layer are marked in the figure with the boundary between them indicated by the solid black line added to the image. Though the perspective in the image is slightly tilted, the thickness of the nanoparticle layer is clearly about 4 times less than the thickness of the paper substrate. A close up view of a section of the printed layer indicated by the rectangle in figure 5.4a is shown in figure 5.4b. The top right of the image shows a smoothed region of the cross-section of the layer which may have resulted from the SEM preparation. Because of the tilt in the image, the surface of the printed layer is clearly visible and can be seen to be composed of varying sizes of the nanoparticle aggregates forming rough features of the order of several microns.

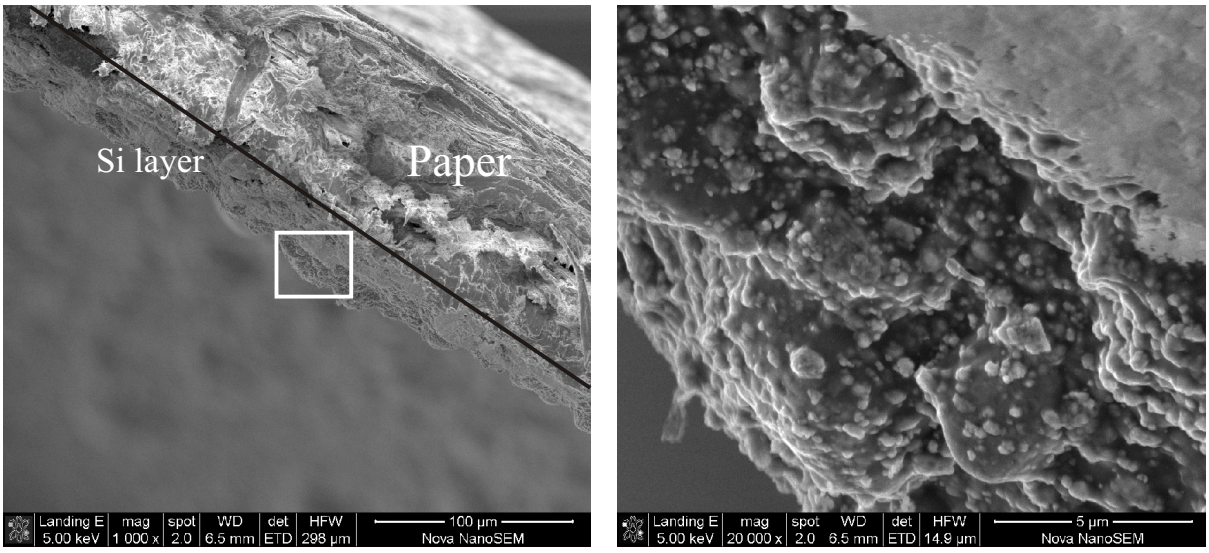

(a) (b)

Figure 5.4: Cross-sectional scanning electron microscope of (a) HEM-P-Si nanoparticle layers deposited on paper, and (b) a higher magnification view of a section of the surface of the layer with rough features of the order of several microns.

5.2 Scattering Experiments

5.2.1 Quantitative evaluation of structural parameters

Figure 5.5 is a log-log plot of the combined SAXS (*star*) and USAXS (*circle*) data of the 5 hour milled metallurgical silicon blade coated on PET using an acrylic binder mixed at 80% to 20% weight ratio, and as described in section 4.3.1. The experiment was used to

demonstrate the extraction of quantitative information in aggregates from scattering data [71]. The combined q-range of this measurement yielded an intensity variation of over 10 orders of magnitude as seen in the figure.

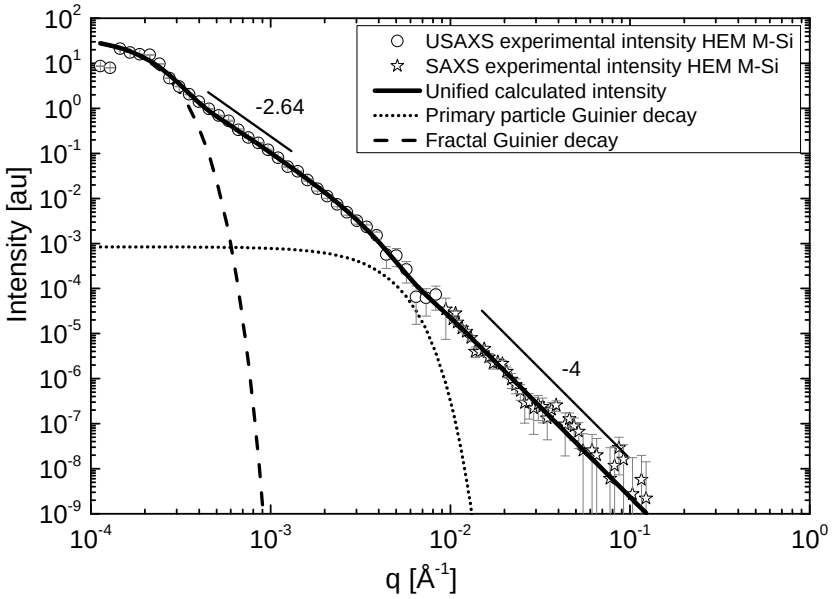

Figure 5.5: Corrected SAXS/USAXS data for HEM M-Si nanoparticles fitted with the unified equation (solid line). The Guinier exponential decay for the primary and fractal structural levels are shown in dash lines. [71]

A fit to the combined data indicated by the *solid line* in figure 5.5 was achieved with two structural levels of the unified function given in equation 3.19. The primary particle Guinier decay and fractal aggregate Guinier decay, from which the average sizes of the primary particles and aggregates respectively can be determined, are shown by dashed lines in the figure. Two power law regions highlighted by the straight lines above the data in the log-log plot, were determined from the fit. These are a Porod scattering i.e $I = q^{-4}$ at high q associated with the primary particles and the power -2.64 at low q associated with the mass fractal aggregate. A summary of the fit results obtained from the unified function are shown in table 5.1. For all the scattering experiments, the uncertainties are propagated from the statistical uncertainty in the data.

The primary particles have an average radius of gyration, $R_{g,1}$ of 49 ± 1 nm bounded by smooth and sharp interfaces as evident by the first level power law exponent α_1 of -4. Also, the contrast and exponential decay in intensity of the primary particles is given by the

Table 5.1: Fitting parameters using two structural levels of the unified function applied to the combined SAXS and USAXS data.

Fitting parameters	Level 1	Level 2
fractal dimension, d_f	-	2.64 ± 0.03
Radius of gyration, R_g	490 ± 10 Å	9390 ± 40 Å
Power law prefactor, B	$2.4 \pm 0.1 \times 10^{-13}$	$1.3 \pm 0.1 \times 10^{-9}$
Guinier prefactor, G	$8.4 \pm 0.4 \times 10^{-4}$	40.1 ± 0.3

Guinier law prefactor G_1 as $8.4 \pm 0.4 \times 10^{-4}$, and the associated power law prefactor B_1 was obtained as $2.4 \pm 0.1 \times 10^{-13}$. The aggregates formed by the nanoparticles have an average radius of gyration $R_{g,2}$ which is 0.939 ± 0.004 μm, and a mass fractal dimension of 2.64. An exponential decay G_2 of 40.1 ± 0.3 and B_2 of $1.3 \pm 0.1 \times 10^{-9}$ which are 5 and 4 orders of magnitude more than for scattering associated with primary particles, were obtained for the mass fractal aggregates. Using these results obtained from the fits (table 5.1), the scaling parameters were calculated as discussed in section 3.2. A summary of the calculated results is shown in table 5.2.

Table 5.2: Calculated scaling parameters as defined in section 3.3, for aggregates of milled nanoparticles.

Calculated scaling parameters	Magnitudes
Degree of aggregation, z	47600 ± 300
Sauter mean diameter, d_p (nm)	42.9 ± 07
Geometric standard deviation, σ_g	1.54
Minimum dimension, d_{min}	1.14 ± 0.04
Connectivity dimension, c	2.32 ± 0.02
Branch fraction, ϕ_{br}	0.998 ± 0.007
Number of branch points in aggregate, n_{br}	6710 ± 70
Number of branch points in minimum path, $n_{br,p}$	28 ± 1
Number of primary particles per branch, z_{br}	1700 ± 30
Average number of particles per segment, z_s	3.6 ± 0.4
Average coordination number, C_N	2.14 ± 0.05

It was found that about 47600 primary particles, with Sauter mean diameter d_p of 43 nm

form an aggregate. A value of 1.54 was obtained as the geometric standard deviation σ_g for the particle size distribution. The average minimum path that traverses the aggregates was found to have a dimension d_{min} of 1.14, and the connectivity paths attached to the minimum path was found to have a high dimension c of 2.32. The fraction of particles not included in the minimum path ϕ_{br}, was found to be 0.998. A total of about 6710 branches n_{br} was found in the aggregates with an average of 28 branch sites per minimum path and each branch having about 1700 primary particles. Furthermore, the aggregates were found to have about 4 particles in each branch segment z_s with each particle having an average coordination number C_N of 2.14.

5.2.2 Influence of particle production approach, ink formulation and substrate on the aggregation of silicon nanoparticles.

HEM and TCP Si nanoparticles based layers blade coated on paper and PET substrates as described in section 4.3.2(a), were investigated using synchrotron USAXS to study the the influence of particle production, ink formulation, as well as the porosity of the substrate on the aggregation of nanoparticles [70]. Table 5.3 identifies the different material combinations for each sample. The acrylic water-based and CAB solvent based inks prepared were composed of the TCP particles and the 5 hour HEM metallurgical particles mixed at 80% to 20% particle by weight.

Table 5.3: Specifications of the blade coated silicon nanoparticle samples with respect to the ink systems and substrates used for synchrotron USAXS measurements following investigations in 4.3.2(a).

Sample ID	Si nanoparticles	Binder	Substrate
HEM1	high energy milled	Acrylic	Paper
HEM2	high energy milled	Acrylic	PET
HEM3	high energy milled	CAB	Paper
HEM4	high energy milled	CAB	PET
TCP1	synthesized by TCP	Acrylic	Paper
TCP2	synthesized by TCP	Acrylic	PET
TCP3	synthesized by TCP	CAB	Paper
TCP4	synthesized by TCP	CAB	PET

Figure 5.6 shows log-log plots of the background corrected and desmeared USAXS data from the eight samples. The intensities have been scaled by different factors for ease of comparison. The scattering data from the HEM M-Si nanoparticle layers (figure 5.6a) covers a q-range yielding intensity range of about 10 orders of magnitude, similar to that obtained from the combined data of the laboratory based scattering experiments reported in section 4.3.1 and shown in figure 5.5. The scattering profiles of the layers formed from TCP synthesised Si nanoparticles, shown in figure 5.6b, have less steep slopes at low q (0.0005 Å$^{-1} \leq q \leq 0.004$ Å^{-1}) when compared with a similar region in the HEM M-Si data. Samples HEM1, TCP1 and TCP3 which were printed on paper substrates, did not yield scattering intensities significantly above that from the reference samples below q of approximately 0.0004 Å^{-1}. For all eight samples, there is a drop in intensity at $q \approx 0.0058$ Å^{-1}. This drop in intensity is an artefact arising from the instrument and was also observed in the reference sample. At very high q (above 0.1 Å^{-1}), only a constant background could be measured for all the samples.

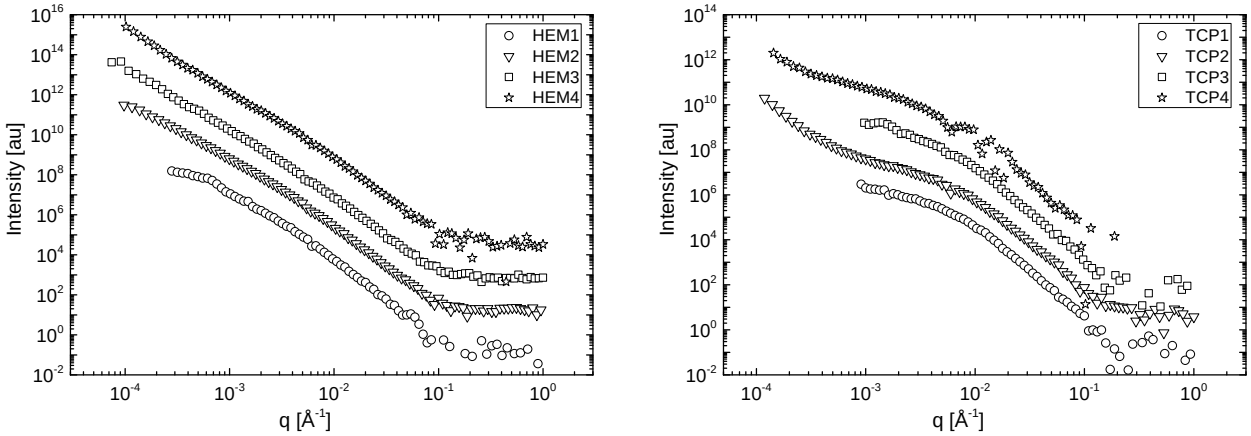

(a) (b)

Figure 5.6: Synchrotron USAXS spectra obtained from layers of different inks of (a) 5 hour HEM M-Si, and (b) TCP Si nanoparticles printed on paper and PET, shown on a log-log scale. The intensities have been scaled by different factors for ease of comparison.

Figures 5.7a and 5.7b are the fits of the unified function (*solid line*) to the USAXS data of samples HEM1 and TCP1 shown here as examples. Two structural levels of the unified function were sufficient to fit most of the samples, except for the layers containing nanoparticles, synthesised by TCP printed on PET substrate, for which a third structural level was required. For comparison and also because the third level Guinier fit was not achieved

for the other samples, only the two levels common to most of the samples will be presented. The primary particle Guinier decay, as well as the fractal aggregate Guinier decay are shown as dashed lines in the figure. The power law regions, as determined from the unified function, are highlighted by straight lines labelled with their respective slopes above the USAXS data. Summaries of the fit results obtained from the unified function are shown in tables 5.4 and 5.5.

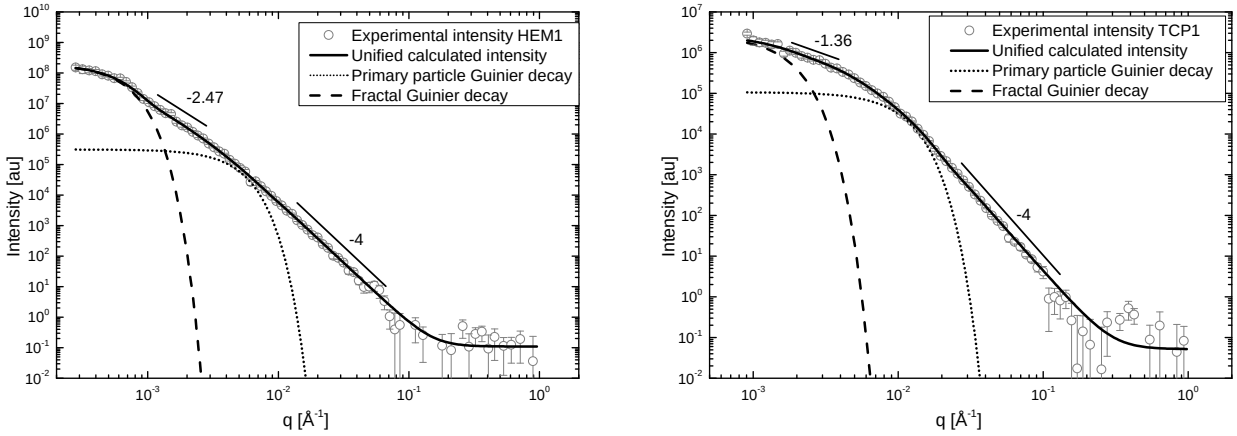

(a) (b)

Figure 5.7: Synchrotron USAXS spectra obtained from (a) HEM M-Si, and (b) TCP Si nanoparticle layers printed using acrylic binder based inks on paper substrates. The *solid line* represent the unified fit to the data. The power law regions for two structural levels as well as the Guinier decays are indicated on the plots as described in the text.

Generally, it was observed that all the nanoparticle layers irrespective of how they were produced, ink formulation, and substrate used, display Porod scattering at high q for the primary particle structural level. From the results given in table 5.4, the first structural level radii of gyration $R_{g,1}$ differs with the nature of the substrate. The samples printed on paper, HEM1 and HEM3, have $R_{g,1}$ of 44 ± 7 nm and 42 ± 3 nm respectively, which are smaller than 64 ± 2 and 52 ± 1 for HEM2 and HEM3 respectively, which were printed on PET. No specific trends was observed in the exponential decay in intensity and power law prefactors of the HEM primary particles given by G_1 and B_1 respectively. At the second structural level, values ranging from 2.65 to 2.95 were obtained for the power law dependence α_2, indicating that all the HEM M-Si aggregates display roughly similar mass fractal properties. For the aggregate size related to the second radius of gyration $R_{g,2}$, a similar dependence on substrate as $R_{g,1}$ was observed. In addition, the layers produced with the acrylic, HEM1 and HEM2

with $R_{g,2}$ of 315 ± 7 nm and 1035 ± 20 nm respectively, have lower values in comparison to HEM3 and HEM4 from the solvent-based ink with 1450 ± 30 nm and 1680 ± 10 nm respectively. Similar to the first level, no specific trends were observed for G_2 and B_1.

Table 5.4: Fitting parameters using two structural levels of the unified function applied to the synchrotron USAXS data of HEM M-Si particles. Parameters with subscript 1 refer to primary particles and those with subscript 2 refer to aggregates.

Sample	Level 1			Level 2			
	G_1	B_1	$R_{g,1}$(Å)	G_2	B_2	$R_{g,2}$(Å)	α_2
HEM1	$3.1 \pm 1.0 \times 10^5$	$6.10 \pm 0.01 \times 10^{-5}$	440 ± 70	$1.80 \pm 0.001 \times 10^8$	0.44 ± 70	3150 ± 70	2.65 ± 0.10
HEM2	$2.2 \pm 0.2 \times 10^6$	$1.30 \pm 0.01 \times 10^{-4}$	640 ± 20	$1.5 \pm 0.1 \times 10^{10}$	0.31 ± 0.01	10350 ± 200	2.92 ± 0.01
HEM3	$5.5 \pm 0.9 \times 10^5$	$1.60 \pm 0.01 \times 10^{-4}$	420 ± 30	$6.8 \pm 0.4 \times 10^{10}$	0.14 ± 0.01	14500 ± 300	2.81 ± 0.01
HEM4	$4.4 \pm 0.2 \times 10^5$	$7.60 \pm 0.04 \times 10^{-5}$	520 ± 10	$5.7 \pm 0.1 \times 10^{10}$	0.020 ± 0.001	16800 ± 100	2.95 ± 0.01

From the results in table 5.5 for the TCP Si nanoparticles, the average primary particle size obtained does not completely follow the same dependence on the substrate as observed for the HEM M-Si particle layers. Whereas TCP1 and TCP2 produced with water-based acrylic binder having $R_{g,1}$ of 20 ± 1 nm and 34 ± 0.4 nm respectively, show a difference between the substrates; TCP3 and TCP4 from the solvent-based ink having 23 ± 0.5 nm and 24 ± 1 are similar within the limits of the uncertainty. In the second structural level, a dependence on the substrate is observed for $R_{g,2}$, with TCP1 and TCP3 samples on paper having similar value of 120 nm which is less than the 300 nm obtained for TCP2 and TCP4 samples on PET. The aggregates also displayed mass fractal scattering, with a range of 1.36 to 1.86 obtained for α_2 which is less than the values obtained for the HEM M-Si layers. Similar to the HEM M-Si particle layers, there was no observable trend in the values obtained for G_1, G_2, B_1 and B_2.

Table 5.5: Fitting parameters using two structural levels of the unified function applied to the synchrotron USAXS data of TCP Si particles. Parameters with subscript 1 refer to primary particles and those with subscript 2 refer to aggregates.

Sample	Level 1			Level 2			
	G_1	B_1	$R_{g,1}$(Å)	G_2	B_2	$R_{g,2}$(Å)	α_2
TCP1	$1.1 \pm 0.1 \times 10^5$	$4.30 \pm 0.01 \times 10^{-4}$	200 ± 10	$2.6 \pm 0.3 \times 10^6$	246 ± 4	1200 ± 100	1.36 ± 0.10
TCP2	$3.2 \pm 0.1 \times 10^5$	$3.60 \pm 0.01 \times 10^{-4}$	340 ± 4	$7.0 \pm 0.2 \times 10^6$	34.7 ± 8.0	3000 ± 70	1.56 ± 0.03
TCP3	$1.0 \pm 0.6 \times 10^5$	$3.3 \pm 0.1 \times 10^{-4}$	230 ± 5	$6.1 \pm 0.4 \times 10^6$	12.94 ± 2.60	1200 ± 50	1.86 ± 0.03
TCP4	$1.7 \pm 0.01 \times 10^4$	$2.80 \pm 0.01 \times 10^{-5}$	240 ± 10	$1.5 \pm 0.01 \times 10^6$	10.57 ± 2.3	3000 ± 100	1.52 ± 0.03

To compare the topological features of the HEM M-Si and TCP synthesised Si nanoparticle aggregates, the scaling parameters discussed in section 3.2 were calculated from the unified fit parameters in tables 5.4 and 5.5 [70]. These results are shown in tables 5.6 and 5.7. For the HEM M-Si particles, it was found that the layers from the water-based ink have about 600 and 7000 primary particles in an average aggregate when deposited on paper and PET respectively. These values are considerably smaller than for the layers produced with the solvent-based ink which have about 120000 and 130000 primary particles in an average aggregate on paper and PET respectively. The average Sauter mean diameter d_p of the primary particles was found to be 41 nm, with an average value of 1.47 obtained as the geometric standard deviation σ_g for the particle size distribution. The dimension of the average minimum path of primary particles spanning the aggregates was found to range between 1.1 and 1.2, while the dimension of the connectivity paths of particles attached to the minimum path was found to range between 2.1 and 2.5. Generally, a high value of about 0.99 was found for the fraction of particles in the aggregates not included in the minimum path.

Table 5.6: Calculated scaling parameters for aggregates of HEM M-Si nanoparticles in printed layer as defined in section 3.3.

	Magnitudes			
	Water-based ink		Solvent-based ink	
	HEM1	HEM2	HEM3	HEM4
z	600 ± 200	7000 ± 600	120000 ± 20000	130000 ± 6000
d_p (nm)	43 ± 2	47 ± 2	35 ± 2	40 ± 2
σ_g	1.43	1.47	1.46	1.51
d_{min}	1.2 ± 0.1	1.1 ± 0.1	1.1 ± 0.1	1.2 ± 0.1
c	2.1 ± 0.8	2.2 ± 0.2	2.4 ± 0.3	2.5 ± 0.3
ϕ_{br}	0.95 ± 0.03	0.99 ± 0.01	0.99 ± 0.01	0.99 ± 0.01
n_{br}	70 ± 5	900 ± 10	15700 ± 50	16100 ± 45
$n_{br,p}$	4 ± 0.5	13 ± 0.5	30 ± 0.5	24 ± 0.3
z_{br}	139 ± 10	600 ± 60	4213 ± 74	5400 ± 70
z_s	4.1 ± 0.2	3.9 ± 0.3	3.9 ± 0.2	4.0 ± 0.1
C_N	2.1 ± 0.2	2.1 ± 0.2	2.1 ± 0.2	2.1 ± 0.2

The number of branches found in the aggregates varies similar to the number of primary

particles in the aggregates. HEM1 with about 70 branches and HEM2 with about 900 branches have about 4 and 13 branch sites $n_{br,p}$ per minimum path.An increased number of branch sites of 30 and 24 were found for HEM3 with 15700 branches and HEM4 with 16100 branches respectively. The average number of primary particles in the branches were found for HEM1, HEM2, HEM3 and HEM4 to be 139, 600, 4213 and 5400 respectively, with an average of 4 particles in each branch segment. It was found that the particles in the aggregate have an average coordination number C_N of 2.1.

Unlike the HEM M-Si layers, table 5.7 shows that the TCP synthesised Si nanoparticle layers, are composed of aggregates with smaller number of primary particles. TCP1, TCP2, TCP3 and TCP4 were found to have about 24, 22, 60 and 84 primary particles respectively in an aggregate. An average value of 25 nm was obtained for the Sauter mean diameter of the primary particles, with an average geometric standard deviation of 1.43. Similar to the HEM M-Si layers, the minimum paths of particles spanning an aggregate of the TCP particle layers were found to have a dimension of about 1.1. The TCP layers were found to have fewer connecting paths than the HEM M-Si layers as indicated by the connectivity dimension which ranges from 1.2 to 1.6. Also less, is the fraction of primary particles in the aggregates of the TCP particles not attached to the minimum path, it was found to range between 0.46 and 0.8. Total branches of about 7, 8 16 and 19 were obtained for TCP1, TCP2, TCP3 and TCP4 respectively, indicating more branches present in the aggregates of the solvent-based ink as obtained for the HEM M-Si particle layers. The four TCP Si layers were found to have about 7, 5, 5 and 11 branch sites per minimum paths, which are composed of about 2, 3, 9 and 5 primary particles respectively. Each branch segment in the TCP aggregates were found to have an average of 2 primary particles with a slightly higher coordination number of 2.3.

Table 5.7: Calculated scaling parameters for aggregates of TCP synthesised Si nanoparticles in printed layers as defined in section 3.3.

	Magnitudes			
	Water-based ink		Solvent-based ink	
	TCP1	TCP2	TCP3	TCP4
z	24 ± 4	22 ± 1	60 ± 5	84 ± 8
d_p (nm)	19 ± 1	30 ± 1	23 ± 1	30 ± 1
σ_g	1.37	1.53	1.45	1.38
d_{min}	1.1 ± 0.2	1.1 ± 0.4	1.1 ± 0.2	1.1 ± 0.3
c	1.2 ± 0.2	1.5 ± 0.5	1.6 ± 0.3	1.4 ± 0.3
ϕ_{br}	0.46 ± 0.01	0.64 ± 0.01	0.80 ± 0.03	0.69 ± 0.02
n_{br}	7 ± 0.3	8 ± 0.2	16 ± 0.3	19 ± 0.3
$n_{br,p}$	7 ± 0.7	5 ± 0.2	5 ± 0.2	11 ± 0.6
z_{br}	2 ± 0.3	3 ± 0.2	9 ± 0.8	5 ± 0.6
z_s	1.7 ± 0.3	1.3 ± 0.1	1.8 ± 0.2	2.1 ± 0.2
C_N	2.3 ± 0.4	2.3 ± 0.1	2.3 ± 0.2	2.2 ± 0.2

5.2.3 Influence of particle concentration and substrates on the aggregation of silicon nanoparticles in printed layers.

The effects of changing the concentration of nanoparticles in the inks, as well as the nature of substrate on the aggregates of the particles were investigated using synchrotron USAXS on 5 hour HEM M-Si particles in acrylic water-based inks of 80%, 70%, 60% and 50% particle weight ratios screen printed on paper, aramid paper and PET substrates as described in section 4.3.2(b). Figure 5.8 shows the dependence of the scattering intensities on particle concentration with respect to the three different substrates used. The scattering profiles of the layers printed on paper did not extend to very low q values, unlike the layers printed on aramid paper and PET substrates. This is because at low q, the intensity signal of the reference sample is comparable to the signal from the measured sample as described in section 5.2.2. A peak is observed at $q \approx 0.78$ Å^{-1} which arises from the instrument used and not associated to the samples investigated. At high q, only a constant background could be measured similar to the previous synchrotron USAXS measurement.

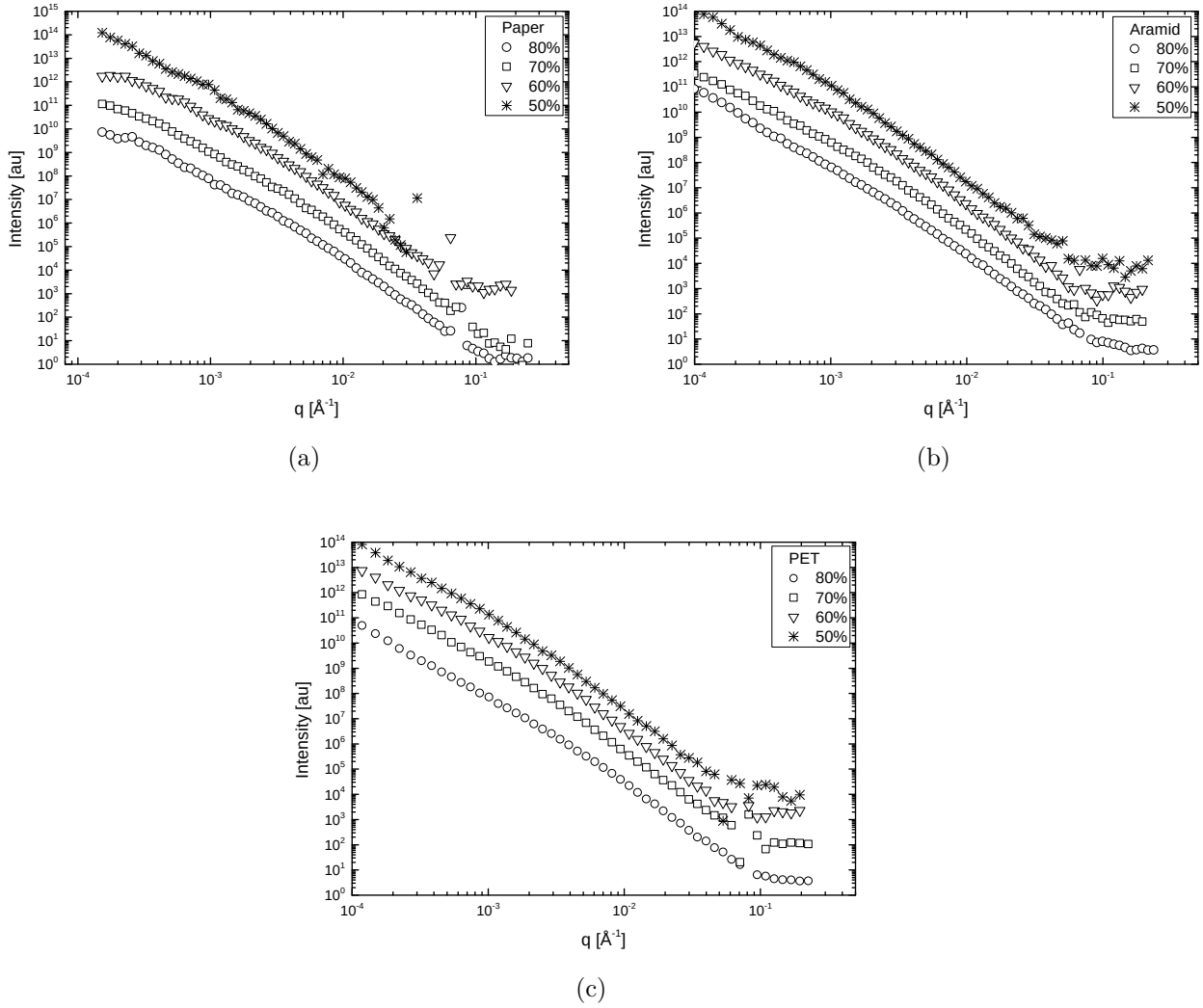

Figure 5.8: USAXS spectra of HEM M-Si on a log- log scale for samples printed on (a) paper,(b) aramid paper, and (c) PET substrates. The intensities have been scaled by different factors for ease of comparison. The numbers in the figures is the percentage by weight concentration of nanoparticles in the water-based inks printed.

All the scattering data were fitted using the unified function. Some of the curves required three structural levels of the unified function but only the first and second structural levels were considered for the reasons given in section 5.2.2. A summary of the fit results obtained from the unified function are shown in tables 5.8 to 5.10. Similar to previously described observations with HEM M-Si samples, all the curves display Porod scattering at high q and mass fractal scattering at low q with values of d_f lying between 2 and 3. From table 5.8, the primary particles in the layers printed using 80%, 70%, 60% and 50% particle concentration

inks printed on paper, have increasing primary radii of gyration $R_{g,1}$ values of about 60 nm, 90 nm, 120 nm and 150 nm respectively. On the contrary, the aggregates all have similar second level radii of gyration $R_{g,2}$ of about 600 nm. The Guinier decay of the second structural level of the layer containing 50% particles by weight could not be achieved in the fit of the data. No specific trend could be identified for the values of G_1, G_2, B_1 and B_2.

Table 5.8: Fitting parameters using two structural levels of the unified function applied to the synchrotron USAXS data of different concentrations of HEM M-Si particle inks printed on paper. Parameters with subscript 1 refer to primary particles and those with subscript 2 refer to aggregates.

Particle weight concentration	Level 1			Level 2			
	G_1	B_1	$R_{g,1}$(Å)	G_2	B_2	$R_{g,2}$(Å)	α_2
80%	$3.9 \pm 1 \times 10^{6}$	$3.2 \pm 0.04 \times 10^{-4}$	600 ± 50	$8.1 \pm 0.5 \times 10^{9}$	0.7 ± 0.5	6000 ± 150	2.7 ± 0.1
70%	$1.5 \pm 0.2 \times 10^{7}$	$3.0 \pm 0.01 \times 10^{-4}$	900 ± 50	$9.5 \pm 0.3 \times 10^{9}$	0.5 ± 0.02	6000 ± 70	2.7 ± 0.2
60%	$2.8 \pm 0.2 \times 10^{7}$	$1.7 \pm 0.02 \times 10^{-4}$	1200 ± 60	$4.2 \pm 0.5 \times 10^{5}$	12.1 ± 0.4	6000 ± 300	2.3 ± 0.4
50%	$3.8 \pm 1 \times 10^{7}$	$6.0 \pm 0.1 \times 10^{-5}$	1500 ± 80		0.8 ± 0.02		2.6 ± 0.1

Table 5.9 shows that the primary particles in the layers printed using 80%, 70%, 60% and 50% particle concentration inks on aramid paper, have increasing $R_{g,1}$ values of about 55 nm, 90 nm, 125 nm and 170 nm respectively, which are similar to what was obtained for the layers on paper. The aggregates have $R_{g,2}$ values ranging from 900 nm to 1300 nm, which is greater than what was obtained for the paper samples. The variation in the $R_{g,2}$ values appears to be random since no trend with respect to concentration could be associated with it.

Table 5.9: Fitting parameters using two structural levels of the unified function applied to the synchrotron USAXS data of different concentrations of HEM M-Si particle inks printed on aramid paper. Parameters with subscript 1 refer to primary particles and those with subscript 2 refer to aggregates.

Particle weight concentration	Level 1			Level 2			
	G_1	B_1	$R_{g,1}$(Å)	G_2	B_2	$R_{g,2}$(Å)	α_2
80%	$1.5 \pm 0.1 \times 10^{6}$	$2.4 \pm 0.02 \times 10^{-4}$	550 ± 30	$8.4 \pm 1 \times 10^{10}$	0.2 ± 0.01	13000 ± 500	2.8 ± 0.1
70%	$7.3 \pm 0.2 \times 10^{6}$	$1.7 \pm 0.01 \times 10^{-4}$	900 ± 50	$2.0 \pm 0.1 \times 10^{10}$	0.3 ± 0.02	10000 ± 300	2.8 ± 0.1
60%	$1.2 \pm 0.1 \times 10^{7}$	$7.7 \pm 0.06 \times 10^{-5}$	1250 ± 50	$9.5 \pm 0.5 \times 10^{9}$	1.4 ± 0.02	9000 ± 200	2.5 ± 0.1
50%	$2.3 \pm 0.2 \times 10^{7}$	$3.2 \pm 0.04 \times 10^{-5}$	1700 ± 60	$2.3 \pm 0.3 \times 10^{10}$	1.0 ± 0.4	13000 ± 550	2.5 ± 0.1

Table 5.10 shows that the primary particles in the layers printed on PET, have values of

$R_{g,1}$ increasing with decreasing particle concentrations of about 55 nm, 90 nm, 125 nm and 170 nm respectively, which is similar to the trend seen for the layers on paper and aramid discussed above. The aggregates have radii of gyration $R_{g,2}$ ranging from 1400 nm to 1800 nm, which is larger than that obtained in the paper and aramid samples. Similarly to previously measured USAXS data, no trend could be associated with the Guinier and power law prefactors.

Table 5.10: Fitting parameters using two structural levels of the unified function applied to the synchrotron USAXS data of different concentrations of HEM M-Si particle inks printed on PET. Parameters with subscript 1 refer to primary particles and those with subscript 2 refer to aggregates.

Particle weight concentration	Level 1			Level 2			
	G_1	B_1	$R_{g,1}$(Å)	G_2	B_2	$R_{g,2}$(Å)	α_2
80%	$3.3 \pm 0.4 \times 10^{6}$	$3.1 \pm 0.02 \times 10^{-4}$	600 ± 30	$7.7 \pm 3 \times 10^{10}$	0.1 ± 0.02	14000 ± 1500	2.9 ± 0.02
70%	$1.3 \pm 0.04 \times 10^{7}$	$1.2 \pm 0.01 \times 10^{-4}$	900 ± 40	$4.7 \pm 0.2 \times 10^{10}$	0.6 ± 0.01	14000 ± 200	2.7 ± 0.2
60%	$1.6 \pm 0.1 \times 10^{7}$	$6.9 \pm 0.04 \times 10^{-5}$	1200 ± 30	$3.8 \pm 0.4 \times 10^{10}$	0.6 ± 0.01	16000 ± 600	2.6 ± 0.1
50%	$1.5 \pm 0.2 \times 10^{7}$	$3.5 \pm 0.03 \times 10^{-5}$	1500 ± 50	$6.5 \pm 0.9 \times 10^{10}$	0.2 ± 0.03	18000 ± 700	2.7 ± 0.02

Figure 5.9 shows graphs comparing the values of $R_{g,1}$ obtained for the different composition of HEM M-Si nanoparticles for each substrate used. The *solid line* on the graphs is a guide to the eye showing the trend of $R_{g,1}$ with respect to the concentration. Within the limits of the experimental uncertainties, a linear decrease in $R_{g,1}$ with increase in concentration, which is similar for all the samples was observed. No dependence on substrate was observed for $R_{g,1}$, since the average values at each concentration did not change across the substrates.

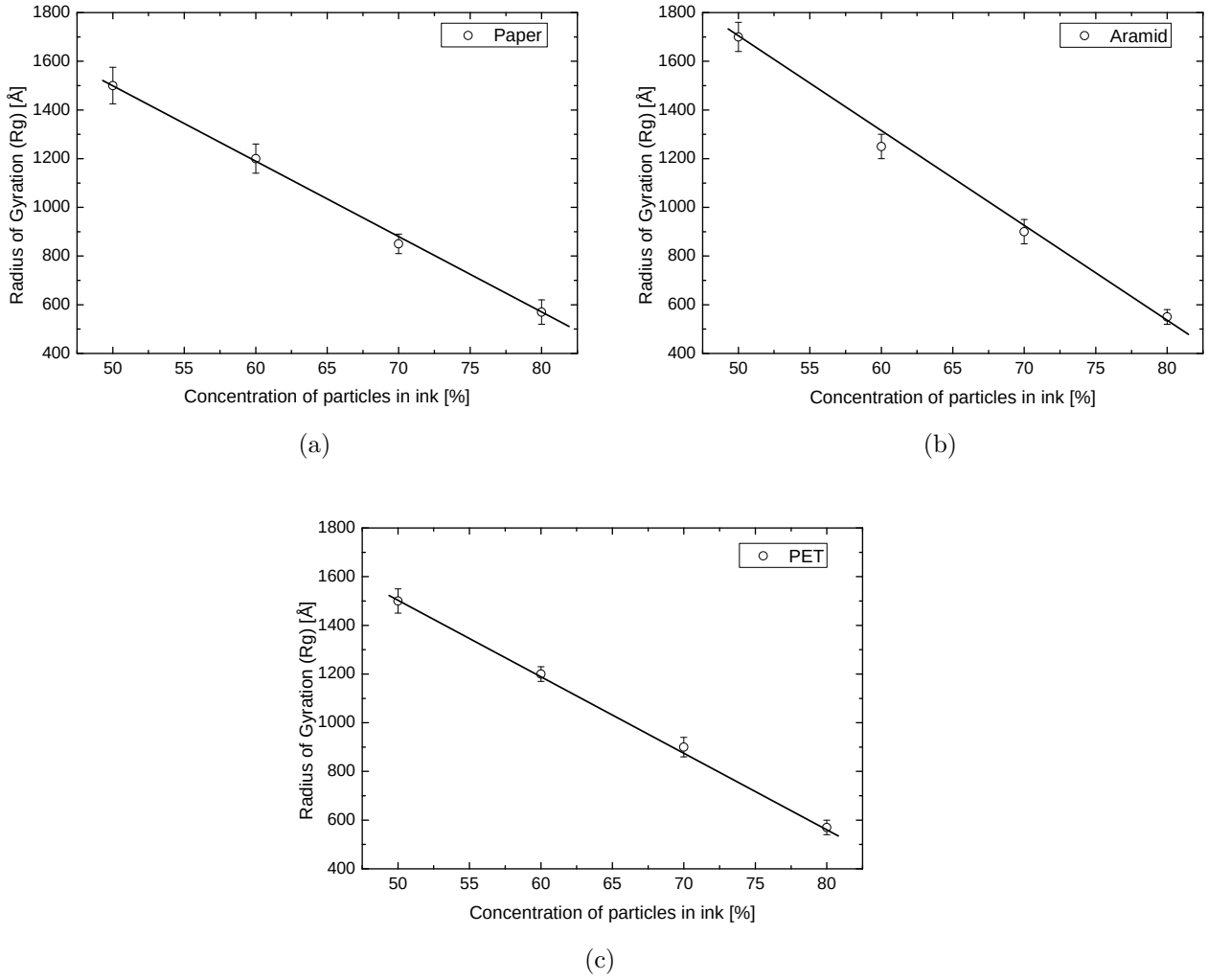

Figure 5.9: First level radii of gyration obtained from the fit of USAXS data for different composition of HEM M-Si nanoparticle inks printed on (a) paper,(b) aramid paper, and (c) PET substrates.

Figure 5.10 is a representation of $R_{g,2}$ obtained for all the samples printed on the various substrates. Generally, the values of $R_{g,2}$ obtained for the samples on the more porous paper substrate are smaller than the $R_{g,2}$ values obtained for the other substrates. The samples on non-porous PET substrate have the highest values, while the less-porous aramid substrate samples have intermediate $R_{g,2}$ values. The aggregate structure shows a dependence on the nature of the substrate, similar to what was noted previously in section 5.2.2.

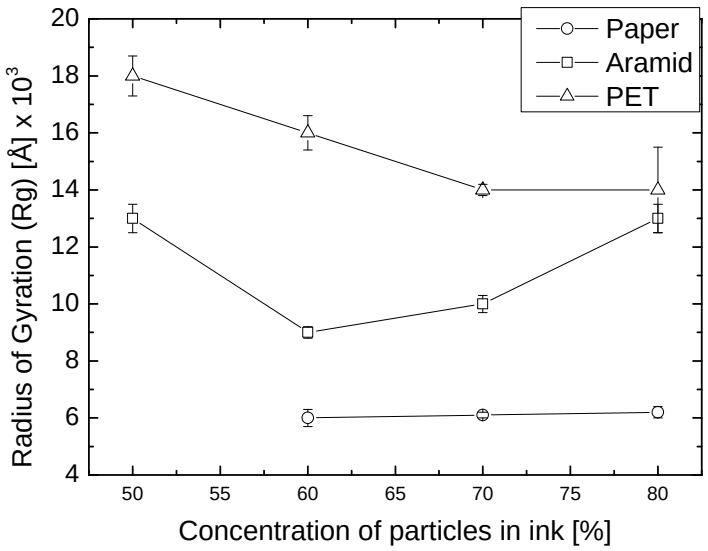

Figure 5.10: The second structural level radii of gyration obtained from fitting the unified equation to the different composition of HEM Si inks printed on three different substrates.

5.2.4 Influence of milling time on the aggregation of silicon nanoparticles in printed layers

Layers of particles screen printed on PET from water-based inks made up of 1 hour, 1.5 hours, 2 hours, 2.5 hours, and 3 hours HEM M-Si particles mixed at 70% particle weight ratios as described in section 4.3.2(c), were used to investigate the effect of milling time on aggregation of the particles using synchrotron USAXS. For each type of ink, nine different prints were measured for statistics. Figure 5.11 is an example log-log plot showing the desmeared USAXS profile of nine different samples of the 1.5 hour HEM M-Si particle layers with no scaling of the different data. There is a considerable overlap across the data which shows little deviation between printed layers of the same ink. The same was observed for data for the other milling times.

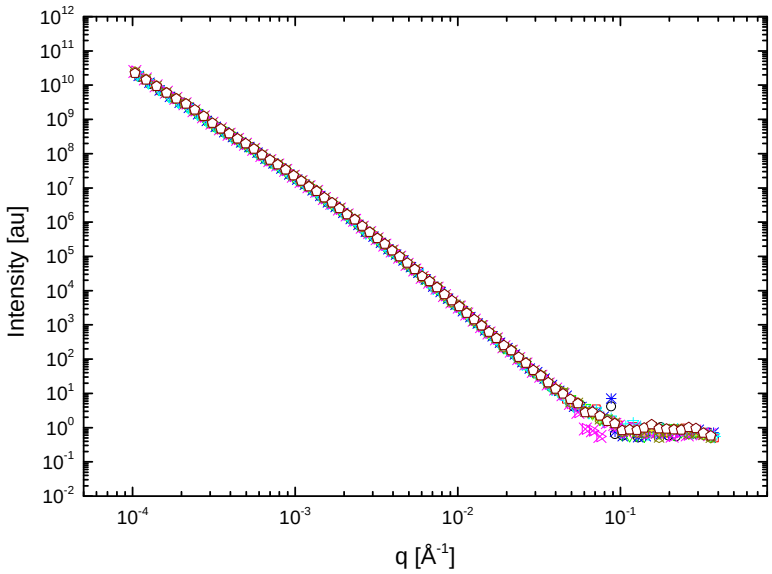

Figure 5.11: Corrected synchrotron USAXS data for 9 different layers of 1.5 hour HEM M-Si particles with no scaling of the data.

Fitting of the scattering data was achieved using the unified function, of which two structural levels were sufficient for all the samples. Table 5.11 shows a summary of the unified function fit results. The uncertainties in the table are the standard deviations of the mean obtained from all nine data sets for printed layers of the same ink. At high q, a Porod power law exponent of -4 was obtained for the primary particles. For increasing milling times of 1, 1.5, 2, 2.5 and 3 hours, decreasing average $R_{g,1}$ values of about 250 nm, 220 nm, 210 nm 180 nm and 170 nm respectively were obtained. However, for the aggregate sizes, an average $R_{g,2}$ value of 1000 nm was obtained for the different milling times except for 1.5 hour where 1300 nm was obtained. The aggregates all display mass fractal scattering with high values of α_2, similar to what was obtained from the unified fit of the USAXS data of all the 5 hour HEM M-Si particle layers investigated. Similarly to previous findings, the prefactors of the Guinier and power laws did not follow any trend.

Table 5.11: Fitting parameters using two structural levels of the unified function applied to the synchrotron USAXS data of different milling times of HEM M-Si particle inks with 70% particle weight printed on PET. Parameters with subscript 1 refer to primary particles and those with subscript 2 refer to aggregates.

Milling time (hours)	Level 1			Level 2			
	G_1	B_1	$R_{g,1}$(Å)	G_2	B_2	$R_{g,2}$(Å)	α_2
1	$1.7 \pm 0.4 \times 10^{8}$	$4.5 \pm 0.2 \times 10^{-4}$	2520 ± 150	$2.3 \pm 0.5 \times 10^{10}$	0.17 ± 0.01	10000 ± 600	2.78 ± 0.01
1.5	$7.4 \pm 1.1 \times 10^{7}$	$3.5 \pm 0.2 \times 10^{-5}$	2220 ± 80	$2.8 \pm 0.4 \times 10^{10}$	0.14 ± 0.01	13000 ± 500	2.77 ± 0.01
2	$9.1 \pm 2.0 \times 10^{7}$	$4.9 \pm 0.2 \times 10^{-5}$	2100 ± 100	$2.0 \pm 0.2 \times 10^{10}$	0.11 ± 0.01	10500 ± 400	2.82 ± 0.04
2.5	$5.3 \pm 1.6 \times 10^{7}$	$5.4 \pm 0.4 \times 10^{-5}$	1790 ± 120	$1.3 \pm 0.1 \times 10^{10}$	0.11 ± 0.01	10000 ± 400	2.80 ± 0.02
3	$4.7 \pm 1.2 \times 10^{7}$	$6.0 \pm 0.6 \times 10^{-5}$	1700 ± 106	$1.3 \pm 0.2 \times 10^{10}$	0.08 ± 0.01	10000 ± 600	2.83 ± 0.02

Figure 5.12 shows the variation of the radii of gyration obtained for the first and second structural levels. The error bars shown are the standard deviations of the mean obtained from nine prints of the same ink, except for the 5 hour sample shown in figure 5.12a which was taken from table 5.10 for a single sample. From figure 5.12a, the average $R_{g,1}$ values decreases almost linearly with increase in milling time. The 170 nm $R_{g,1}$ obtained for the 180 minutes milled particles is almost twice the average value of about 90 nm obtained for the 5 hour milled particles. In the case of the aggregates, similar $R_{g,2}$ values consistent in the order of magnitude with previous findings reported for the layers on PET were obtained.

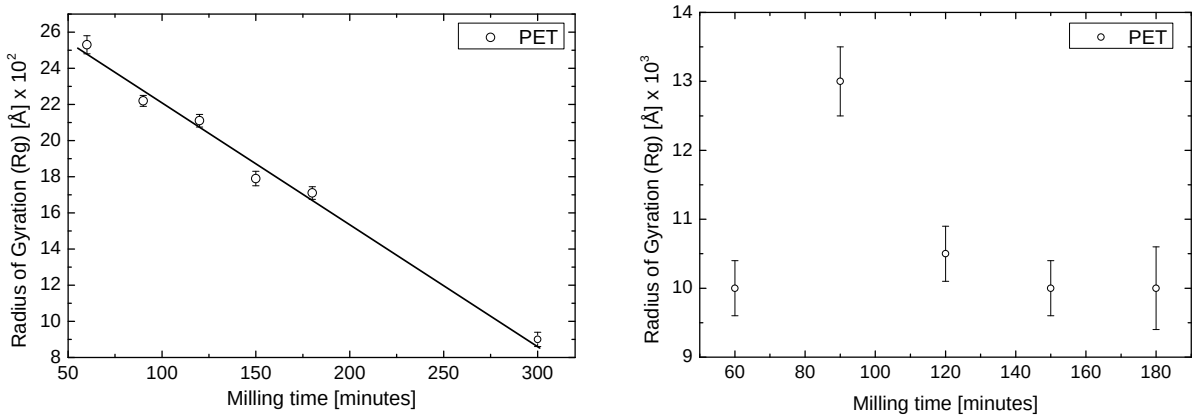

(a) (b)

Figure 5.12: Variation of the radii of gyration obtained for (a) first structural level, and the (b) second structural level, with milling times. The bars are the standard deviation of the means from 9 samples, except for the 5 hour sample in (a) taken from figure 5.9c.

5.2.5 Investigation of the surface topology of printed layers using WALq

The new WALq technique described in section 4.3.3 which uses low energy X-rays scattered at wide angles, was used to study the surface topology of printed layers of acrylic water-based and CAB solvent-based inks composed of 80%, 50% and 20% particle weight ratios of 3 hour HEM M-Si and 5 hour HEM P-Si nanoparticles, as well as laser synthesised I-Si nanoparticles for comparison. The relative scattering intensity I(θ) for each sample was obtained by normalising the output intensity data with respect to the beam intensity incident on each sample. This was further reduced to I (q) using the equation,

$$I(q) = I(\theta)\left(\frac{dq}{d\theta}\right)^{-1}, \tag{5.1}$$

where,

$$\frac{dq}{d\theta} = \frac{4\pi}{\lambda}\cos(\theta). \tag{5.2}$$

This reduction process was used for both the 2 nm and 13 nm wavelengths, and both data were combined to give the scattering profile for a sample. A log-log plot of the intensity versus q for the paper substrate is shown in figure 5.13. The point of combination of the 2 and 13 nm wavelength data is shown in the figure indicating continuity in the scattering data.

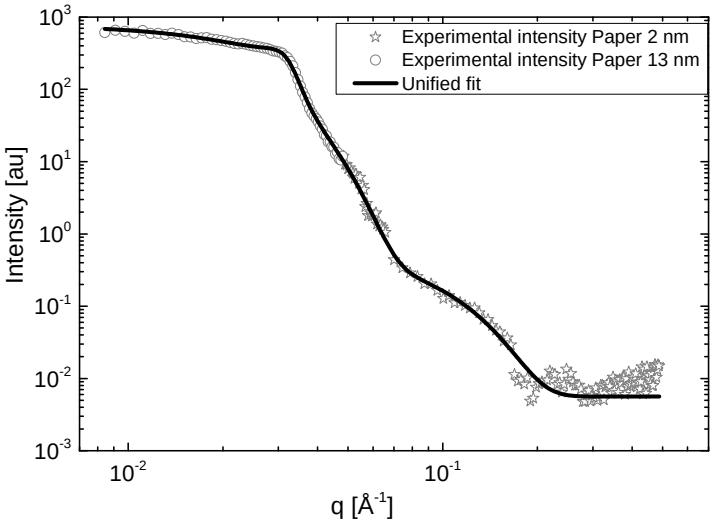

Figure 5.13: WALq scattering spectrum obtained for paper substrate. The *solid line* represent the unified fit to the data.

About five orders of magnitude variation in intensity was obtained within the q range covered in this experiment. At low q, the data plateaus to the limit of the instrument used. This was followed by several broad peaks with increase in q, terminating with a constant background at high q similar to what was observed in the synchrotron USAXS data.

Figure 5.14 shows log-log plots of data from the 80% particle weight ratios of the water-based inks as examples. Features similar to the paper scattering profile was observed in the scattering profile of all the layers from the water-based inks. However, the broad peak at $q \approx 0.1$ Å^{-1} in all three figures was not observed in the substrate scattering data, and is therefore to be interpreted as a feature that arises due to scattering from the nanoparticle layer. Two or more peaks similar to diffraction peaks of regular structures were observed at $q > 0.15$Å^{-1}. These were unexpected since this work was concerned only with the small angle scattering features. These peaks are probably associated with diffraction from the polymer binder, but suitable samples with thick layers of binder only were not available at the time of measurement to investigate this further. However, the structure of a polymer layer without nanoparticle filler may be different.

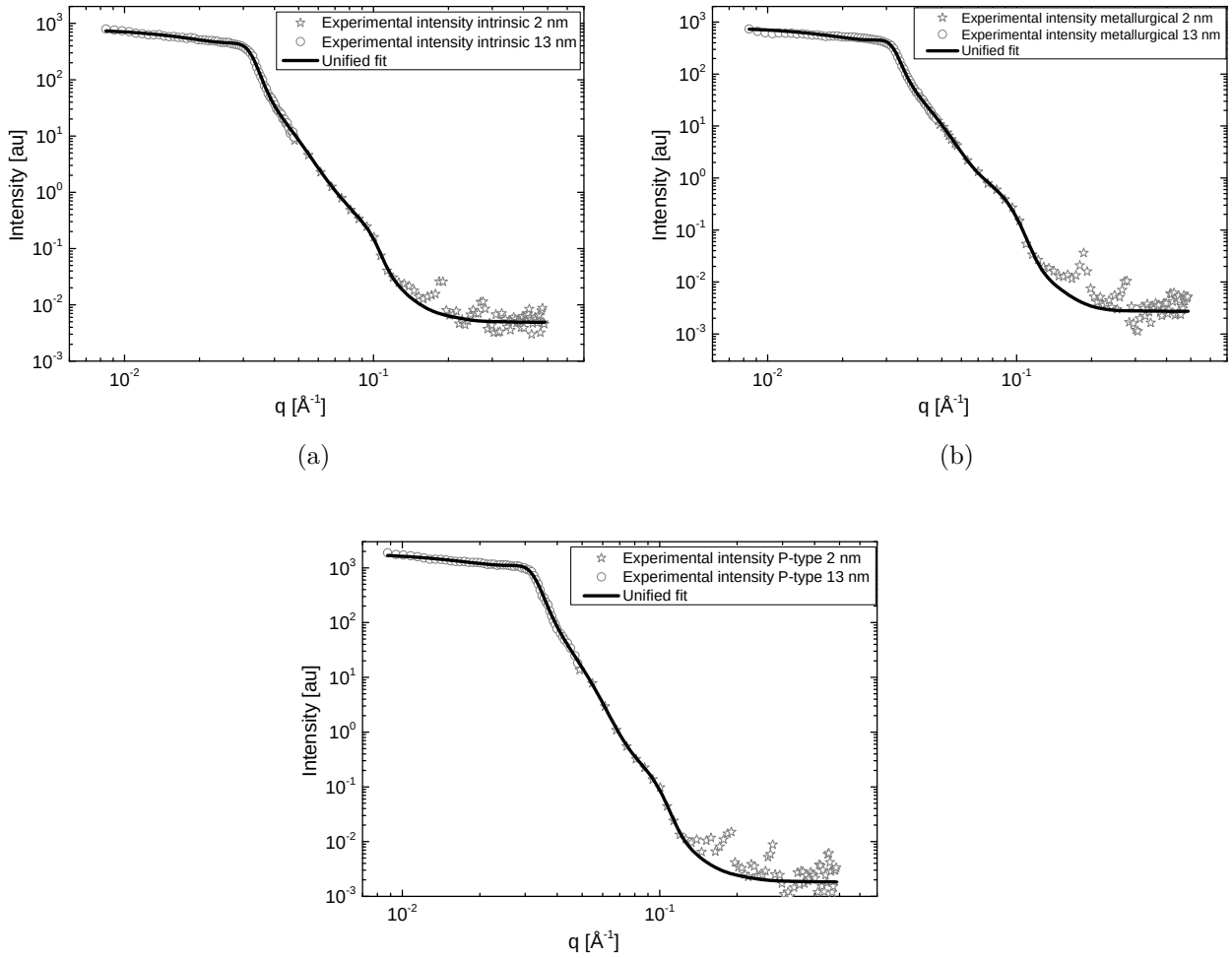

Figure 5.14: WALq scattering spectra obtained for 80% (a) I-Si, (b) HEM-M and (c) HEM-P nanoparticles from the water-based ink. The solid line through each data is a fit of structure factor modified unified function.

Figure 5.15 shows log-log plots of data from the 80% particle weight ratios of the solvent-based inks as examples. The paper scattering features observed in the profiles for water-based inks was not observed in the scattering data of the solvent-based inks except for the layers from inks with low silicon particle concentration of 20%. However, the peak observed in figure 5.15c at very low q was present in few samples, and could probably be associated with the substrate. At $q > 0.08\text{Å}^{-1}$, up to five or more diffraction peaks, more pronounced than in the layers produced using the water-based inks, were observed for all the layers deposited with the solvent-based inks.

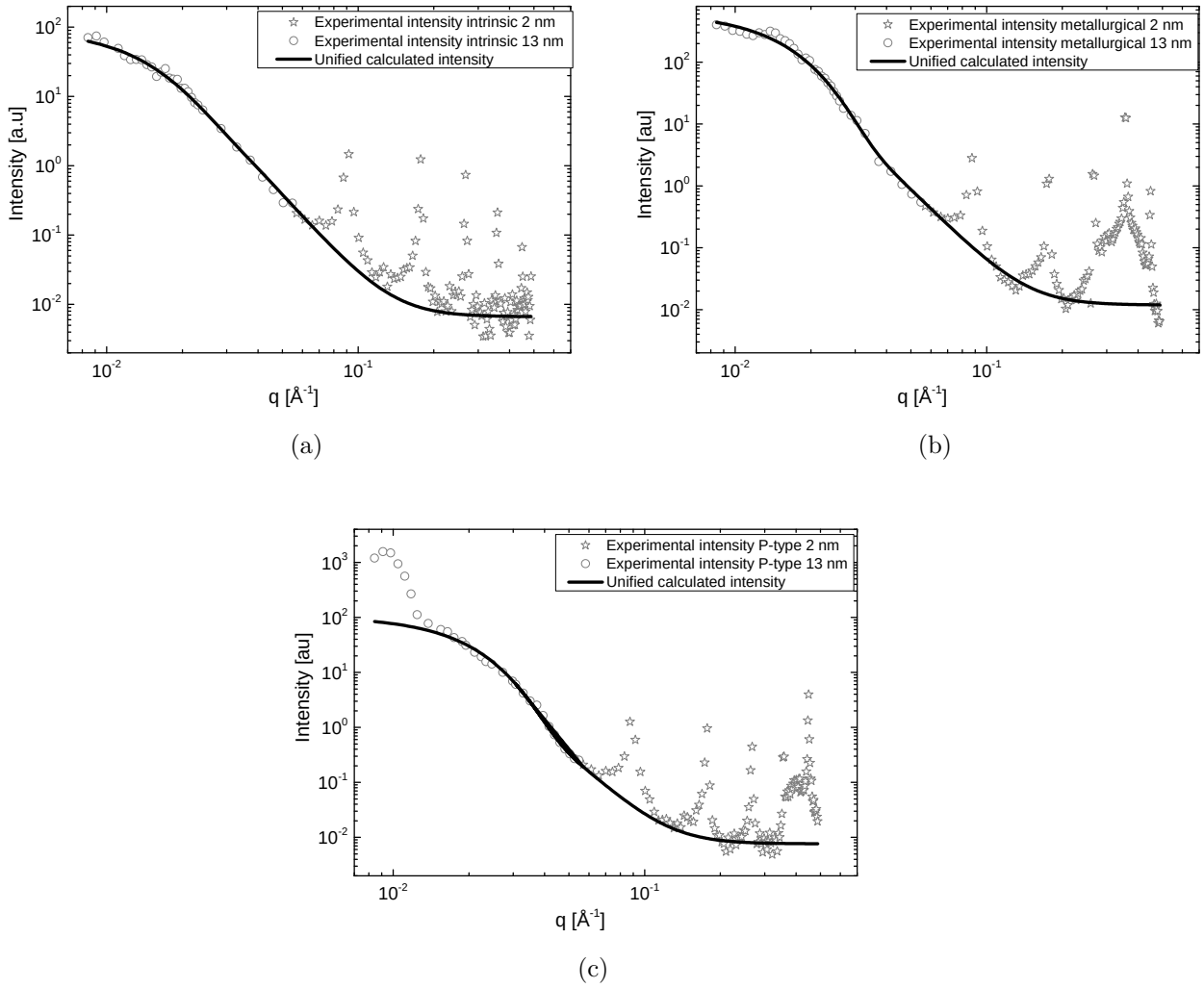

Figure 5.15: WALq scattering spectra (grey circles) for (a) I-Si, (b) HEM-M and (c) HEM-P nanoparticles from the solvent-based ink. The solid line through each data is the unified fit (Eq. 3.19) with four levels. The second and fourth levels were modified with the structure factor equation (Eq. 3.21).

The data sets are treated as small angle scattering data relative to the wavelength of the incident radiation since the scattering angles are well below the first diffraction peak for silicon at these wavelengths. The solid line through the paper sample data in figure 5.13 is a fit to the unified function in equation 3.19 for three structural levels with third level modified using the structure function (Eq. 3.21) as described in section 3.1.3. The parameters for the fit are shown in table 5.12. The high q power law was not observed, so the power law prefactor α_1 was given a zero value as shown in the table. From the fit results, three sizes given by $R_{g,1}$, $R_{g,2}$, $R_{g,3}$ were obtained as 1.9 nm, 6.7 nm and 11.4 nm for the paper substrate.

A correlation length ζ of 17.7 nm was obtained for the structural features of the third level, with packing factor κ of about 8.4.

Table 5.12: Fitting parameters using three structural levels of the unified function to the scattering data of the paper substrate, with the third structural level modified with the correlated function.

Fitting parameters	Level 1	Level 2	Level 3
G	0.52	309.5	4234
B	0	1.0×10^{-6}	5.6×10^{-5}
R_g (Å)	19.1 ± 1.2	67.1 ± 0.7	114.5 ± 7.1
α	-	4	4
ζ (Å)	-	-	177.3 ± 5.4
κ	-	-	8.4

Samples from the water-based inks were fitted with the unified function with $n = 4$ (*solid lines* in figures 5.14). Since the paper features were observed in these scattering data, the fit parameters for the paper substrate ($R_{g,i}$ and α_i) were fixed for the three levels seen as the paper contribution. The level associated with the particles (0.0787 Å$^{-1} \leq q \leq 0.1048$ Å^{-1}) was modified with the structure function in equation 3.21 to fit the broad peak. A summary of the results obtained for all the layers from the water-based inks are shown in table 5.13. From the table, the radii of gyration obtained for the silicon nanoparticle layers ranges from 3.9 nm to 5.2 nm. These values are independent of the particle concentration in the inks or the type of nanoparticles used. A correlation length in the range of 5.5 nm to about 7 nm was obtained for the particle features, which have packing factors ranging from 4.1 to as high as 9.5. For these particle features, a slope of -4 was obtained indicating Porod scattering.

Table 5.13: Fitting parameters for the four structural level of fitting the unified function to the scattering data of the acrylic based layers, with the second and fourth structural levels modified with the correlated function.

Sample	weight(%)	Fitting parameters					
		G	B	α	R_g (Å)	ζ (Å)	κ
I-Si	80	81.04	1.62×10^{-6}	4	49.1 ± 0.3	55.9 ± 0.1	7.94
	50	9.79	3.05×10^{-6}	4	39.9 ± 0.7	67.6 ± 1.3	2.86
	20	8.88	3.83×10^{-6}	4	39.2 ± 0.3	59.7 ± 0.1	4.29
HEM-M	80	15.47	3.65×10^{-7}	4	39.5 ± 0.2	57.4 ± 0.1	4.74
	50	157.91	1.09×10^{-6}	4	49.5 ± 0.3	58.1 ± 1.0	8.85
	20	97.22	1.04×10^{-6}	4	51.6 ± 0.4	58.6 ± 0.1	9.02
HEM-P	80	16.67	7.44×10^{-7}	4	43.1 ± 0.3	54.6 ± 0.2	5.83
	50	7.00	4.32×10^{-7}	4	39.1 ± 0.7	68.8 ± 1.6	4.19
	20	19.98	4.32×10^{-7}	4	50.0 ± 1.3	60.6 ± 0.1	9.48

For the layers of particles produced from the solvent-based inks, only a single level ($n = 1$) of the unified function with no modification was required to fit the scattering data, except for the layers with 20% particle concentration that required the structure factor modification for the broad peaks observed at low q. A summary of the results obtained for all the layers from the solvent-based inks are shown in tables 5.14. The radii of gyration for these layers ranges from 8.4 nm to 13 nm, which is about twice the values obtained for the acrylic-based samples. For the layers with only 20% particles, correlation length in the range of 33.1 nm to 33.7 nm was obtained for the features on the layers, which have smaller packing factors in the range 3.1 to 3.7. Porod scattering was also observed for these scattering features.

Table 5.14: Fitting parameters using one structural level of the unified function to the scattering data of the CAB based layers, with the modified correlated function used for layers with 20% particles.

Sample	weight(%)	Fitting parameters					
		G	B	α	R_g (Å)	ζ (Å)	κ
I-Si	80	93.26	2.36×10^{-6}	4	130.3 ± 0.6		
	50	82.09	1.34×10^{-6}	4	124.4 ± 0.3		
	20	74.95	2.06×10^{-6}	4	117.5 ± 0.8	337.0 ± 1.3	3.11
HEM-M	80	628.70	5.38×10^{-6}	4	122.8 ± 0.2		
	50	61.72	1.08×10^{-6}	4	113.7 ± 0.4		
	20	1149.10	6.86×10^{-6}	4	129.2 ± 0.2	337.8 ± 0.6	3.86
HEM-P	80	104.99	1.93×10^{-6}	4	97.2 ± 0.2		
	50	27.01	1.72×10^{-6}	4	84.4 ± 0.3		
	20	69.64	1.02×10^{-6}	4	110.6 ± 0.2	330.9 ± 0.7	3.28

5.3 Electrical characterisation

Layers of 1.5 hour HEM M-Si particles produced from water-based inks of 80%, 70%, 60% and 50% particle weight concentrations, and screen printed on PET were investigated electrically in the same uncalendared state as when they were investigated with USAXS as described in section 4.3.2(d), except for the metal contacts which were later overprinted onto the layers (see section 4.4). Usually, most printed electronic devices have layers which are sintered or compacted [112, 125, 126] to enhance stability of the device property, but in this case no further processing was carried out after the layers were dry. The V-I characteristics of two of the layers is shown in figure 5.16. For low particle loadings (50% to 70%), the shape of the curve is dominated by the curved region seen at the left of the curve in figure 5.16a, while for high particle loading (80%), the shape of the curve is composed of the curved region on the left and a symmetric curve on the right (figure 5.16b). The curved shape of the V-I plot arises from the presence of capacitance in the printed layers. During holding time of the V-I measurement, there is a build up of charge which is discharged as the measurement

progresses, resulting in the shapes in figure 5.16 which have a characteristic "hockey stick" form.

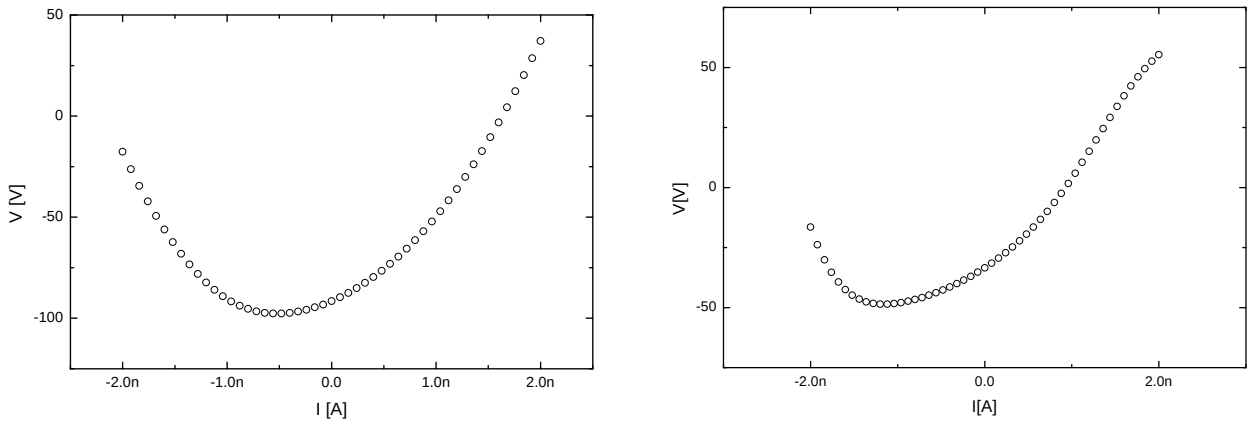

(a) (b)

Figure 5.16: V-I characteristics of a printed HEM metallurgical silicon layer in an uncalendared state. The low particle loading (a) is dominated by the charging region while the higher particle loading (b) is composed of charging and symmetric regions.

The other contribution to non-linearity in the V-I plot can be associated with the numerous interfaces present in the system. These interfaces could be between similar particles in the conducting paths, but also at the junction between the metal electrodes and the silicon nanoparticles [127, 128]. A proposed equivalent circuit for the symmetry in this system can be represented as two diodes connected back to back in series with a resistor as shown in figure 5.17. The diodes 1 and 2 are as a result of the symmetry present in the system due to the interfaces, and the series resistance R_s is the effective bulk resistance of the conducting paths in the system [128].

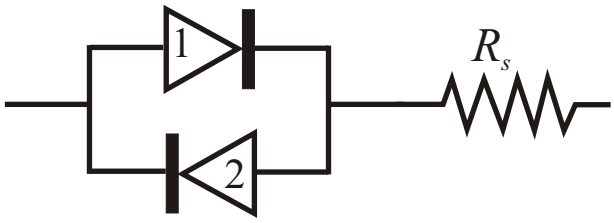

Figure 5.17: Equivalent circuit for symmetric diode behaviour of the nanoparticles in the printed structure.

The equation for current I_D through a diode under applied voltage V is given by

$$I_D = I_0 \left[\exp\left(\frac{eV_D}{\eta k_B T} \right) - 1 \right], \tag{5.3}$$

where e is the electronic charge, η is the diode ideality factor, k_B is the Boltzmann constant, V_D is the voltage drop across the diode, I_0 is the reverse saturation current, and T is the temperature at which the measurement was carried out. If the current in figure 5.17 is in the direction left to right, the diode 1 is in forward bias mode and the current through the circuit can be represented as a serial combination of diode 1 and R_s. The same condition holds for diode 2 if the direction of the current is reversed. Using equation 5.3 to describe the diodes above, the current due to diode 1 is given by

$$I_1 = I_0 \left[\exp\left(\frac{e(V_D - IR_s)}{\eta k_B T} \right) - 1 \right], \tag{5.4}$$

and the current through diode 2 is given by

$$I_2 = -I_0 \left[\exp\left(\frac{-e(V_D - IR_s)}{\eta k_B T} \right) - 1 \right]. \tag{5.5}$$

Due to the symmetry in the material, the magnitudes of I_0 and η are assumed to be the same for both diodes. Combining equations 5.4 and 5.5, the total current describing the symmetric behaviour of the curve is given by [129]

$$I = I_0 \left[\exp\left(\frac{e(V_D - IR_s)}{\eta k_B T} \right) - \exp\left(\frac{-e(V_D - IR_s)}{\eta k_B T} \right) \right]. \tag{5.6}$$

For a current sweep through the circuit, equation 5.6 can be rearranged to express V_D in terms of I as

$$V_D = \frac{\eta k_B T}{e} \ln \left| \frac{1}{2} \left\{ \left(\frac{I}{I_0} \right) + \sqrt{\left(\frac{I}{I_0} \right)^2 + 4} \right\} \right| + IR_s. \tag{5.7}$$

Equation 5.7 describes the voltage through the nanoparticles when they behave as symmetric diodes in the absence of any capacitive coupling. In a case where capacitance exist, figure 5.18 can be used as an equivalent circuit to describe the voltage through the nanoparticles during current sweep. The capacitor C in the figure could be attributed to gaps between conducting paths and R_c, is the resistance associated with the capacitor. The other parameters in figure 5.18 are as a result of the same conditions described for figure 5.17.

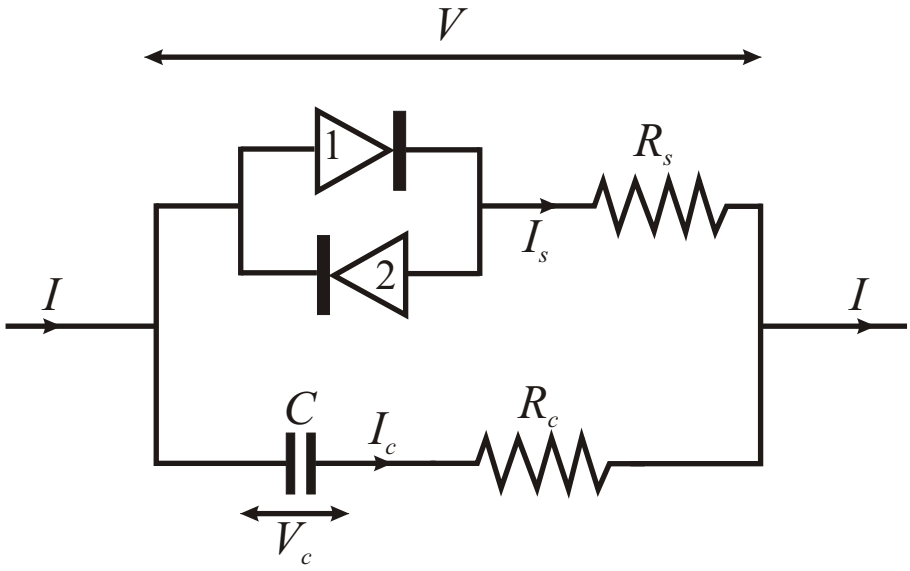

Figure 5.18: Equivalent circuit for printed structure during current sweep.

The total current I, through the circuit in figure 5.18 during current sweep mode is given as

$$I = I_s + I_c, \tag{5.8}$$

where I_s and I_c are the currents through R_s and C respectively. The potential V across the printed layer based on the circuit in figure 5.18 is given as

$$\begin{aligned} V &= V_D + I_s R_s \\ &= V_c + I_c R_c, \end{aligned} \tag{5.9}$$

where the potential across the C is given as

$$V_c = \frac{Q_c}{C}. \tag{5.10}$$

Using equations 5.9 and 5.10, equation 5.8 can be written as

$$I = \frac{Q_c}{R_s C} + \left(1 + \frac{R_c}{R_s}\right) I_c - \frac{V_D}{R_s}. \tag{5.11}$$

Differentiating equation 5.11 with respect to time, and setting $\tau_s = R_s C$, then

$$\frac{dI}{dt} = \frac{1}{\tau_s} I_c + \left(1 + \frac{R_c}{R_s}\right) \frac{dI_c}{dt} - \frac{1}{R_s} \frac{dV_D(I_s)}{dt}. \tag{5.12}$$

During holding time $-t_0 < t < 0$, and $I = J_0$, where t_0 and J_0 are the hold time and starting current respectively. Equation 5.12 reduces to

$$\frac{dI_c}{dt} = -\left(1 + \frac{R_c}{R_s}\right)^{-1} \frac{1}{\tau_s} I_c, \tag{5.13}$$

with the initial condition $I_c(-t_0) = J_0$. The solution of equation 5.13 is

$$I_c(0) = J_0 \exp\left\{-\left(1 + \frac{R_c}{R_s}\right)^{-1} \frac{t_0}{\tau_s}\right\}. \tag{5.14}$$

For $t > 0$, $I = J_0 + \beta t$, where β = current step/ sweep delay. Equation 5.12 becomes,

$$\beta = \frac{1}{\tau_s} I_c + \left(1 + \frac{R_c}{R_s}\right) \frac{dI_c}{dt}, \tag{5.15}$$

which can also be written as

$$\frac{dI_c}{dt} = \left(1 + \frac{R_c}{R_s}\right)^{-1} \beta - \left(1 + \frac{R_c}{R_s}\right)^{-1} \frac{1}{\tau_s} I_c. \tag{5.16}$$

Equation 5.16 is a separable differential equation of the form $dy/dx = a - by$. Solving the differential equation yields

$$I_c = \tau_s \left(1 + \frac{R_c}{R_s}\right) \left\{\left(1 + \frac{R_c}{R_s}\right)^{-1} \beta - W \exp\left[-\left(1 + \frac{R_c}{R_s}\right)^{-1} \frac{t}{\tau_s}\right]\right\}. \tag{5.17}$$

The value of the constant W in equation 5.17 can be determined from equation 5.14 with time $t = 0$. This will yield a final solution for I_c as

$$I_c = \tau_s \beta - \left[\tau_s \beta - J_0 \exp\left\{-\left(1 + \frac{R_c}{R_s}\right)^{-1} \frac{t_0}{\tau_s}\right\}\right] \exp\left\{-\left(1 + \frac{R_c}{R_s}\right)^{-1} \frac{t}{\tau_s}\right\}. \tag{5.18}$$

The current through R_s can be determined by substituting equation 5.18 for I_c in equation 5.8, and also substitute for t.This will yield the current through R_s as

$$I_s = I - \tau_s \beta - \left[\tau_s \beta - J_0 \exp\left\{-\left(1 + \frac{R_c}{R_s}\right)^{-1} \frac{t_0}{\tau_s}\right\}\right] \exp\left\{-\left(1 + \frac{R_c}{R_s}\right)^{-1} \frac{t}{\tau_s}\right\}. \tag{5.19}$$

Substituting for I_s in equation 5.9, the voltage through the circuit is given by

$$V = V_D(I_s) + \left(I - \tau_s \beta - \left[\tau_s \beta - J_0 \exp\left\{-\left(1 + \frac{R_c}{R_s}\right)^{-1} \frac{t_0}{\tau_s}\right\}\right] \exp\left\{-\left(1 + \frac{R_c}{R_s}\right)^{-1} \frac{t}{\tau_s}\right\}\right) R_s. \tag{5.20}$$

Due to the charging of the layers, the V-I curve does not pass through the origin as seen in figure 5.16. To account for the shift, equations 5.7 and 5.20 were modified as

$$V_D = \frac{\eta k_B T}{e} \ln \left| \frac{1}{2} \left\{ \left(\frac{I_s}{I_0} + \Delta I\right) + \sqrt{\left(\frac{I_s}{I_0} + \Delta I\right)^2 + 4} \right\} \right| + I R_s, \tag{5.21}$$

and,

$$V = V_D(I_s) + \left(I - \tau_s\beta - \left[\tau_s\beta - J_0 \exp\left\{ -\left(1 + \frac{R_c}{R_s}\right)^{-1} \frac{t_0}{\tau_s} \right\} \right] \exp\left\{ -\left(1 + \frac{R_c}{R_s}\right)^{-1} \frac{t}{\tau_s} \right\} \right) R_s - \Delta V, \tag{5.22}$$

where ΔI and ΔV are the shifts in the current and voltage axes respectively. Equation 5.22 was fitted to all the samples. Examples of the fitted data are shown in figures 5.19a and 5.19b. No appreciable difference was observed in the distribution of the diode ideality factor η, and the reverse saturation current I_0. Since the samples all had same type of nanoparticles, the diode behaviour was expected to be similar for all the samples. Also, the mean value of R_c for all the samples was of the order of 10^9 Ω, which implies that the effective gap between the conducting paths may be similar. Generally, for the samples with 50 to 70% particle concentration, the resistance in the capacitive branch R_c is less than the lumped bulk resistance R_s by 1 or 2 orders of magnitude, but in the case of the samples with 80% particle concentration, both parameters have similar magnitude. The similarity of R_s and R_c at high particle loadings is probably coincidental and no physical significance can be attributed to it.

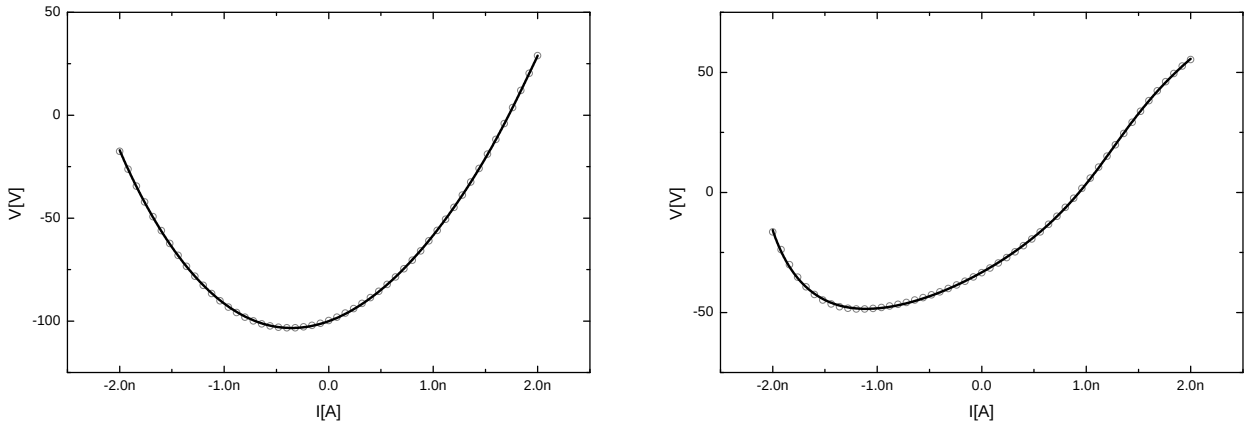

(a) (b)

Figure 5.19: V-I characteristic curves of (a) 50% and (b) 80% HEM metallurgical silicon nanoparticle concentration fitted with equation 5.22.

Figure 5.20 shows the variation of the mean series resistance R_s (Fig. 5.20a) and capacitance C (Fig. 5.20b) values obtained from the fit to the V-I data, with the radius of gyration for the first structural level R_g obtained from USAXS. Since all the samples were prepared with same dimensions as described in section 4.1.2, a resistance of 50 GΩ on figure 5.20a

corresponds to sheet resistivity of 50 GΩ/□. The error bars are the standard deviation of the mean. As expected, the effective resistance decreased with increase in particle loading, and this follows the decrease in length between the primary particles as indicated by the trend of R_g. The decrease in gap between the particles will lead to an increase in the conducting path which results in the lower resistances determined for the samples with higher particle concentration. Despite the high resistance values recorded for the samples which was due to the uncalendared state of the layers, the variation was consistent for the different samples. Also, the variation of the error bars in figure 5.20a indicates a broader spread with decrease in particle concentration. Generally a calendared layer is not only mechanically more stable but is more similar to polycrystalline silicon with better electronic properties including a lower resistivity and less capacitance [128], but for the purpose of comparing with USAXS data, calendared samples were not considered. The concentrations with less spread in R_s, may be above the percolation threshold of the system, but this require more studies as it was not investigated in this work. Unlike R_s, the distribution of C tends to increase with increase in particle loading as shown in figure 5.20b. The error bars shown in the plot are smaller for the samples with lower particle concentration, and this is also in complete opposite to the error bars associated with the resistance values.

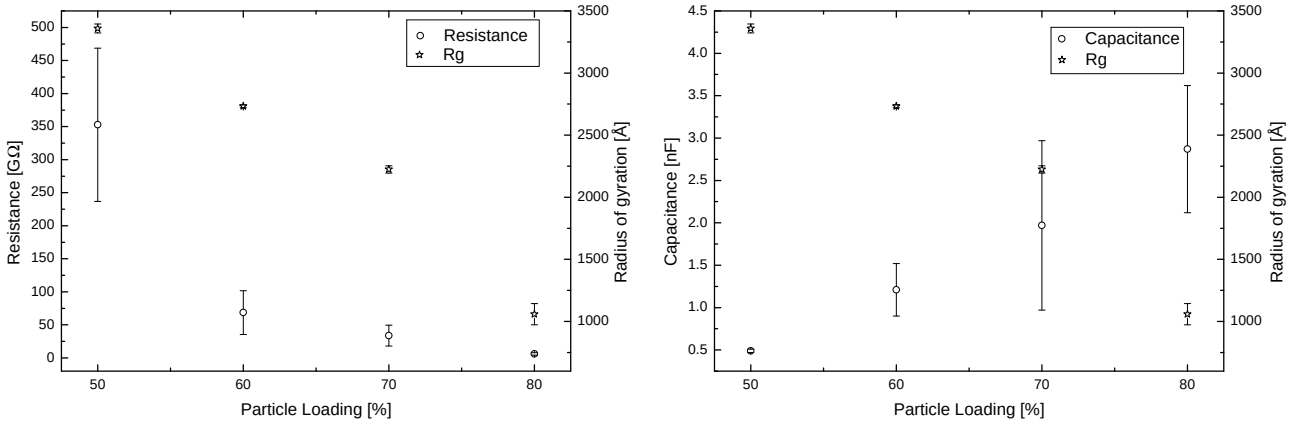

(a) (b)

Figure 5.20: Variation of the first radius of gyration $R_{g,1}$ from USAXS measurements plotted with (a) effective series resistance, R_s and (b) effective capacitance, C versus concentration of metallurgical silicon nanopaticles.

6. Discussion

The silicon nanoparticles produced by high energy milling are aggregated when in the powder phase as shown in section 5.1. This aggregation found by investigation using scattering techniques was also found to persist in the printed layers. The compact nature of the aggregates makes it difficult to resolve the size of the individual primary particles in microscopy studies. This is a common challenge in top-down production process of nanoparticles when no post-fabrication treatment is applied to separate the particles [48]. Small angle scattering techniques have been used to study the aggregation of the silicon nanoparticles in printed layers, with the quantification of the average number of primary particles in branching state of nanoparticulate aggregate systems demonstrated [70, 71].

Using the unified function (equation 3.19) to fit USAXS data from 5 hour milled Si nanoparticles as discussed in sections 5.2.1, 5.2.2 and 5.2.3, the radius of gyration $R_{g,1}$ of the primary particles was determined to be in the range of 40 nm to 60 nm. The Sauter mean diameter d_p obtained using equation 3.40 was found to be about 45 nm, which falls within the obtained range of the radius of gyration, but is significantly different from the 130 ± 3 nm and 80 ± 2 nm determined by TEM studies (section 5.1) for the long and short axes respectively of the nanoparticles. Calculating the average size directly from the radius of gyration using equation 3.16 assuming spherical particles, a value of about 130 nm is obtained, which indicates that this method yields a value which is about 3 times the value obtained for the Sauter mean diameter. Similarly, the size determined for the bottom-up TCP synthesised Si nanoparticles was about 22 nm for the Sauter mean diameter which is similar to the reported size of these particles determined by TEM in previous literature [45], and about 32 nm using $R_{g,1}$ in equation 3.16 assuming spherical particle. The discrepancy between the two ways of calculating the average size in SAS data analysis is because $R_{g,1}$ reflects the ratio of the eighth to the sixth moment of the size distribution which is sensitive to the presence of large particles [96], while d_p reflects the ratio of the third to the second moment of the distribution [97, 130]. It has been shown in the analysis of USAXS data of flame-made silica nanoparticles, that d_p is comparable to sizes determined from gas adsorption techniques [97] using BET analysis [99]. This indicates that the Sauter mean diameter, which like the radius of gyration is independent of the shape of the scattering particle, is the best parameter to be used as a measure of the average particle size in a distribution. It implies that at 5 hours of milling, the average size of the distribution of the silicon particles is in the nanoscale. This is not the case for the 1, 1.5, 2, 2.5 and 3 hour milling times discussed in section 5.2.4. From

the values of $R_{g,1}$ obtained from the USAXS data with respect to different milling times as shown in figure 5.12a, there is a decrease in the average size of the nanoparticles with increased milling time. Since the values of $R_{g,1}$ are comparable to d_p, none of the milling times above resulted in particles with an average size less than 100 nm except for the 5 hour milled. The decrease in size with milling time shows a linear trend up to the fifth hour, instead of an exponential decrease as predicted in the literature [100]. Since for all these layers investigated, inks with the same particle loading of 70% were used, it is expected that the scattering reflects the size of the primary particles making up the scattering aggregates in the layers. Therefore, the implication of the observed linear relationship is that the milling time required for the average nanoparticle size to be saturated is beyond the 5 hours milling time, as investigated in this work.

With the variation in the concentration of 5 hour HEM M-Si nanoparticles in the inks forming the layers as seen in section 5.2.3, the primary particle radius of gyration $R_{g,1}$ also decreases linearly with increasing particle loading (figure 5.9). In this case, any change in R_{g1} will reflect the separation between particles, since the agglomeration of the particles and aggregates will depend largely on the powder concentration in the inks. Therefore, the linear relationship of R_{g1} with respect to concentration describes a change in the mean particle separation of the primary particles, with the separation in the higher particle concentration samples close to the average particle size. For the same concentration of particles in the ink, similar values of $R_{g,1}$ were obtained independent of which substrate the inks were printed on, indicating that at the primary particle level, variation in separation does not depend on substrate when a single type of ink is deposited. It should be mentioned here that this variation determined from USAXS data analysis cannot be easily obtained from SEM for the HEM particles, because of the compact nature of the as milled and printed aggregates seen in figures 5.1, 5.3a and 5.3b.

The aggregate sizes, described by the second level radius of gyration $R_{g,2}$ from the unified fit were obtained from the USAXS data of printed layers. Unlike $R_{g,1}$ which does not depend on the substrate used, but on the concentration of particles and milling time, $R_{g,2}$ shows a trend which is largely dependent on both the substrate on which the layers were deposited and the nature of the inks used [70]. Generally, on porous substrates such as paper, the aggregate size is smaller than that in layers deposited on the non-porous substrates (i.e. PET), as shown for the HEM M-Si particles in table 5.4, tables 5.8 to 5.10 and summarised in figure 5.10. A possible explanation for the trend in the $R_{g,2}$ values for the different substrates lies in the liquid phase deposition and drying processes. For the porous substrate, capillary

flow of the liquid binder out of the layer into the substrate leads to the formation of a denser network than for a non-porous substrate where all the liquid remains in the layer until it is completely cured [70]. Similarly, the solvent-based ink system with large values of $R_{g,2}$ values compared to the water-based ink, dries by rapid evaporation of the solvent from throughout the layer, with essentially no flow of the binder out of the layer, leading to a more open network structure with more binder between the particles and aggregates as shown in figures 5.3b and 5.3d. An implication of this, is that the aggregates from the water-based ink systems will have structures with more particles in contact as compared to the aggregates from the solvent-based ink systems.

For all the USAXS data analysis, the aggregates of HEM Si nanoparticles have mass fractal structures with fractal dimension d_f above 2 but less than 3. These values of d_f obtained suggest that the aggregates have a compact structure. TCP synthesised nanoparticles also form mass fractal aggregates but with d_f less than 2, which implies more open chain-like networks of particles in the aggregates. For d_f larger than 2, a two dimensional projection of the surface of the layer should appear as an area filled with particles. In contrast for d_f smaller than 2, an open network of particles should appear. In the case of the HEM M-Si nanoparticle layers, both the SEM micrographs shown in figure 5.3a and 5.3b have aggregates which appear densely packed as expected from the value of d_f. However, while the TCP synthesised Si particle layers produced from the solvent-based ink does appear to follow the prediction of d_f for the SEM micrograph, the same cannot be said of the particle layers from the water-based ink. As seen in figure 5.3c, it is not obvious in the micrograph that the TCP particles have open aggregates, and this could be attributed to the curing process of the ink as described above. This limitation of the two dimensional SEM to give a true representation of the three dimensional aggregate feature of the TCP particles is one of the reasons complementary techniques, such as USAXS, are required for understanding the structure of these layers. Comparing the values of d_f from these USAXS results with the values obtained for simulation processes as described in section 2.2, the HEM M-Si nanoparticle aggregates are similar to aggregates formed by RLCA, while the TCP synthesised nanoparticles are similar to the normal DLCA model which is also referred to as cluster-cluster (CC) model [56]. However, to be able to fully model the aggregates formed by the HEM M-Si and TCP Si particles, more information about the aggregates is required, as presented below.

The scaling model described in section 3.2, applied to the USAXS data, shows that the 5 hour HEM M-Si nanoparticles form aggregates with large number (several thousands) of

primary particles as indicated by the degree of aggregation z in tables 5.2 and 5.6. As shown in the tables, the number of particles in an aggregate depends on the nature of the ink and also on the type of substrate the ink was deposited on. These results can be explained in a similar manner as for the aggregate radius of gyration $R_{g,2}$ given above, since z can also be calculated from the ratio of the radii of gyration of both the first (primary particles) and second (aggregate) levels [96]. The dimension of the minimum paths that traverse these aggregates was found to range from about1.1 to 1.2 for the HEM M-Si nanoparticles. This dimension is equivalent to a 10% to 20% sideways slip in the height of adjacent particles in a chain, which would otherwise have had a dimension of 1 if there were no slip as shown in figures 6.1a and 6.1b. The solid bar in figure 6.1b is an illustration showing the height slip from a linear chain between adjacent particles. Similar results were obtained for the TCP Si nanoparticle aggregates. This implies that the average minimum paths of the nanoparticle aggregates for both the HEM M-Si and the TCP Si nanoparticles are convoluted in a similar manner.

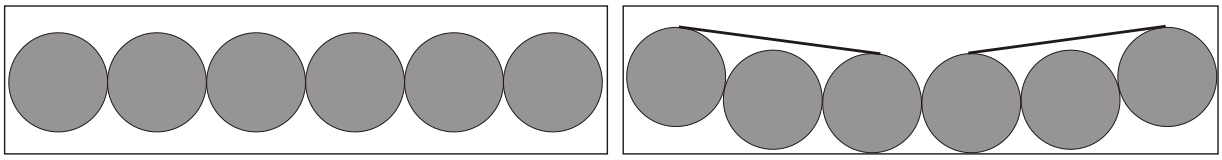

(a) (b)

Figure 6.1: Cartoons illustrating (a) an aggregate chain of particles with mass fractal dimension of 1, (b) an aggregate chain with mass fractal dimension of 1.1. The solid bar shows the slip from a linear chain between adjacent particles.

The 5 hour HEM M-Si aggregates, exhibit a connectivity dimension c of about 2.3 [70, 71] as seen in tables 5.2 and 5.6, which is an indication that the primary particles are highly connected. In contrast, the TCP synthesised nanoparticle aggregates have an average value of c of about 1.5 which indicates that the aggregates are less branched in comparison to the milled nanoparticles. Figure 6.2 shows the difference in the average number of particles in a branch segment, z_s for the aggregates of the HEM M-Si and TCP Si nanoparticles. The minimum path in the aggregates is indicated by the solid line. The 5 hour HEM M-Si nanoparticles have an average of about 4 particles per branch segment of the minimum path as shown by the darker spheres, while the TCP Si nanoparticles have only 2 particles per branch segment. The models using the values of c and z_s show why the aggregates formed by the HEM M-Si nanoparticles form a compact structure, while the TCP particle aggregates

form more open networks.

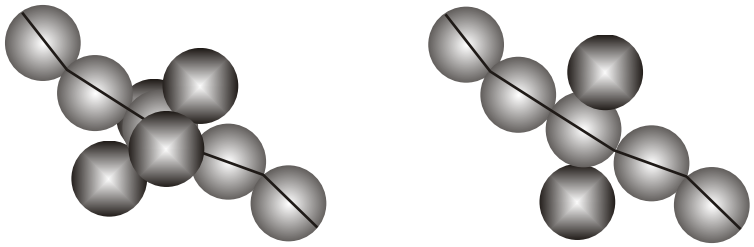

Figure 6.2: Illustration of the average number of particles per branch segment of an aggregate for the HEM M-Si and TCP Si nanoparticles.

The branch fraction, ϕ_{br} which is the mole fraction of the structure that is not included in the minimum path, is also a measure to show how compact an aggregate structure is. For the aggregates of the 5 hour HEM M-Si particles that have c greater than 2, the aggregates are close to a "regular" object defined as $c = d_f$ for a rod, disc or sphere [26], so it is expected that they have branch fractions of about 1 which is the result shown in tables 5.1 and 5.6. This is different for the TCP nanoparticles, where the average ϕ_{br} is about 0.6 indicating a less branched aggregate with more particles in the minimum path. The total number of branches n_{br} in an aggregate depends on the size of the aggregates, with the larger aggregates having more branches than the smaller ones. The milled particles with more branches have more particles per branch, z_{br} than the TCP synthesised nanoparticles as shown in tables 5.6 and 5.7.

The strength of the aggregate structure is determined by the magnitude of the coordination number C_N [131]. A larger value for C_N is also an indication of close-packing of the particles in the aggregate structure. The bonds in the aggregate structures formed by the TCP synthesised nanoparticles are strong in comparison to the 5 hour HEM nanoparticles. The value of C_N obtained for the HEM M-Si nanoparticles does not follow the prediction obtained by simulation for DLCA [57, 132] which gave values of more than 3 for the coordination number of aggregates with d_f greater than 2. On the other hand, C_N for the TCP nanoparticles falls within the range predicted by simulation for DLCA with d_f less than 2. This also shows that a slight modification to existing simulation mechanisms is required to account for these differences when modelling the aggregates of the HEM M-Si nanoparticles. Some of the differences between the TCP and HEM M-Si aggregates could be attributed to the surface

properties. The TCP nanoparticles have Si-H bonds [133] resulting in low surface free energy due to lack of hydrogen bonding at interfaces, while the HEM M-Si nanoparticles have been reported to have surfaces with a monolayer of silicon monoxide [124]. These properties are the subject of future investigations to further understand their influence on the aggregation of these materials.

The result obtained from the wide angle low q (WALq) experiment, which is a new surface scattering technique as described in section 4.3.3, shows that the radius of gyration of the particles on the surface is dependent on the nature of the ink, and independent on the type of silicon nanoparticles used in the printed layer. This can be attributed to the packing density of the particles in the different samples due to the flow properties of the binder as observed in the analyses of the USAXS data. The values obtained for the particle R_g in table 5.13 for the water based inks, and table 5.14 for the solvent based inks, are too small to be the size of the nanoparticles. For the I-Si nanoparticles, a radius of about 30 nm was reported from previous SAXS measurement [69], and from the USAXS measurements the 5 hour HEM M-Si nanoparticles are larger than 40 nm [70, 71]. A tentative explanation can be given in terms of the step height between neighbouring particles at the surface. As has been shown using the scaling relationship for USAXS data, the aggregates in the bulk of the silicon nanoparticle systems can be described using a branching system, with the minimum path which traverse the aggregate reported to be a chain with fractal dimension ranging from 1.1 to 1.2. These results have been correlated to the results shown in figure 6.1b to correspond to 10% and 20% slip in height between adjacent particles in a chain. The values of the radii of gyration obtained in the WALq measurement were only about 10% to 20% of the size of the nanoparticles measured with SAXS/USAXS, and therefore the radius of gyration can be related to the height difference between the particles forming the aggregates at the surface. If the aggregate length indicated in figure 6.1b, is increased by connecting the particle units end-to-end, then the height (side slip) will change by a factor of approximately 1.1 for the water-based and 1.2 for the solvent-based samples, resulting in a rough structures shown in figures 6.3 as the stacking procedure is repeated. The image shown is a one dimensional representation of the topology of the particle networks on the surface of the printed layers, with the 10% height slip between adjacent particles indicated by the gap between the line and circle underneath it. Similar rough features are expected for the solvent-based samples but with about 20% height slip.

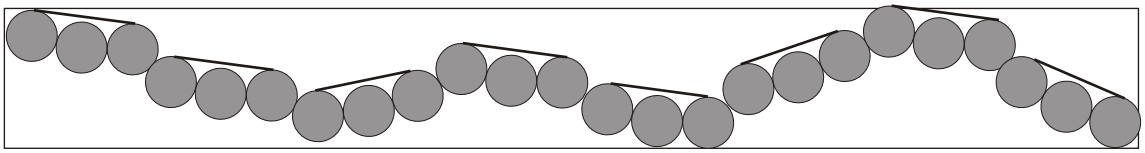

Figure 6.3: A one dimensional illustration of the formation of a rough surface from a chain with a mass fractal dimension of 1.1. The solid bar shows the slip from a linear chain between adjacent particles.

The feature of figure 6.3 is an indication that the network of particles on the surface have a similar topology to the particles in the bulk of the aggregates. This information was only inferred from the minimum path dimension from the scaling model applied to USAXS, but WALq has shown that there is a step height difference between adjacent particles on the surface. This information cannot be obtained with other techniques such as GISAXS or AFM, because of the high roughness and limited area which can be scanned. The average distance between the aggregates ζ ranges from about 55 to 70 Å for the water-based samples, resulting in a very rough surface composed of similar aggregate features illustrated in figure 6.3. It should, however, be mentioned here that $\zeta$was only obtained for the poorly printed layers on paper, and not for layers with good coverage.

From an electronic point of view, based on the results presented in section 5.3, the printed layers can be described in terms of a network of capacitors, resistors and diodes. The series resistance R_s is caused by the contact resistance between particles along a continuous path through the layer. This continuous path is a combination of the bulk resistance of the particles, internal structure of interfaces and interconnections between junctions [128]. In relation to the aggregates in the layers, the resistance and capacitance should depend on the distance between particles reflected in the Sauter mean diameter, and the minimum path length p as determined from the scaling model. Figures 6.4a and 6.4b shows the relationships between the Sauter mean diameter as determined from USAXS for the layers printed with different particle concentrations of the 90 min. HEM M-Si and the resistance and capacitance respectively, obtained from the fit of equation 5.22.

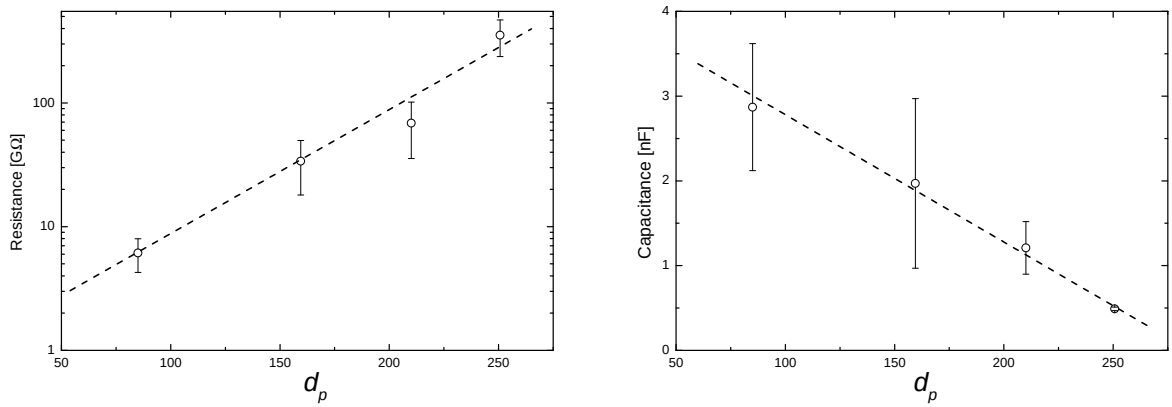

(a) (b)

Figure 6.4: Relationship between the Sauter mean diameter d_p of different particle concentration of the 90 min. HEM M-Si printed layers and (a) resistance of the layers, (b) capacitance of the layers obtained from equation 5.22. The lines are guides to the eye.

The resistance of the layers was found to have a non-linear relationship with the Sauter mean diameter as shown by the log-linear plot in figure 6.4a. This can be ascribed to the changing contact area between the primary particles in the layers. As the separation between the particles increases, the contact areas between these particle surfaces decreases resulting in an increase in the effective resistance of the layers. In figure 6.4b, the capacitance was found to have a linear relationship with the Sauter mean diameter. This can be explained using a parallel plate capacitor described by equation

$$C = \epsilon_r \epsilon_0 \frac{A}{d}, \tag{6.1}$$

where ϵ_r and ϵ_0 are the relative permittivity of the medium and free space respectively. With increase in the separation d of the particles, but the effective area between the particles does not change, therefore the effective capacitance decreases.

A fuller quantitative description is given by making use of the structural parameters derived from the scaling model. As far as the electrical properties are concerned, the basic circuit element is the minimum path p through the aggregate. This further needs to be scaled with the fractal dimension d_f to account for the three dimensional distribution of the paths in the aggregates. Figures 6.5a and 6.5b shows the relationship between the minimum path and fractal dimension of the aggregates with the resistance and capacitance respectively of the layers.

In terms of the minimum path, the fractal dimension is required to account for the three dimensional nature of the aggregates in the layers.

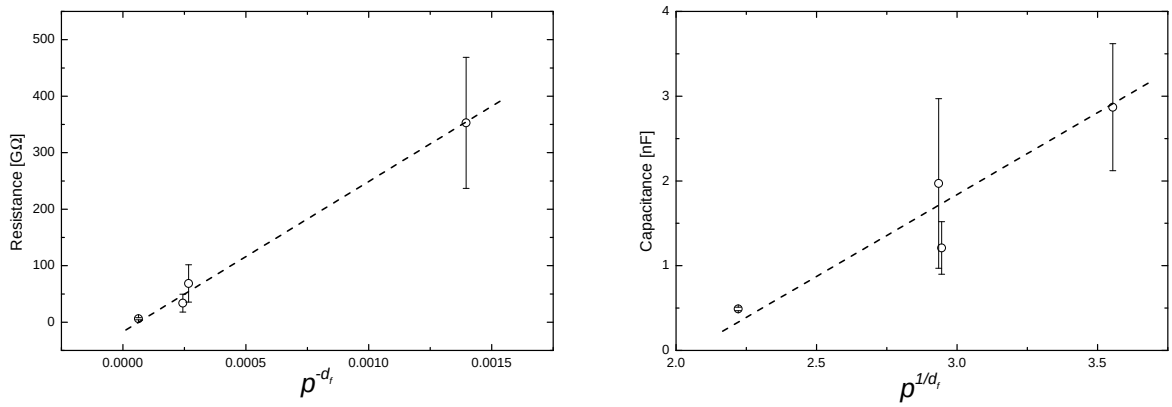

(a) (b)

Figure 6.5: Relationship between the minimum path p and fractal dimension d_f of different particle concentration of the 90 min. HEM M-Si printed layers and (a) resistance of the layers, (b) capacitance of the layers obtained from equation 5.22. The lines are guides to the eye.

The resistance was found to have a linear relationship with a negative power of the fractal dimension for the minimum path p. The function p^{-d_f} reflects the number of parallel connections of length p in the layer. In this case, the resistance will decrease as the number of the possible paths increases in the aggregates. In the case of the capacitance, this was found to have a linear relationship with a reciprocal power of the fractal dimension for p^{1/d_f} which reflects a series connection through the minimum path. Since the length of the minimum path increases with increase in particle concentration, the number of these path connected will decrease resulting in a decrease of the capacitance of the layer.

7. Conclusions

X-ray scattering techniques have been used to characterise electrically active nanoparticles and their aggregates when incorporated in a printed layer. For the first time, topological information of the particle aggregates inside the printed layer as well as the surface has been evaluated using laboratory and synchrotron based SAXS and USAXS, and the newly developed wide angle low q (WALq) scattering technique. This topological information was obtained using a scaling approach, which was originally developed for polymers, but in this work it was successfully applied for the first time to nanoparticulate systems. This led to the important opportunity to distinguish between topological features of layers of different nanoparticle aggregates, produced from various printed electronic ink systems.

In particular, electron microscopy performed on the printed layers and the analysis of small angle scattering data using scaling model, showed that the size distributions of the nanoparticles produced from high energy milling are highly disperse. The mean size of the particle distribution was shown to decrease with increasing milling time. Variation in particle concentration in a printed layer also leads to a quantitative change in the radius of gyration of the first structural level, reflecting the separation between particles in the aggregates. Furthermore, it was shown that in the printed layers, the primary particles formed agglomerates, which in turn cluster to form larger aggregates. This was indicated by the high mass fractal dimension, twofold coordination and very high degree of aggregation of the aggregates. In contrast, nanoparticles with a narrow size distribution synthesized by thermal catalytic pyrolysis of silane form small, more open clusters with a low fractal dimension and lower degree of aggregation, but which also further aggregate to form larger more open clusters of clusters.

A new surface scattering technique, WALq, was developed to probe surface topography which allows, together with studies of the internal microstructure, a better understanding of the printed layers. Topological features of the surface of layers printed from high energy milled silicon nanoparticle inks exhibit a high surface roughness with step heights of 10% to 20% of the particle diameter between adjacent particles. This was found to be consistent with the topology of the particle aggregates inferred from the USAXS measurement of the printed layers, but confirmed using WALq. The type of substrate, the properties of the inks, as well as the curing time of the layers under ambient conditions leads to a quantitative change in the radius of gyration for observed aggregate structural level ($R_{g,2}$), which can be interpreted as a change in mean aggregate separation. Slowly curing systems with a good

capillary flow conditions lead to denser networks, with smaller aggregates and better contact between particles.

The relationship between the mean particle separation and the electrical properties of the printed layers was obtained by combining structural information from USAXS measurements with electrical measurements. The resistance of the nanoparticle network was found to have a non-linear relationship with the distance between centres of primary particles. This could be interpreted as being partly due to a decreasing contact area as the particles move apart, but a full understanding requires the description of the network topology in the aggregate. The conductance was found to have a power relationship with the minimum path length (describing the inter-particle connections), where the power law is the fractal dimension of the aggregate. This combination describes the parallel connections of the average minimum path in the particle aggregates. Furthermore, the capacitance of the layers was found to have linear relationships with both the separation between primary particles and a series connection of the average minimum path, shown by a power law dependence to the inverse fractal dimension.

However, the relationship between fractal properties of aggregate systems and their electrical properties is still an open ended question. This thesis has shown that the topology of silicon nanoparticulate aggregate systems in printed layers is related to the electrical properties of the layers. Similar approaches should be used to study other nanoparticles used in electronic ink systems.

References

[1] Y Lee, J Choi, KJ Lee, NE Stott, and D Kim. Large-scale synthesis of copper nanoparticles by chemically controlled reduction for applications of inkjet-printed electronics. *Nanotechnology*, 19:415604, 2008.

[2] SH Ko, H Pan, CP Grigoropoulos, CK Luscombe, JMJ Fréchet, and D Poulikakos. All-inkjet-printed flexible electronics fabrication on a polymer substrate by low-temperature high-resolution selective laser sintering of metal nanoparticles. *Nanotechnology*, 18:345202, 2007.

[3] KJ Lee, BH Jun, TH Kim, and J Joung. Direct synthesis and inkjetting of silver nanocrystals toward printed electronics. *Nanotechnology*, 17:2424, 2006.

[4] RW Kelsall, IW Hamley, M Geoghegan, and J Wiley. *Nanoscale science and technology*. Wiley Online Library, 2005.

[5] M Hosokawa, K Nogi, M Naito, and T Yokoyama. *Nanoparticle technology handbook*. Elsevier, 2007.

[6] S Magdassi, M Grouchko, and A Kamyshny. Copper nanoparticles for printed electronics: routes towards achieving oxidation stability. *Materials*, 3:4626–4638, 2010.

[7] T Hanemann and DV Szabó. Polymer-nanoparticle composites: from synthesis to modern applications. *Materials*, 3:3468–3517, 2010.

[8] LS Schadler, LC Brinson, and WG Sawyer. Polymer nanocomposites: a small part of the story. *Jom*, 59:53–60, 2007.

[9] Z-M Dang, J-K Yuan, S-H Yao, and R-J Liao. Flexible nanodielectric materials with high permittivity for power energy storage. *Advanced Materials*, 25:6334–6365, 2013.

[10] U Simon. Charge transport in nanoparticle arrangements. *Advanced Materials*, 10:1487–1492, 1998.

[11] Michael G Todd and Frank G Shi. Characterizing the interphase dielectric constant of polymer composite materials: Effect of chemical coupling agents. *Journal of applied physics*, 94(7):4551–4557, 2003.

[12] Michael G Todd and Frank G Shi. Molecular basis of the interphase dielectric properties of microelectronic and optoelectronic packaging materials. *Components and Packaging Technologies, IEEE Transactions on*, 26(3):667–672, 2003.

[13] SR Forrest. The path to ubiquitous and low-cost organic electronic appliances on plastic. *Nature*, 428:911–918, 2004.

[14] HE Katz and J Huang. Thin-film organic electronic devices. *Annual Review of Materials Research*, 39:71–92, 2009.

[15] B Sun and H Sirringhaus. Solution-processed zinc oxide field-effect transistors based on self-assembly of colloidal nanorods. *Nano Lett*, 5:2408–2413, 2005.

[16] DT Britton and M Härting. Printed nanoparticulate composites for silicon thick-film electronics. *Pure and Applied Chemistry*, 78:1723–1739, 2006.

[17] M Härting, J Zhang, DR Gamota, and DT Britton. Fully printed silicon field effect transistors. *Applied Physics Letters*, 94:193509–193509, 2009.

[18] S Kirkpatrick. Percolation and conduction. *Rev. Mod. Phys.*, 45:574–588, 1973.

[19] BJ Last and DJ Thouless. Percolation theory and electrical conductivity. *Physical Review Letters*, 27:1719–1721, 1971.

[20] JP Fitzpatrick, RB Malt, and F Spaepen. Percolation theory and the conductivity of random close packed mixtures of hard spheres. *Physics Letters A*, 47:207–208, 1974.

[21] ME Cates. Brownian dynamics of self-similar macromolecules. *Journal de Physique*, 46:1059–1077, 1985.

[22] ME Cates. The fractal dimension and connectivity of random surfaces. *Physics Letters B*, 161:363–367, 1985.

[23] R Dekeyser, A Maritan, and A Stella. Deterministic fractal models for transport properties, inspired by d= 2 random walks. *Physical Review A*, 40:5299, 1989.

[24] JE Martin and AJ Hurd. Scattering from fractals. *Journal of applied Crystallography*, 20:61–78, 1987.

[25] J Teixeira. Small-angle scattering by fractal systems. *Journal of Applied Crystallography*, 21:781–785, 1988.

[26] G Beaucage. Determination of branch fraction and minimum dimension of mass-fractal aggregates. *Physical Review E*, 70:031401, 2004.

[27] G Beaucage. Toward resolution of ambiguity for the unfolded state. *Biophysical journal*, 95:503–509, 2008.

[28] R Ramachandran, G Beaucage, AS Kulkarni, D McFaddin, J Merrick-Mack, and V Galiatsatos. Branch content of metallocene polyethylene. *Macromolecules*, 42:4746–4750, 2009.

[29] PY Yu and M Cardona. *Fundamentals of semiconductors: physics and materials properties*. Springer Berlin etc, 1999.

[30] EW Paul, AJ Ricco, and MS Wrighton. Resistance of polyaniline films as a function of electrochemical potential and the fabrication of polyaniline-based microelectronic devices. *The Journal of Physical Chemistry*, 89:1441–1447, 1985.

[31] J Yu, P Cheng, Z Ma, and B Yi. Fabrication of a miniature twin-fuel-cell on silicon wafer. *Electrochimica Acta*, 48:1537–1541, 2003.

[32] AJ Snell, KD Mackenzie, WE Spear, PG LeComber, and AJ Hughes. Application of amorphous silicon field effect transistors in addressable liquid crystal display panels. *Applied physics*, 24:357–362, 1981.

[33] DE Carlson and CR Wronski. Amorphous silicon solar cell. *Applied Physics Letters*, 28:671–673, 1976.

[34] DE Carlson. Amorphous silicon solar cells. *Electron Devices, IEEE Transactions on*, 24:449–453, 1977.

[35] E Fabre and Y Baudet. Polycrystalline silicon solar cells. In *Photovoltaic Solar Energy Conference*, volume 1, pages 178–186, 1978.

[36] EC Garnett and P Yang. Silicon nanowire radial p- n junction solar cells. *Journal of the American Chemical Society*, 130:9224–9225, 2008.

[37] I Matsui. Nanoparticles for electronic device applications: a brief review. *Journal of chemical engineering of Japan*, 38:535–546, 2005.

[38] SK Ghosh and T Pal. Interparticle coupling effect on the surface plasmon resonance of gold nanoparticles: from theory to applications. *Chemical Reviews*, 107:4797–4862, 2007.

[39] Y Yin and AP Alivisatos. Colloidal nanocrystal synthesis and the organic–inorganic interface. *Nature*, 437:664–670, 2004.

[40] AA Onischuk, AI Levykin, VP Strunin, MA Ushakova, RI Samoilova, KK Sabelfeld, and VN Panfilov. Aerosol formation under heterogeneous/homogeneous thermal decomposition of silane: experiment and numerical modeling. *Journal of aerosol science*, 31:879–906, 2000.

[41] MT Swihart. Vapor-phase synthesis of nanoparticles. *Current Opinion in Colloid & Interface Science*, 8:127–133, 2003.

[42] RA Bley and SM Kauzlarich. A low-temperature solution phase route for the synthesis of silicon nanoclusters. *Journal of the American Chemical Society*, 118:12461–12462, 1996.

[43] R Ghosh Chaudhuri and S Paria. Core/shell nanoparticles: classes, properties, synthesis mechanisms, characterization, and applications. *Chemical reviews*, 112:2373–2433, 2011.

[44] BA Larsen, MA Haag, NJ Serkova, KR Shroyer, and CR Stoldt. Controlled aggregation of superparamagnetic iron oxide nanoparticles for the development of molecular magnetic resonance imaging probes. *Nanotechnology*, 19:265102, 2008.

[45] MR Scriba, DT Britton, and M Härting. Electrically active, doped monocrystalline silicon nanoparticles produced by hot wire thermal catalytic pyrolysis. *Thin Solid Films*, 519:4491–4494, 2011.

[46] MR Scriba, DT Britton, and M Härting. Hot wire and spark pyrolysis as simple new routes to silicon nanoparticle synthesis. *Nanostructured Materials and Nanotechnology VI*, pages 69–80, 2013.

[47] S Bernotat and K Schönert. Size reduction. In VCH Verlagsgesellschaft, editor, *Ullmann's Encyclopedia of Industrial Chemistry*, volume B2, pages 5.1–5.39. Weinheim, 1998.

[48] I Sandu, P Moreau, D Guyomard, T Brousse, and L Roue. Synthesis of nanosized si particles via a mechanochemical solid–liquid reaction and application in li-ion batteries. *Solid State Ionics*, 178:1297–1303, 2007.

[49] PG Kuzmin, GA Shafeev, VV Bukin, SV Garnov, C Farcau, R Carles, B W-F, V Guieu, and G Viau. Silicon nanoparticles produced by femtosecond laser ablation in ethanol: size control, structural characterization, and optical properties. *The Journal of Physical Chemistry C*, 114:15266–15273, 2010.

[50] NT Jenkins, WMG Pierce, and TW Eagar. Particle size distribution of gas metal and flux cored arc welding fumes. *Welding J*, 84:158–163, 2005.

[51] M Lattuada, P Sandkühler, H Wu, J Sefcik, and M Morbidelli. Aggregation kinetics of polymer colloids in reaction limited regime: experiments and simulations. *Advances in colloid and interface science*, 103:33–56, 2003.

[52] BB Mandelbrot. *The fractal geometry of nature*. Macmillan, 1983.

[53] TA Witten Jr and LM Sander. Diffusion-limited aggregation, a kinetic critical phenomenon. *Physical review letters*, 47:1400, 1981.

[54] R Jullien and M Kolb. Hierarchical model for chemically limited cluster-cluster aggregation. *Journal of Physics A: Mathematical and General*, 17:L639, 1984.

[55] G Pranami. *Understanding nanoparticle aggregation*. PhD thesis, Iowa State University, Ames, Iowa, 2009.

[56] P Meakin. Diffusion-controlled cluster formation in two, three, and four dimensions. *Physical Review A*, 27:604, 1983.

[57] AP Weber and SK Friedlander. Relation between coordination number and fractal dimension of aerosol agglomerates. *Journal of Aerosol Science*, 28:S765–S766, 1997.

[58] P Meakin and R Jullien. The effects of restructuring on the geometry of clusters formed by diffusion-limited, ballistic, and reaction-limited cluster–cluster aggregation. *The Journal of chemical physics*, 89:246, 1988.

[59] DW Schaefer, JE Martin, P Wiltzius, and DS Cannell. Fractal geometry of colloidal aggregates. *Physical Review Letters*, 52:2371, 1984.

[60] MY Lin, HM Lindsay, DA Weitz, RC Ball, R Klein, and P Meakin. Universality of fractal aggregates as probed by light scattering. *Proceedings of the Royal Society of London. A. Mathematical and Physical Sciences*, 423:71–87, 1989.

[61] A Guinier. Structure of age-hardened aluminium-copper alloys. *Nature*, 142:569–570, 1938.

[62] G Porod. Die röntgenkleinwinkelstreuung von dichtgepackten kolloiden systemen. *Kolloid-Zeitschrift*, 124:83–114, 1951.

[63] G Porod. Die röntgenkleinwinkelstreuung von dichtgepackten kolloiden systemen. ii. teil. *Kolloid-Zeitschrift*, 125:108–122, 1952.

[64] P Debye and AM Bueche. Scattering by an inhomogeneous solid. *Journal of Applied Physics*, 20:518–525, 1949.

[65] P Debye, HR Anderson, and H Brumberger. Scattering by an inhomogeneous solid. ii. the correlation function and its application. *Journal of applied Physics*, 28:679–683, 1957.

[66] O Kratky. Die berechnung der mizelldimensionen von faserstoffen aus den unter kleinsten winkeln abgebeugten interferenzen. *Naturwissenschaften*, 26:94–94, 1938.

[67] O Kratky and G Porod. Diffuse small-angle scattering of x-rays in colloid systems. *Journal of Colloid Science*, 4:35 – 70, 1949.

[68] A Guinier, G Fournet, CB Walker, and KL Yudowitch. *Small-angle scattering of X-rays*, volume 14. Wiley New York, 1955.

[69] DT Britton, EA Odo, GG Gonfa, EO Jonah, and M Harting. Size distribution and surface characteristics of silicon nanoparticles. *Journal of Applied Crystallography*, 42:448–456, 2009.

[70] EO Jonah, DT Britton, P Beaucage, D Rai, G Beaucage, B Magunje, J Ilavsky, MR Scriba, and M Härting. Topological investigation of electronic silicon nanoparticulate aggregates using ultra-small-angle x-ray scattering. *Journal of Nanoparticle Research*, 14:1–10, 2012. 10.1007/s11051-012-1249-y.

[71] DK Rai, G Beaucage, EO Jonah, DT Britton, S Sukumaran, S Chopra, GG Gonfa, and M Härting. Quantitative investigations of aggregate systems. *The Journal of Chemical Physics*, 137:044311–044311, 2012.

[72] M Kotlarchyk, S-H Chen, JS Huang, and MW Kim. Structure of three-component microemulsions in the critical region determined by small-angle neutron scattering. *Physical Review A*, 29:2054, 1984.

[73] T Ito, L Sun, MA Bevan, and RM Crooks. Comparison of nanoparticle size and electrophoretic mobility measurements using a carbon-nanotube-based coulter counter, dynamic light scattering, transmission electron microscopy, and phase analysis light scattering. *Langmuir*, 20:6940–6945, 2004.

[74] DW Schaefer and C Chen. Structure optimization in colloidal reinforcing fillers: Precipitated silica. *Rubber chemistry and technology*, 75:773–794, 2002.

[75] O Glatter and O Kratky. *Small-angle x-ray scattering*. New York: Academic Press, 1982.

[76] DI Svergun, GW Taylor, and LA Feigin. *Structure analysis by small-angle X-ray and neutron scattering*. New York: Plenum Press, 1987.

[77] G Beaucage. Approximations leading to a unified exponential/power-law approach to small-angle scattering. *Journal of Applied Crystallography*, 28:717–728, 1995.

[78] PW Schmidt. Small-angle scattering studies of disordered, porous and fractal systems. *Journal of Applied Crystallography*, 24:414–435, 1991.

[79] K Malekani, JA Rice, and J-S Lin. Comparison of techniques for determining the fractal dimensions of clay minerals. *Clays and clay minerals*, 44:677–685, 1996.

[80] DW Schaefer and KD Keefer. Structure of random porous materials: silica aerogel. *Physical review letters*, 56:2199–2202, 1986.

[81] P Mangin, B Rodmacq, and A Chamberod. Fractal structure of tiH_2 aggregates in a cuti matrix. *Physical review letters*, 55:2899, 1985.

[82] H Boukari, JS Lin, and MT Harris. Probing the dynamics of the silica nanostructure formation and growth by saxs. *Chemistry of materials*, 9:2376–2384, 1997.

[83] H Tamon and H Ishizaka. Saxs study on gelation process in preparation of resorcinol–formaldehyde aerogel. *Journal of colloid and interface science*, 206:577–582, 1998.

[84] G Beaucage and DW Schaefer. Structural studies of complex systems using small-angle scattering: a unified guinier/power-law approach. *Journal of non-crystalline solids*, 172:797–805, 1994.

[85] G Beaucage. Small-angle scattering from polymeric mass fractals of arbitrary mass-fractal dimension. *Journal of Applied Crystallography*, 29:134–146, 1996.

[86] DWL Hukins et al. *X-ray diffraction by disordered and ordered systems.* Pergamon Press, 1981.

[87] AC Geiculescu and HJ Rack. X-ray scattering studies of polymeric zirconium species in aqueous xerogels. *Journal of non-crystalline solids*, 306:30–41, 2002.

[88] H Jensen, KD Joensen, J-E Jørgensen, JS Pedersen, and G Søgaard. Characterization of nanosized partly crystalline photocatalysts. *Journal of Nanoparticle Research*, 6:519–526, 2004.

[89] DW Schaefer, G Beaucage, DA Loy, KJ Shea, and JS Lin. Structure of arylene-bridged polysilsesquioxane xerogels and aerogels. *Chemistry of materials*, 16:1402–1410, 2004.

[90] DR Vollet, DA Donatti, and A Ibañez Ruiz. A saxs study of kinetics of aggregation of teos-derived sonogels at different temperatures. *Journal of non-crystalline solids*, 288:81–87, 2001.

[91] G Beaucage, TA Ulibarri, EP Black, and DW Schaefer. Multiple size scale structures in silica-siloxane composites studied by small-angle scattering. In *ACS symposium series*, volume 585, pages 97–97. ACS Publications, 1995.

[92] P Meakin, I Majid, S Havlin, and HE Stanley. Topological properties of diffusion limited aggregation and cluster-cluster aggregation. *Journal of Physics A: Mathematical and General*, 17:L975, 1984.

[93] MY Lin, HM Lindsay, DA Weitz, RC Ball, R Klein, and P Meakin. Universality in colloid aggregation. *Nature*, 339, 1989.

[94] S Costeux, P Wood-Adams, and D Beigzadeh. Molecular structure of metallocene-catalyzed polyethylene: rheologically relevant representation of branching architecture in single catalyst and blended systems. *Macromolecules*, 35:2514–2528, 2002.

[95] SK Friedlander. *Smoke, dust, and haze: Fundamentals of Aerosol Dynamics*, volume 198. Oxford University Press New York, 2000.

[96] G Beaucage, HK Kammler, and SE Pratsinis. Particle size distributions from small-angle scattering using global scattering functions. *Journal of applied crystallography*, 37:523–535, 2004.

[97] HK Kammler, G Beaucage, R Mueller, and SE Pratsinis. Structure of flame-made silica nanoparticles by ultra-small-angle x-ray scattering. *Langmuir*, 20:1915–1921, 2004.

[98] HK Kammler, G Beaucage, DJ Kohls, N Agashe, and J Ilavsky. Monitoring simultaneously the growth of nanoparticles and aggregates by in situ ultra-small-angle x-ray scattering. *Journal of applied physics*, 97:054309–054309, 2005.

[99] S Brunauer, PH Emmett, and E Teller. Adsorption of gases in multimolecular layers. *Journal of the American Chemical Society*, 60:309–319, 1938.

[100] P Baláž. *High-Energy Milling*. Springer, 2008.

[101] DY Sogah, WR Hertler, OW Webster, and GM Cohen. Group transfer polymerization-polymerization of acrylic monomers. *Macromolecules*, 20:1473–1488, 1987.

[102] J-S Wang, R Jérôme, P Bayard, M Patin, P Teyssie, B Vuillemin, and P Heim. Anionic polymerization of acrylic monomers. 16. living anionic copolymerization of methyl methacrylate and tert-butyl acrylate as promoted by lithium 2-(2-methoxyethoxy) ethoxide. *Macromolecules*, 27:4635–4638, 1994.

[103] S-C Liao, KD Pae, and WE Mayo. High pressure and low temperature sintering of bulk nanocrystalline tio$_2$. *Materials Science and Engineering: A*, 204:152–159, 1995.

[104] MD Abràmoff, PJ Magalhães, and SJ Ram. Image processing with imagej. *Biophotonics international*, 11:36–42, 2004.

[105] CA Schneider, WS Rasband, and KW Eliceiri. Nih image to imagej: 25 years of image analysis. *Nature Methods*, 9:671–675, 2012.

[106] MR Scriba. *Synthesis and Characterisation of doped silicon nanoparticles by hot wire thermal catalytic and spark pyrolysis*. PhD thesis, University of Cape Town, South Africa, Feb 2010.

[107] W Rosenthal, J Saleta, and J Dozier. Scanning electron microscopy of impurity structures in snow. *Cold regions science and technology*, 47:80–89, 2007.

[108] B Chu, BS Hsiao, et al. Small-angle x-ray scattering of polymers. *Chemical Reviews-Columbus*, 101:1727–1762, 2001.

[109] J Ilavsky, PR Jemian, AJ Allen, F Zhang, LE Levine, and GG Long. Ultra-small-angle x-ray scattering at the advanced photon source. *Journal of Applied Crystallography*, 42:469–479, 2009.

[110] JA Lake. An iterative method of slit-correcting small angle x-ray data. *Acta crystallographica*, 23:191–194, 1967.

[111] P-PEA de Moor, TPM Beelen, RA van Santen, K Tsuji, and ME Davis. Saxs and usaxs investigation on nanometer-scaled precursors in organic-mediated zeolite crystallization from gelating systems. *Chemistry of materials*, 11:36–43, 1999.

[112] NM Muhammad, N Duraisamy, K Rahman, HW Dang, J Jo, and KH Choi. Fabrication of printed memory device having zinc-oxide active nano-layer and investigation of resistive switching. *Current Applied Physics*, 2012.

[113] RW James. *The Optical Principles of the Diffraction of X-rays*. Ox Bow Press Woodbridge (Connecticut), 1982.

[114] PD Hatton, SB Wilkins, TAW Beale, TK Johal, D Prabhakaran, and AT Boothroyd. Resonant soft x-ray scattering—a new probe of charge, spin and orbital ordering in the manganites. *Journal of magnetism and magnetic materials*, 290:891–897, 2005.

[115] M Rauscher, R Paniago, H Metzger, Z Kovats, J Domke, J Peisl, H-D Pfannes, J Schulze, and I Eisele. Grazing incidence small angle x-ray scattering from free-standing nanostructures. *Journal of Applied Physics*, 86:6763–6769, 1999.

[116] A Naudon, T Slimani, and Ph Goudeau. Grazing small-angle scattering of x-rays for the study of thin surface layers. *Journal of Applied Crystallography*, 24:501–508, 1991.

[117] JR Levine, JB Cohen, YW Chung, and P Georgopoulos. Grazing-incidence small-angle x-ray scattering: new tool for studying thin film growth. *Journal of Applied Crystallography*, 22:528–532, 1989.

[118] JH Underwood, EM Gullikson, M Koike, PJ Batson, PE Denham, KD Franck, RE Tackaberry, and WF Steele. Calibration and standards beamline 6.3. 2 at the advanced light source. *Review of Scientific Instruments*, 67:3372–3372, 1996.

[119] JH Underwood and EM Gullikson. High-resolution, high-flux, user friendly vls beamline at the als for the 50-1300 ev energy region1. *Journal of electron spectroscopy and related phenomena*, 92:265–272, 1998.

[120] EM Gullikson, S Mrowka, and BB Kaufmann. Recent developments in euv reflectometry at the advanced light source. In *26th Annual International Symposium on Microlithography*, pages 363–373. International Society for Optics and Photonics, 2001.

[121] Center for X-Ray Optics. The world standard for euv and x-ray reflectance measurements. `http://cxro.lbl.gov/reflectometer`. Accessed on 16 March 2013.

[122] MC Bertilson, PAC Takman, A Holmberg, U Vogt, and HM Hertz. Laboratory arrangement for soft x-ray zone plate efficiency measurements. *Review of scientific instruments*, 78:026103–026103, 2007.

[123] M Kado, M Richardson, J M Rajyaguru, MJ Muszynski, H Friedman, and Y Yamamoto. Direct ultrastructural imaging of macrophages using a novel x-ray contact microscopy. *Proceedings of the Society for Experimental Biology and Medicine*, 220:27–30, 1999.

[124] U Männl, A Chuvilin, B Magunje, EO Jonah, M Härting, and DT Britton. Interfacial and network characteristics of silicon nanoparticle layers used in printed electronics. *Japanese Journal of Applied Physics*, 52, 2013.

[125] JH Lim, JH Shim, JH Choi, J Joo, K Park, H Jeon, MR Moon, D Jung, H Kim, and H-J Lee. Solution-processed ingazno-based thin film transistors for printed electronics applications. *Applied Physics Letters*, 95:012108–012108, 2009.

[126] Z Radivojevic, K Andersson, K Hashizume, M Heino, M Mantysalo, P Mansikkamaki, Y Matsuba, and N Terada. Optimised curing of silver ink jet based printed traces. *arXiv preprint arXiv:0709.1842*, 2007.

[127] TA Burr, AA Seraphin, E Werwa, and KD Kolenbrander. Carrier transport in thin films of silicon nanoparticles. *Physical Review B*, 56:4818, 1997.

[128] B Magunje. *Charge Transport in Printed Silicon Nanoparticle Networks*. PhD thesis, University of Cape Town, South Africa, Nov 2012.

[129] DT Britton, SD Walton, S Zambou, B Magunje, EO Jonah, and M Härting. A novel mode of current switching dependent on activated charge transport. *AIP Advances*, 3:082110, 2013.

[130] WC Hinds. Aerosol technology, 1999.

[131] AM Brasil, TL Farias, MG Carvalho, and UO Koylu. Numerical characterization of the morphology of aggregated particles. *journal of Aerosol Science*, 32:489–508, 2001.

[132] AP Weber and SK Friedlander. In situ determination of the activation energy for restructuring of nanometer aerosol agglomerates. *Journal of aerosol science*, 28:179–192, 1997.

[133] MR Scriba, DT Britton, C Arendse, MJ van Staden, and M Härting. Composition and crystallinity of silicon nanoparticles synthesised by hot wire thermal catalytic pyrolysis at different pressures. *Thin Solid Films*, 517:3484–3487, 2009.

List of Figures

List of Tables